UNIVERSITÉ DE STRASBOURG

UNIVERSITÉ DE STRASBOURG

IPCMS

ÉCOLE DOCTORALE PHYSIQUE ET CHIMIE-PHYSIQUE

Institut de Physique et Chimie des Matériaux de Strasbourg

THÈSE présentée par:

Thomas ROLAND

soutenue le : 10 avril 2014

pour obtenir le grade de: **Docteur de l'université de Strasbourg**

Discipline / Spécialité: Physique

Ultrafast Spectroscopy of New Organic Molecules for Photovoltaic Applications

---

THÈSE dirigée par :

M. HAACKE Stefan — Professeur, Université de Strasbourg

RAPPORTEURS :

M. VAUTHEY Eric — Professeur, Université de Genève

M. PLAZA Pascal — Directeur de Recherche, ENS

AUTRES MEMBRES DU JURY:

M. DORKENOO Honorat — Professeur, Université de Strasbourg

M. LÉONARD Jérémie — Chargé de recherche, IPCMS

Contents

0.1 Remerciements

Je voudrais remercier en premier lieu mon directeur de thèse, Stefan Haacke, qui après m'avoir permis de découvrir le travail de l'équipe BIODYN lors de mon stage de fin d'étude, a accepté d'encadrer cette thèse. En particulier, je souhaite le remercier pour tout le temps qu'il a consacré à cette tâche, en restant toujours disponible malgré un emploi du temps très chargé. De même, je tiens à le remercier pour sa patience lors de nos discussions, pour m'avoir appris non seulement énormément sur la physique, mais aussi (entre autres) à présenter mes résultats lors des réunions d'équipe. Un grand merci également pour tous les efforts du point de vue des relations humaines, car il a toujours été agréable de travailler au sein de l'équipe.

Je remercie également Jérémie Léonard, pour tout ce qu'il a pu m'apprendre, et sa capacité à toujours avoir de bonnes questions ou remarques. De même, je voudrais dire un grand merci à Olivier Crégut, pour sa disponibilité, toutes les fois où il a répondu à mes questions, ou m'a aidé à optimiser les expériences.

Il me faut aussi remercier Thomas Heiser, sans qui je n'aurais sans doute jamais eu l'occasion de venir à l'IPCMS, et Donatas Zigmantas qui m'a fait découvrir la spectroscopie bi-dimensionnelle.

Je remercie également Sophie Barre, Gautier Dekyndt, Nicolas Beyer, Benoît Heinrich, Dominique Quince et Estelle Brunette pour leur aide toujours efficace. Merci également à Alex Boeglin, grâce à qui j'ai grandement amélioré mon vocabulaire en anglais.

Je tiens à adresser également tous mes remerciements à l'ensemble des amis que j'ai pu me faire durant cette thèse, pour leur soutien et les bons moments passés ensemble: Jean, Bertrand, Thomas, Yannick et Patricia, Sacha, Alexandre, Deborah, P-O, Jamie, Naya, Li, Moussa, Thierry,... et à l'ensemble du RUCK.

Finalement, je veux remercier toute ma famille, qui m'a supporté tout ce temps.

0.2 Résumé en français

0.2.1 Introduction

Cette thèse porte sur l'étude par spectroscopie ultrarapide de nouvelles molécules organiques pour le photovoltaïque. Cette étude est motivée par le besoin croissant en énergie, notamment électrique. En effet, l'augmentation de la population mondiale ainsi que du niveau de vie implique une consommation grandissante d'énergie, dont la production est de plus en plus problématique. Effectivement, si de nombreuses solutions existent toutes ont leurs avantages et inconvénients: le nucléaire bien qu'efficace souffre d'une opinion publique désastreuse, les énergies fossiles voient leur rareté (et leur prix) augmenter en plus de poser des soucis écologiques,... Une solution favorisée depuis quelques année est le photovoltaïque, consistant à convertir l'énergie solaire en électricité.

Toutefois, la génération de photo-courant est généralement basée sur l'utilisation de cellules photovoltaïques en silicium, qui si elles sont très efficaces (les records d'efficacité dépassant les 40 %) restent très onéreuses, principalement à cause de la purification nécessaire du silicium et des dopants à intégrer. C'est pourquoi de nouvelles solutions sont mises au point, qui cherchent à remplacer le silicium par des matériaux organiques semi-conducteurs, qui peuvent non seulement être synthétisés à moindre coût, mais aussi permettent de fabriquer les dispositifs de façon beaucoup plus économique, puisqu'une "simple" impression est envisageable.

Ces nouveaux matériaux sont certes prometteurs, mais n'offrent pour le moment que des performances réduites par rapport au silicium (dépassant au mieux les 9%), ce qui motive l'étude de ces matériaux, afin de mieux identifier les processus impliqués dans la photogénération de charges. Ces processus (génération d'excitons, séparation, diffusion et recombinaison de charges,..) ont typiquement lieu à des échelles de temps allant de la femto- à la nano-seconde, et nécessitent donc des méthodes particulières pour être étudiées. Ces méthodes sont brièvement décrites dans la section suivante, et seront appliquées à l'étude de deux familles de molécules. La première a été développée de façon à agir comme une antenne (composée de trois blocs) donneuse d'électrons à large spectre d'absorption, de manière à ce que -en présence d'une molécule de type accepteur- la photo-excitation d'un des trois blocs conduise à la formation d'une paire de charges. La seconde famille de molécules se base sur l'idée d'utiliser des matériaux de

type cristal-liquide combinant des blocs donneurs et accepteurs (formant dans notre cas une triade donneur-accepteur-donneur, dite DAD) et comporte deux générations: après l'étude de la première génération de DAD et l'identification de paramètres limitant l'efficacité de la molécule, une deuxième génération a été mise au point, incluant une variété de blocs donneurs permettant d'étudier en détail l'effet de certains paramètres tels que la distance entre groupe donneur et accepteur, ou la nature des groupements espaceurs.

0.2.2 Méthodes

Plusieurs méthodes complémentaires ont été utilisées dans cette étude. Si les données principales ont été obtenues par la méthodes de spectroscopie pompe-sonde, l'analyse détaillée des résultats n'a été possible que grâce à un ensembles d'autres méthodes: la fluorescence résolue en temps (caméra à balayage de fente), la spectro-electro-chimie et l'absorption statique UV-Vis.

La spectroscopie pompe sonde consiste à suivre les variations de l'absorption d'un échantillon après son excitation par une impulsion pompe. Partant d'impulsions femtoseconde (~40 fs), deux impulsions sont créées: l'une qui servira de pompe, et qui déclenchera la photoréaction à un instant t_0 donné, et une autre qui servira de sonde (couvrant un spectre large allant du proche UV au proche IR), qui après être passée dans une ligne à délai passera à un délai "t" après t_0 à travers l'échantillon, ce qui permet d'obtenir le spectre d'absorption de ce dernier (voir fig. 2.2). Ce spectre d'absorption peut être comparé à celui de l'échantillon à son état fondamental, ce qui révèle le spectre d'absorption différentielle (à l'état excité moins celle à l'état fondamental) à l'instant t (la figure 2.6 illustre les différents phénomènes observables). En faisant varier la distance parcourue par la sonde dans la ligne à délai, on peut faire varier le délai t, et ainsi scanner l'ensemble de la dynamique de l'échantillon; dans notre cas, limitée aux temps courts par la résolution temporelle (~60fs) et aux temps longs par la longueur de la ligne à délai (~5ns).

Les données "pompe-sonde" permettent donc d'obtenir le spectre caractéristique de l'état de l'échantillon à un instant t après excitation. Toutefois, afin de pouvoir identifier les différentes contributions présentes dans ces spectres (quelles sont les espèces impliquées, et dans quel état), il est intéressant de pouvoir identifier lesdites contributions de façon univoque. Cela est fait en utilisant une caméra à balayage

de fente (qui nous donne accès à la fluorescence résolue en temps de l'échantillon) et la spectro-electro-chimie (qui nous donne accès aux spectres d'absorption des différentes espèces chargées, expériences réalisées par l'équipe de Sabine Ludwigs).

En identifiant les dites contribution dans les données pompe-sonde à chaque instant après l'excitation de l'échantillon, on peut reconstruire le schéma réactionnel suivi par l'échantillon. Pour obtenir les constantes de temps associées aux différentes, un ajustement des données cinétiques avec un modèle (généralement une somme d'exponentielles décroissantes) est effectué, tout d'abord à certaines longueur d'onde choisies, puis de façon globale.

0.2.3 Résultats

0.2.3.1 Cascade

Le dispositif organique photovoltaïque le plus étudié ("de référence") est le blend P3HT/PCBM (respectivement poly(3-hexylthiophene) et [6,6]-phenyl-C_{61}-butyric acid methyl ester), toutefois une des limitations de ce matériau viens du spectre d'absorption limité du P3HT. Une des voies explorées pour améliorer les performances photovolta¨est donc de remplacer le P3HT par un autre donneur conservant de bonne propriétés de transfert et conductivité, mais avec un spectre d'absorption plus important (spectralement plus large).

La "cascade" étudiée ici (dans le THF -tétrahydrofurane-), mise au point par Élodie Heyer et Raymond Ziessel, a été développée dans cet objectif, en combinant trois blocs donneurs : TPA, DPP et BOD (respectivement triphenylamine, diketopyrrolopyrrole et boron-dipyrromethene, représentés fig. 3.1) aux spectres d'absorption complémentaires en une "cascade". Connaissant les propriétés électroniques de chaque bloc, le comportement prévu est qu'un excitation d'un quelconque bloc résulte au final en la localisation de l'excitation sur le BOD, connu pour ses bonnes propriétés de donneur d'électrons (par exemple l'excitation de TPA sera transférée à DPP, puis à BOD, d'où le terme "cascade"). Le but de l'étude est d'analyser le comportement effectif de cette antenne.

Une première observation peut être faite sur les spectres d'absorption statiques de cette cascade: si les spectres d'absorption des composants isolés sont effectivement complémentaires pour couvrir l'ensemble de la plage spectrale allant de 280 à 680 nm, on ne reconnait pas dans

l'absorption de la cascade complète celle du DPP (attendue entre 450 et 550nm), cette dernière se retrouvée décalée de manière bathochrome (vers le rouge), et se superpose à celle du BOD.

De la même façon, le spectre de fluorescence de DPP et BOD se retrouvent superposés, et donc difficilement discernables (comme le montre la figure 3.8). Toutefois, il est possible par spectroscopie résolue en temps d'obtenir un certain nombre d'informations. Premièrement, la fluorescence de TPA n'est pas détectable dans la cascade, indiquant un transfert d'énergie (ou de charge) extrêmement rapide depuis le TPA vers DPP et/ou BOD. Deuxièmement la fluorescence détectée est une superposition de celles de DPP et BOD, traduisant la présence des états excités de DPP et BOD simultanément (notés DPP* et BOD*. De plus, on remarque que les temps de vie de la fluorescence de ces deux groupes sont significativement plus courts que pour les molécules isolées (les temps de vie de DPP et BOD isolés sont respectivement de 2.2 et 4.5 ns, alors que les temps de vie trouvés pour la cascade sont de 63 ps, 518 ps et 2.3 ns). La fluorescence de la cascade peut ainsi être décomposée en trois contributions: une première correspondant à la fluorescence de DPP* associée à une constante de temps de 63 ps, une seconde correspondant à la fluorescence de BOD, associée à une constante de temps de 518 ps, et finalement une troisième qui correspond aux deux molécules, associée à une constante de 2.3 ns. Cela semble indiquer qu'il existe une hétérogénéité de conformations au sein des molécules, qui crée plusieurs populations avec des dynamiques différentes: certaines permettant le quenching de la fluorescence (probablement via la formation d'états transfert de charge, en 63 et 518 ps), et d'autres interdisant la formation de ces états.

Utilisant les observations précédentes et les spectres d'absorptions des espèces chargées, nous pouvons interpréter les spectres d'absorption différentielle obtenus par pompe-sonde sur la cascade et les blocs isolés. Ceux-ci révèlent qu'après excitation à 400 nm, on observe plusieurs transferts d'énergie, tout d'abord depuis TPA* vers les deux autres blocs, puis depuis une fraction de la population de DPP* vers BOD. La fraction restante de DPP* réalise un transfert d'électron avec BOD, conduisant à la formation en ~ 52 ps d'un état transfert de charge, d'une durée de vie d'environ 500ps. Le schéma réactionnel complet est représenté figure 3.16.

Si l'étude de cette molécule isolée (sans polymère accepteur) ne permet pas de définir de manière certaine les performances potentielles de cette cascade, nous pouvons néanmoins affirmer qu'après excitation -

même à haute énergie-, la majeure partie de l'énergie est transférée vers le groupe BOD, ce qui devrait être favorable au transfert de charges vers un accepteur. De même, le reste de l'énergie apportée par la pompe se localise sur le groupe DPP, soit sous la forme de DPP*, soit sous la forme du radical anion DPP^-, ce qui dans les deux cas peut également permettre un transfert de charge. Un deuxième point que montre cette étude est que malgré des signatures spectrales intriquées de trois blocs, l'utilisation d'expériences complémentaires peut permettre de décrypter les données de pompe-sonde et définir un modèle, même dans un cas complexe comme celui-ci.

0.2.3.2 Première génération de DAD

Une autre étude a été menée sur une molécule ayant des propriétés cristal liquide. L'idée derrière la mise au point de ces molécules est d'améliorer la structuration des cellules photovoltaïques en créant une alternance de domaines donneurs et accepteurs. Cela afin d'éviter certains défauts observés dans les blends de polymères: en effet il arrive que les excitons créés le soient à une distance trop grande d'une interface donneur/accepteur, ce qui empêche la formation de paires de charges, ou qu'une des charges créées le soit dans un domaine non connecté aux électrodes de la cellule, ce qui entraine la perte de la charge. Un système correctement structuré (alternance donneur/accepteur dans des domaines bidimensionnels) permet d'une part d'assurer la présence d'une interface donneur/accepteur à proximité immédiate des excitons formés, et d'autre part d'assurer la conduction de ces charges vers les électrodes.

La molécule étudiée dite "de première génération" se base sur un coeur pérylène diimide (noté "A"), connu à la fois pour ses propriétés accepteur et sa capacité à se structurer (via π-stacking), auquel sont greffés des groupements donneurs (notés "D") composés de groupes thiophènes et phényl, les propriétés cristal liquide étant assurée par des chaines terminales siloxanes. La structure de la triade DAD est représentée figure 4.2, ainsi que son organisation attendue en film.

Les spectres d'absorption statiques des groupes A et D peuvent être utilisés pour reconstruire celui de la triade DAD, indiquant un faible couplage électronique entre les différents blocs. L'étude de la photodynamique de cette molécule a été faite tout d'abord en solution afin de pouvoir identifier les signatures des différents états de molécules isolées, avant d'être ensuite réalisée sur la molécule à l'état cristal-liquide, en

film, situation plus proche de celle rencontrée dans les cellules photovoltaïques fonctionnelles, où les différentes molécules interagissent entre elles.

L'étude de la molécule en solution dans le chloroforme (la figure 4.8 reprend les spectres différentiels les plus significatifs) révèle qu'après excitation du donneur (D^*AD), un transfert d'énergie très rapide a lieu vers l'accepteur (DA^*D, en ~ 130 fs), suivi de la formation de l'état transfert de charge (D^+A^-D, en ~ 2.7 ps), qui a une durée de vie d'environ 55 ps. L'identification de cet état transfert de charge a été confirmée par la détermination via spectro-electro-chimie des spectres d'absorption des radicaux $A^{-\cdot}$ et $D^{+\cdot}$. On voit déjà ici ce qui pourrait être un élément limitant des performances de la molécule: l'état transfert de charge a une durée de vie extrêmement courte.

L'étude de la molécule a ensuite été menée en film (une selection de spectres différentiels sont reproduits figure 4.11), où l'on observe cette fois la formation directe et extrêmement rapide de l'état transfert de charge après excitation du bloc donneur. Le déclin de la signature de l'état transfert de charge se fait avec trois constantes de temps (de 1.1 ps, 70 ps and 1.3 ns), ce que l'on traduit par trois phénomènes distincts. La constante de temps de 70 ps est du même ordre de grandeur que celle de 55 ps observée en solution, et est donc attribuée au même phénomène de recombinaison de charges intra-moléculaire. La constante de temps de 1.3 ns est associé à une recombinaison de charges inter-moléculaire (donc plus éloignées l'une de l'autre), venant donc de charges positives et négatives localisées sur des molécules voisines, ce qui est possible à cause de la formation en moins de 100 fs de l'état transfert de charge, avant la localisation de l'exciton. La constante de 1.1 ps est attribuée soit à une recombinaison intra-moléculaire rendue possible par des contraintes géométriques particulières, soit une recombinaison bi-moléculaire. La formation d'une faible population de triplets de A est également détectée.

Si l'observation d'un temps de vie de 1.3 ns semble favorable à de bonnes performances photovoltaïques, les deux constantes de temps courtes impliquent une perte importante d'efficacité, de même que la formation d'états triplets. Pour cette raison une nouvelle génération de molécules a été mise au point, avec comme objectif d'obtenir un temps de vie de l'état transfert de charge aussi long que possible, tout en conservant une formation efficace de cet état.

0.2.3.3 Seconde génération de DAD

La nouvelle famille de molécules mise au point conserve le même coeur accepteur périlène diimide (noté A), mais a été déclinée en un ensemble de molécules avec différents groupes donneurs (D), permettant de varier indépendamment la nature de l'espaceur entre donneur et accepteur (notés δ ou δ_+), la longueur du donneur (D_n, n variant de 0 à 3) et la présence d'une amine terminale (notée δ_-), une représentation de l'ensemble de ces molécules est donnée figure 4.13. Le comportement de l'ensemble de ces molécule a pu être étudié, et les effets de ces différents paramètres identifiés.

Un total de sept molécules ont été étudiées, uniquement en solution (dans le chloroforme): l'effet des groupes δ,δ_+ et δ_- a été mis en évidence à travers la comparaison des résultats obtenus sur les molécules $\delta_-D_1\delta A$, $D_1\delta A$, $D_1\delta_+A$ et $\delta_-D_1\delta_+A$, tandis que l'effet de la longueur du donneur l'a été par l'étude des molécules $D_0\delta_+A$, $D_1\delta_+A$, $D_2\delta_+A$ et $D_3\delta_+A$.

En utilisant les mêmes principes que précédemment, les données pompe-sonde obtenues pour chaque molécule ont pu être analysées afin de définir un schéma réactionnel. La formation d'états excités ou d'états transfert de charge est confirmée par la comparaison des spectres différentiels obtenus avec les spectres fluorescences ou les spectres d'absorption des espèces chargées.

Dans tous les cas, la formation de l'état transfert de charge est observé, mais l'on peut noter d'importantes variations dans les processus observés en fonction de la présence ou non du groupement δ_+. En effet, en l'absence de ce groupe, la réaction observée est très semblable à celle de la première génération (par exemple la molécule $\delta_-D_1\delta A$, dont les spectres différentiels principaux sont représentés figure 4.16): après excitation du groupe donneur, un transfert d'énergie vers l'accepteur a lieu en ~1 ps, suivi de la formation de l'état transfert de charge en une quinzaine de picosecondes. À contrario, en présence du groupe δ_+ ce transfert d'énergie n'est pas observé, et la formation de l'état transfert de charge a lieu (vraisemblablement à travers 2 chemins réactionnels, associés à des constantes de temps de ~ 10 ps et ~ 150 ps) directement après l'excitation du groupe donneur.

Cette première observation s'explique par le décalage vers le rouge du spectre de fluorescence du groupe $D\delta_+$ par rapport à celui de $D\delta$, qui supprime tout overlap entre ce dernier et le spectre d'absorption de A, ce qui élimine la possibilité de transfert d'énergie par résonance de type Förster.

La durée de vie de l'état transfert de charge semble principalement impactée par la présence ou non de l'amine terminale δ_-: en effet dans les molécules où cette amine est absente, le temps de vie de l'état transfert de charge observé est d'environ 400 ps, alors qu'il est de plus d'une nanoseconde en présence de δ_-. Les effets des groupes δ_+ et δ_- sont résumés par la figure 4.20, qui montre la formation et le déclin de l'état transfert de charge.

La longueur du groupe donneur ne semble en revanche pas avoir d'impact majeur sur la dynamique des molécules étudiées, la seule différence étant la proportion et la signature des états triplets formés.

Ces dernières observations semblent pouvoir s'expliquer par la théorie de Marcus, qui entre autres, permet de relier la durée de vie des états transfert de charges à la distance séparant les orbitales moléculaires hautes occupées (HO) et basses vacantes (BV) des groupes donneurs et accepteurs. Les premières simulations réalisées par l'équipe de Irene Burghardt semblent corroborer nos résultats: en effet, même si toutes les molécules n'ont pas encore été modélisées, on observe bien un effet de l'amine sur la localisation de la HO, l'éloignant de la BV de 'accepteur, et donc réduisant le taux de recombinaison des charges. De même on observe que la HO se localise principalement à proximité de l'espaceur δ ou δ_+, et n'est donc que peut affectée par la longueur du groupe donneur.

Ces résultats semblent encourageant, puisque dans le meilleur cas (en présence de δ_-), le temps de vie de l'état transfert de charge dépasse la nanoseconde, c'est à dire un gain d'un facteur 20 par rapport à la précédente génération. Les prochaines étapes de l'étude, en plus des modélisations moléculaires, seront donc d'étudier d'une part les molécules $\delta_-D_0\delta A$ et $\delta_-D_2\delta A$, pour lesquelles la longueur du donneur devrait effectivement modifier la distance HO-BV, et d'autre part les mêmes molécules en films. L'étude des molécules en films va de paire avec le travail des équipes de Martin Brinkmann et Nicolas Leclerc, qui étudient la structuration de ces différentes molécules en fonction des conditions de dépôts.

0.2.4 Conclusions et perspectives

Plusieurs observations peuvent être tirées de ces travaux. Un premier point est l'intérêt de l'accès à plusieurs expériences complémentaires, ce qui permet d'identifier les contributions des différentes espèces dans les données "pompe-sonde", même dans les cas où ces contributions

sont intriquées. Un second point est l'intérêt d'une étude approfondie des molécules développées, en plus d'une étude de leurs performances photovoltaïques, puisque cela permet de comprendre les points limitant ces performances et de les améliorer par la suite.

Part I

Introduction

1

Photovoltaics

1.1 Energy source shortening, interest of photovoltaic power

As both world population and living standards increase, energy needs rise drastically (grew by 26% between 2000 and 2010, and is projected to rise by 20% by 2020). Among that energy, the share of electricity is also growing more important: if 42% of the energy produced in 2012 was electricity, this ratio is planned to reach two-thirds by 2035. This trend triggers an important need for electricity production. Yet, most of the energy is still produced by "conventional" methods: by the end of 2012, more than 78% of the consumed energy in the world comes from fossil fuels and about 3% from nuclear power[1]. Unfortunately, fossil fuels are in limited amounts, and conjunction of both an increased demand and a reduced production can only lead to skyrocketing costs. In actual economy, this factor is probably the more deterrent one, but ecological considerations about CO_2 emissions and global warming are also a major concern. If the nuclear production is economically much more efficient, and is theoretically sustainable[2], it does imply heavy investments to be built and to be kept safe, suffers from a very bad public image, and poses yet to be resolved problems with the wastes (and complicated political problems).

Several alternatives exist : hydraulic and geothermal are the most usual, but newer solutions are developing, as wind-mills, solar concentration, biodiesels,... and photovoltaics. Each of these solutions have their pros and cons, for example hydraulics and geothermal stations cannot be built just anywhere, but the latter seems the most promising, provided we can get rid of some limitations (mostly fabrication costs, both in term of energy and money).

Indeed, given the huge amount of irradiation from the sun (over 1.3kW/m^2 in average), solar energy is almost unlimited, free, and renewable (at our scale). Putting aside fabrication costs, generation of electricity from a simple solar-panel makes it easy to provide electricity anywhere (given some sunlight), which makes it outright the best solution for off-grid areas. On-grid production may pose a bit more problems, as one have to compensate fluctuation in energy production to match energy consumption at any moment, be it with an over-scaled production and large amount of batteries, or with additional and controllable energy sources.

Photovoltaic energy production rose from 2.2GW in 2002 to 100GW

in 2012, but still represents less than a percent of the world energy production (about $1.7*10^{13}$W).

1.2 Standard photovoltaic cells

The most common solar cells are made with doped silicon, and are based on P-N junctions. The first photovoltaic effect was observed by A. and E. Becquerel in 1839 while studying a chain of conductors under illumination. This effect was later explained in 1905 by A. Einstein.

A scheme explaining the principle of such cells is represented in Fig.1.1. On the left - graph. A) - two separated crystals are represented, one P-doped on the left, with additional "free-holes" and a Fermi level close to the valence band, and one N-doped, with additional "free-electrons" and a Fermi level closer to the conduction band. When those two differently doped materials are put together - graph. B) - a P-N junction is formed, creating a diode effect better seen on C). Using different electrodes on each sides, usually Aluminum and ITO (Indium Tin Oxyde) creates an additional electric bias, that leads photo-induced charges to their respective electrodes as pictured in D).

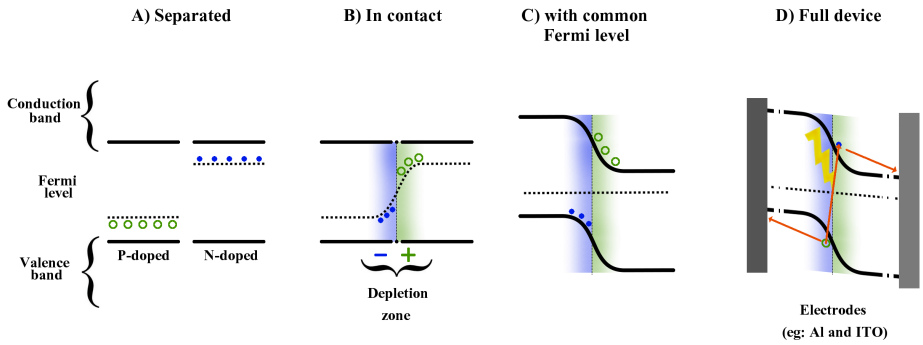

Figure 1.1: Schematics of P- and N-doped semiconductor energy bands, and typical Si Solar cell principle. A) Valence and Conduction bands of N- and P-doped Si crystals. B) when in contact, excess charges from one moiety may diffuse to the other, creating a depletion zone and a local charge. C) equalizing the Fermi level of both sides, we see that we create a bias in the valence and conduction bands that will separate the charges when D) a photon is absorbed.

1.3 Silicon cell performances and limitations

Such cells have been widely developed in the last 50 years, to reach very high efficiencies (>40%[3]) with multi-layer cells, combining several P-N junctions layers with complementary absorption spectra. Yet, these cells are extremely costly to produce, both in terms of energy and money, due to the fabrication process involving (among other factors): extreme purification of Si, creation of mono-crystalline wafers, precise doping using rare materials,... The high financial cost reduces drastically the application domains for such cells, and the time needed for a cell to produce again the energy spent in its fabrication (usually from 5 to 10 years) make it more a "battery" than an energy production source if no correct maintenance is done.

Variations of these cells were made, using cheaper materials (poly-crystalline Si), or less materials (thin-film crystals) but at the cost of a lowered efficiency (15-20%), and they still need several years to pay-off.

Plus, another factor to account for is that such cells are costly to recycle, as they need treatments similar to those used for the construction (chemical or thermal peeling of protective layers and electrodes, melting and purification of Si wafers,..), further reducing the overall investment-profit balance of the Si-based cells.

Fig. 1.2 sums up the best efficiencies obtained for several solar-cells technologies along the 40 last years. This only shows the efficiency of cells, but already indicates that new cell-technologies (orange curves) are developing quite fast during the last few years. In the following some of these new solutions will be described, that do not suffer from the limitations of crystalline cells, and should soon become efficient enough to be competitive.

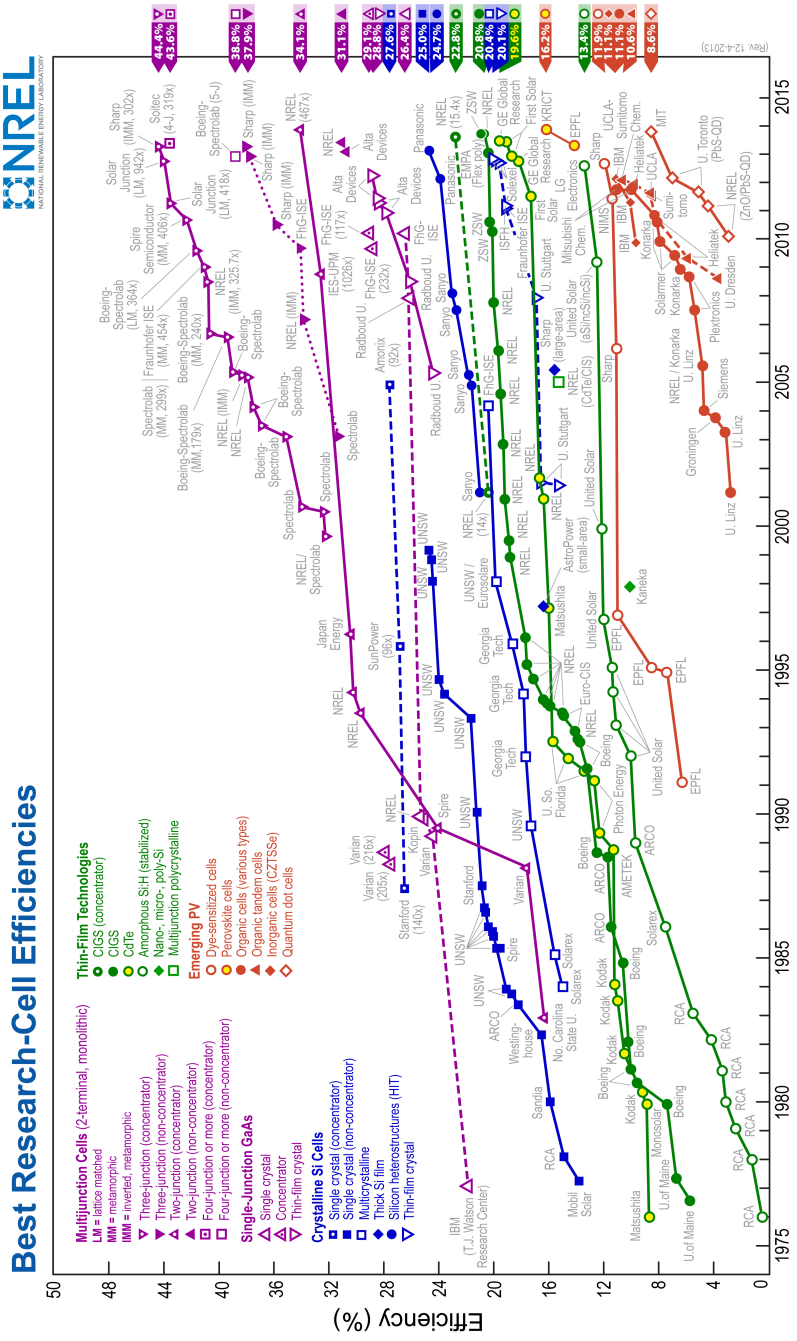

Figure 1.2: Summary of the different cell technologies best results by year (source: www.nrel.gov/ncpv). One can see that very few progress was made on mono-crystalline cells (both on Si and Ga) during the past 20 years, and that most progress in inorganic cells comes from improvements in the "stacking" of junctions to form multi-layer cells or better fabrication processes for thin-films. On the other hand, new alternative solutions (orange curves in the lower part of the graph) are undergoing an important growth in the last few years.

1.4 Alternatives

As said previously, "classic" solar cells are mainly limited by their main constituent: the substrate (Si in general), that may break, need to be highly purified, carefully doped,... Several alternative solutions were invented to avoid these aspects, some inspired by natural phenomena (Dye-sensitized cells), or by the classical cells but with an organic implementation.

1.4.1 Dye-sensitized solar cells

Dye-sensitized solar cells (DSSC), or "Grätzel cells" from the name of their inventor[4], were discovered while studying photosynthesis and the photo-oxidation of chlorophyll. In such cells, as depicted on Fig. 1.3, a porous semiconductor is deposited on the internal surface of a transparent electrode, and covered with dyes. Theses dyes are used as electron donors upon photo-excitation. The missing charge on the dye is then replaced -faster than the geminate recombination- by an electron coming from the electrolyte that fills the cell, enclosed by the second electrode. The electron given to the semi conductor diffuse to the transparent electrode, and then may go through an electrical circuit to go back to the second electrode and back to the electrolyte.

This process is working thanks to the speed at which electrons from the electrolyte replace those given by the dyes, which is possible only due to the small size of the dyes that allows immediate contact between the electrolyte and the depleted molecule. As the efficient part of the cell is made of dyes, one has to make that absorbing part the thickest possible, while maintaining the possibility for the electrons to diffuse to the electrode. This implies a very high surface area on which to graft the dyes, while maintaining electrical contact: this is achieved with transparent nanoporous materials, such as TiO_2.

This technology main advantage is a much lower fabrication cost for a rather good conversion efficiency (above 10%[5,6]), but it still suffers from several disadvantages, mostly due to the liquid electrolyte (usually based on iodide[7]) that may pose stability problems at low (freezing) or high (evaporation) temperatures, which may lead to structural damages and leaks (opening the circuit and stopping any production), leaving a lot of optimization work on the electrolytes[8]. Besides, the fabrication of large surface of nanoporous transparent electrodes and

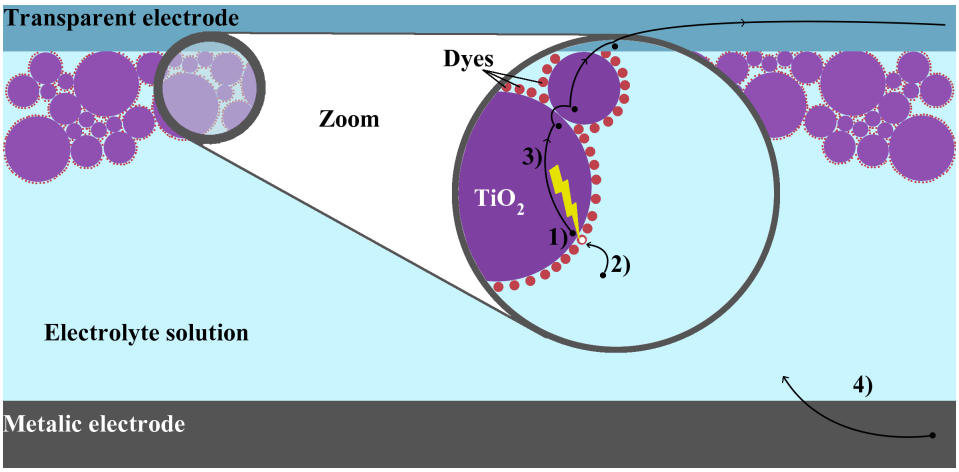

Figure 1.3: Scheme of a typical Grätzel cell. An electrolyte fills the space between a transparent and a metallic electrode. A conducting porous material (usually TiO_2) is used to obtain a very high surface area on the transparent electrode, sensitized by a dye. Upon absorption of a photon, a dye may transfer an electron to the TiO_2 (1), before recombination occurs, an electron from the electrolyte may fill the hole in the dye (2), leaving an excess electron in the TiO_2, that can drift to the electrode (3) and then an electrical circuit, to come back on the counter electrode and return to the electrolyte (4).

sealing of the electrolyte is not so easy to allow for a facile mass production as another solution: the organic solar cells.

1.4.2 Organic materials

Under the name of "organic materials" lies a lot of various cells types, but they share a common trait: the use of an organic molecule (be it small molecules or polymers[9]) to act as the semiconductor of classical cells[10,11].

The basic idea[12] is to place a layer of an organic material[13] between two electrodes (one of which is transparent), with different work functions, inducing an electric field within the material. These materials consist in conjugated systems, selected so that upon photo-excitation an electron may be promoted from the highest occupied molecular orbital (HOMO) to the lowest unoccupied molecular orbital (LUMO) of the molecule, creating an exciton (an electron-hole pair, slightly separated but still under interaction). If this state lives long enough, the conductivity of the material is high enough and the electrical field is intense enough, the charge may be separated into free charges, that

can migrate to the electrodes.

This is made possible by the very high extinction coefficients of conjugated molecules, that allow to reach very high optical density with very thin layers (hundredth of nanometers), thus limiting problems related to the low conductivity of organic materials, and allowing intense electrical fields, given the small distance between electrodes.

The main advantage of these cells is that one can "print" the cells by depositing a film of the organic material, optimally by roll-to-roll processes. Adapting such rotary printing press allows to produce large surfaces at a very low cost, as (almost) all the expenses reduce to the materials (electrodes and ink). Lower costs imply that one can accept a lower efficiency from the cell and still make it beneficial. Another gain is that the fabrication of such cells imply wet chemistry and no heavy pollution is expected.

The most common solution with organic materials is to mix 2 different species, one acting as an electron donor and one as acceptor: at the interface between the two, the charge separation can take place. To optimize this process[14], one needs to maximize the interface surface, and several solutions exist. Some imply the careful mix of 2 polymers (one polymer and small molecules), in which case the organization comes from phase separation and eventual annealing. Others imply the use of organized molecules, such as polymers alternating donors and acceptors groups, or liquid crystals that self-assemble in the desired configuration.

2

Ultrafast Spectroscopy

2.1 Interest of ultrafast spectroscopy

The physical phenomena we are investigating are extremely fast, the longer time scales implied would be the lifetime of the charge transfer states, in the pico- to nano-second scale. Other processes implied, like energy transfer are even faster and go to the femto-second scale. Usual detectors, like ultra-fast photo-diodes can have a rise time in the order of tens of pico-seconds. This is by far not enough to resolve all the phenomena and thus, alternative solutions had to be developed.

For this thesis, two different time-resolved setups were mainly used: a streak camera giving access to the (time-resolved) fluorescence of the molecules, and a pump-probe setup revealing more informations with a better time resolution, but more complicated to decipher. Besides these time-resolved techniques, other spectroscopy techniques were used, as the spectro-electro-chemistry (done in Stuttgart, by Adrian Ruff, Olena Yurchenko and Beatrice Omiecienski, from the team *Functional Polymers*, lead by Sabine Ludwigs), in order to get more insight on the studied molecules. This combination of different techniques allows to clearly identify the chemical species that we observe.

2.2 Streak Camera

The streak camera is an instrument that allows to get a time resolution (down to some ps) on the fluorescence of a sample, and that thanks to amplification possibilities allows to work even on samples with low fluorescence quantum yield.

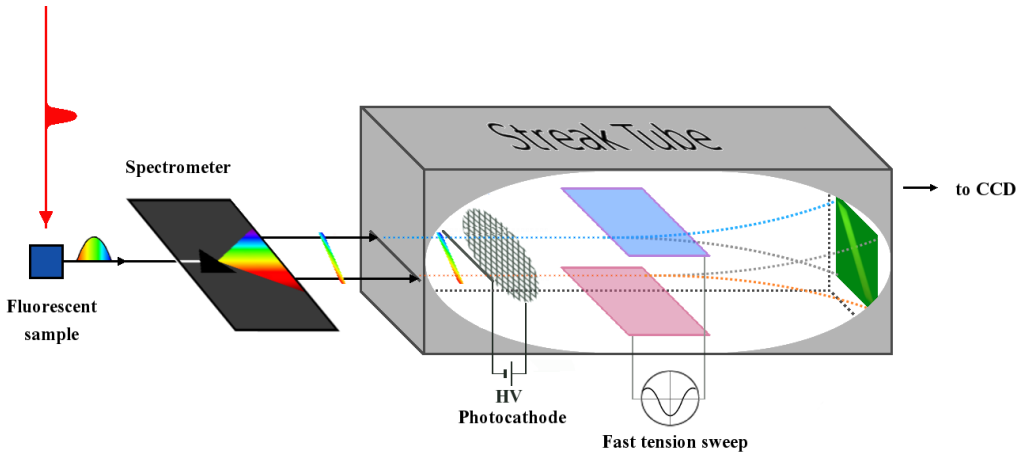

Figure 2.1: Schematic of the streak camera setup. An incoming pulse excites the sample that emits its characteristic fluorescence, which is collected and sent first to a spectrometer, in order to get spectral resolution along the horizontal axis. This line is sent to a photo-cathode that converts incoming photons into electrons, keeping the spectral resolution along the horizontal axis and emitted with the same time dependence as the incoming fluorescence. The resulting electron beam travels between 2 electrodes on which a fast tension sweep (synchronized with the laser pulses) is applied, deflecting the electrons according to the time at which they were emitted along the vertical axis. The resulting electron beam can be amplified by a Micro Chanel Plate (MCP) before arriving on a fluorescent phosphor screen, converting electrons into photons again. That phosphorescence reflects both the spectral and time resolution of the fluorescence and can be recorded by a CCD camera.

A schematic of the Streak Camera setup is pictured on Fig. 2.1. The fluorescence of the sample is triggered by a laser pulse, and collected. If that fluorescence was to be sent to a detector ”as is”, one could not spectrally resolve it, and the time resolution would be limited by the detector response time. Using a spectrometer one gets the spectral resolution, as the fluorescence is spread axially depending of its wavelength (here, horizontally). This spectrally resolved fluorescence is

then sent in the streak tube, that will give us the time resolution along the other axis (here, vertically). The streak tube achieves this in 4 steps. The first consists in the conversion of the incoming photons into electrons with the help of a very sensitive photo-cathode and a grid, so that a large fraction of incoming photons is immediately converted into accelerated electrons. The second step is the most characteristic of the streak camera: in order to achieve the time resolution, those electrons are sent between 2 plates to which a fast tension sweep is applied. The electrostatic force will deflect the electrons according to the generated electric field. The fluorescence is spread on the vertical axis by synchronizing the electric sweep with the laser pulse, so that the sweep starts with the beginning of the emission (plus a delay accounting for the propagation time from the sample to the streak tube). The two last steps are the amplification of the sample with a Micro Chanel Plate (MCP) and the conversion into photons with a fluorescent phosphor screen. The fluorescence achieved on this screen will reflect along the horizontal and vertical axis respectively the spectral and time dependence, and is recorded with a CCD camera.

Our streak camera is a HAMAMATSU streak camera C10627, and offers a time resolution of 0.5% of the time range scanned except for the smallest range, which is 1 ns, this mean that we can achieve a 10 ps resolution.

The main advantages of the streak camera compared to the pump-probe spectroscopy (described further) lie in the relative easiness of the experiment, and in the interpretation of the results. Indeed only the fluorescence of the molecule is observed, and no doubt lies about the possible superposition of different contributions (as induced absorption), which can be very helpful for interpretation of pump-probe results. Beside, the observation of fluorescence itself brings a lot of informations, about anisotropy, energy transfer, etc.The same informations could be obtained, with better time resolution, through a broadband fluorescence up- (or down-) conversion spectroscopy[15–17], but at the cost of a much more complex experiment.

2.3 Pump-probe spectroscopy

2.3.1 Principle of pump-probe spectroscopy

The idea behind time resolved spectroscopy is to unravel the dynamic of a sample through its optical properties. Indeed, the absorbance $A(\lambda)$ of a species is given by the Beer-Lambert law in Eq.2.1:

$$A(\lambda) = \epsilon(\lambda).c.d \tag{2.1}$$

Where $\epsilon(\lambda)$ is the exctinction coefficient of the molecule (in $M^{-1}cm^{-1}$), c is the molar concentration (in M), and d is the sample thickness (in cm).

If we have many species in the sample, the total absorbance is the sum of each species, Eq.2.2:

$$A(\lambda) = \sum_i \epsilon_i(\lambda).c_i.d \tag{2.2}$$

And if the concentrations are changing, as in the case of a photoreaction where one goes from the fundamental state of the molecule to excited states and possible photoproducts, this becomes Eq.2.3:

$$A(\lambda, t) = \sum_i \epsilon_i(\lambda).c_i(t).d \tag{2.3}$$

These equations assume that the $\epsilon_i(\lambda)$ do not depend on time, which is usually a good approximation for delays t > 10 ps, when intra- and inter-molecular relaxation is accomplished. Thus, monitoring the changes of absorbance in time of a sample allows not only to get information about the species in the sample, but also their dynamics: if we now compare the absorption at any given delay Δt with that of unexcited molecules (with concentrations c_{i0}), the differential absorption recorded becomes Eq.2.4:

$$\Delta A(\lambda, \Delta t) = \sum_i \epsilon_i(\lambda).(c_i(\Delta t) - c_{i0}).d = \sum_i \epsilon_i(\lambda).\Delta c_i(\Delta t).d \tag{2.4}$$

And ΔA give a direct access to the concentration changes Δc_i.

The problem is that, as said before, the phenomena we are interested in are extremely fast, and the changes in absorbance cannot be recorded by classical ways (as flash photolysis, where the time resolution limitation comes from the detector response time, typically in the nanosecond time scale). The pump-probe technique allows to overcome this limitation, as the time resolution is only limited by the laser pulses duration. The idea is to send 2 pulses to the sample. One pulse starts the photo-reaction (called "pump pulse") and at a controlled delay Δt after, another pulse (the "probe pulse") is sent to measure the sample absorption. This "probe pulse" always probes the absorbance of the sample at this same Δt time, so the recording device (a CCD camera or a diode array) can be slow without giving any loss in time resolution, it will simply average over some pulses.

The signal detected by the recording device is the spectrally resolved probe that went through the sample. Thus, if we have an initial probe intensity $I_0(\lambda)$ at λ, Eq.2.3 tells us that the intensity recorded $I_p(\lambda,\Delta t)$ when the sample was excited Δt femtoseconds earlier is Eq.2.5:

$$I_p(\lambda,\Delta t) = I_0(\lambda).10^{-\sum_i \epsilon_i(\lambda).c_i(\Delta t).d} \tag{2.5}$$

If we now cut the pump beam (usually with a chopper plate), the sample is no more excited, the concentrations $c_i(\Delta t)$ become c_{i0}, and the intensity recorded with no pump I_{np} is Eq.2.6:

$$I_{np}(\lambda,\Delta t) = I_0(\lambda).10^{-\sum_i \epsilon_i(\lambda).c_{i0}.d} \tag{2.6}$$

We now calculate the log of the ratio between those two intensities, Eq.2.7:

$$\Delta A(\lambda,\Delta t) = \log\left(\frac{I_{np}(\lambda,\Delta t)}{I_p(\lambda,\Delta t)}\right) = \sum_i \epsilon_i(\lambda)(c_i(\Delta t) - c_{i0})d \tag{2.7}$$

Which is the differential absorption spectrum $\Delta A(\lambda,\Delta t)$ determined sooner in Eq.2.4.

The pump-probe spectroscopy got a lot of success thanks to technological development, as lasers producing ultra-short pulses (under the

100 femto-second range) are nowadays commercially available, giving "easy" access to time resolutions below 100 fs.

2.3.2 Pump-probe spectroscopy setup

The pump-probe setup is sketched in Fig.2.2.In our setup[18] ultrashort pulses are generated in a *FemtoLasers Synergy 20* Ti:Sapphire oscillator, producing pulses centered at 800 nm, with a full width half maximum of 40 nm, a duration of ~20fs at a 60 MHz repetition rate, and with an energy per pulse of $\sim 1,2.10^{-9}$J.

Those pulses are then amplified in a Chirped Pulse Amplifier (CPA) *Amplitude Technology Pulsar*, so that we get 40 fs pulses with an energy of 4.10^{-4}J at 5 kHz.

The laser beam is split in two : one that will be used for the pump, and one for the probe. The pump has to be adapted to the absorption properties of the sample one wants to study, so it is possible to send it either in a β-barium borate (BBO) crystal to produce a 400-nm pump beam by Second Harmonic Generation (SHG), or in a Non-collinear Optical Parametric Amplifier (NOPA) to obtain other wavelengths. The desired pump is then sent to the sample. The probe beam goes through a delay line that allow us to adjust the time at which the probe will scan the sample, from 0 to 5ns after the pump, with 13 fs steps, defining our Δt. With a CaF_2 or a sapphire crystal, the 800nm probe is converted into a white-light continuum (300-1000nm) through White Light Generation (WLG). All those non-linear processes (SHG, WLG and NOPA) will be detailed in 2.3.4.

This minimal setup would give access to the desired informations : absorption of the sample at any time after excitation or without excitation (meaning, when probing the sample before the pump excites it) can be recorded, giving access to ΔA. But it can be greatly improved in terms of signal to noise ratio and sensitivity limits by adding a chopper on the pump and by using a reference beam, which will be detailed in the following section 2.3.3.[19]

2.3.3 Noise reduction

The amplitude of the spectra that are recorded is limited by the dynamic range of the CCD and the fact that the power of the probe should remain small compared to that of the pump. Furthermore, the

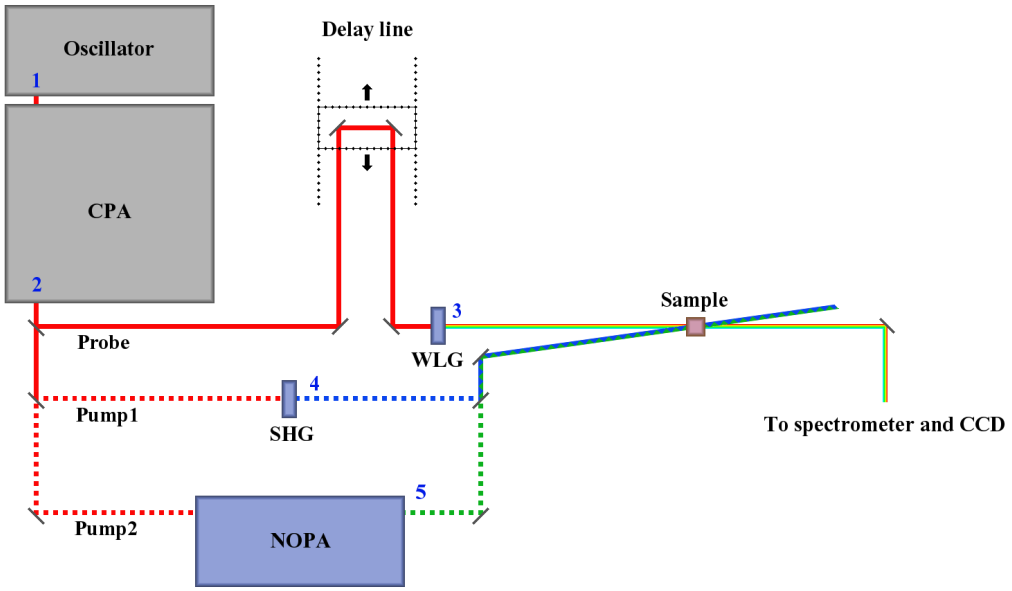

Figure 2.2: Schematic of the pump-probe setup. Pulses(1) are generated in the oscillator, amplified in the CPA(2) and split in 2 beams. One of the beam is sent to the delay line and then through a CaF_2 or a sapphire crystal to generate the white light (WLG) to be used as the probe(3). The second beam will be used as the pump and, depending of needed wavelength, is sent either to a BBO crystal for SHG(4), or in a NOPA(5). Both beams are then sent on the sample. Characteristics of the pulses at the different steps (figures) can be found in table2.1

changes in those spectra are small due to both the relatively small optical density of the sample (the probe still need to be transmitted) and the limited power of the pump, as we want to excite only a few percents of the molecules to remain in a linear regime of excitation. This results in the amplitude of our signal to be very small: the amplitude of ΔA is in the range of milli-OD (OD of the sample is usually around 0.1 OD, and about 1% of the sample is excited). This means that we have to record the very small changes of an already weak probe, thus the extreme importance of reducing the noise as much as possible. Beside the noise coming from the sample (diffusion of the pump, bubbles in flushed liquid samples or inhomogeneities in solid ones,...), noise mainly comes from both the probe and pump laser pulses : variations of the probe spectral features from one measurement to the next, or pump-power changes would be -wrongly- associated to concentration changes in the sample. This noise can be reduced by two tools : choppers and

a reference beam.

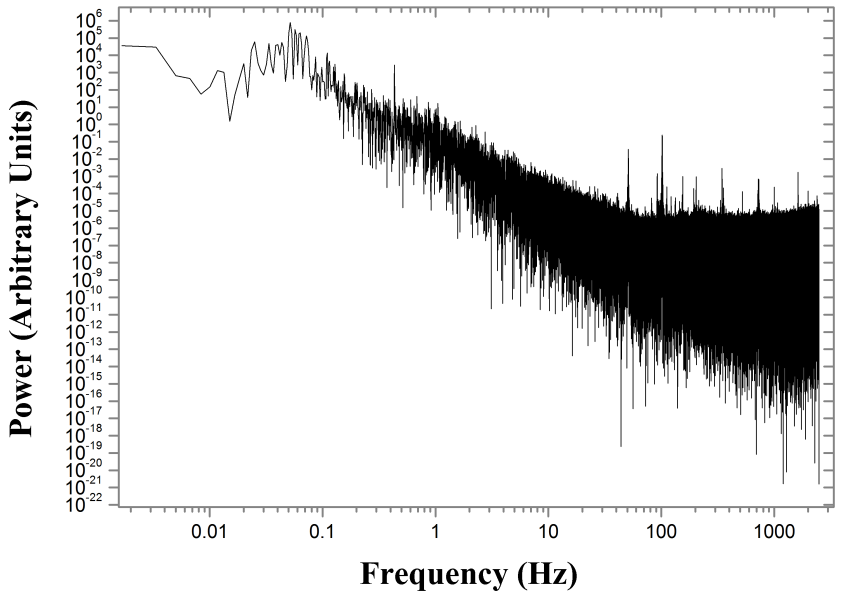

Figure 2.3: Spectral repartition of the noise on the pump power. This spectrum was obtained by recording the fluctuation of the power of the pump at 400nm during 2 minutes and then calculating the FFT.

Noise in the laser pulses is shown on Fig.2.3: recording the power of each pulses for 2 minutes (about 600000 pulses) and calculating its FFT show that most of the variations are slow (mainly resulting of thermal effects in the laser setup, under a few tens of hertz). The influence of these slow drift compound is eliminated by doing each measurement on a time scale much shorter than the drift . This is achieved by placing a chopper at the entrance of the detector, cutting the probe beam at a frequency of ~ 227Hz and reading the CCD detector accordingly. Doing so means that each reading of the CCD (meaning "one spectrum") is done in about 4.4ms, a time scale on which there is virtually no fluctuations of the power, effectively removing any "slow noise" on the probe. Additionally, this allows to read the CCD chip without adding any more photons on it. Unfortunately, this corrects the noise on one single spectrum, but what we are interested in is the differential spectrum "with/without pump". If we were to use only this chopper, each recorded spectrum would be "clean", but slow changes in the probe would still be recorded from one measurement to the next,

changes that wouldn't be induced by the sample. To avoid that effect, another chopper is placed on the pump beam, at half the frequency of the previous one ($\sim$ 113Hz). Doing so allows to record sequentially the absorption of the sample with (I_p from Eq. 2.5) and without pump (I_{np} from Eq. 2.6) every $\sim$ 9ms , as shown on Fig2.4, removing any effect of fluctuations slower than that.

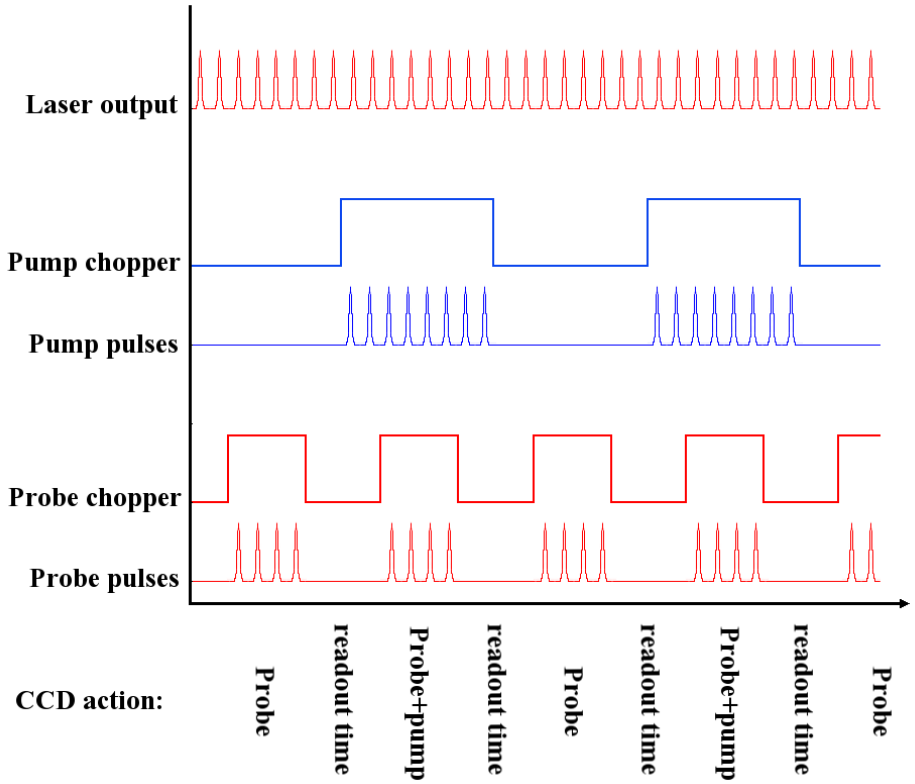

Figure 2.4: representation of the sequences of pulses. The 5kHz pulses are chopped so that the pump irradiates the sample half of the time. A second chopper is placed in front of the CCD in order to clearly separate pump + probe and probe only acquisition, and insure that no light arrives to the CCD during reading time.

Those two choppers take care of the slow variations, but pulse to pulse variations remain, and we can further improve the signal to noise ratio by measuring and correcting for them. This is achieved by the use of a reference beam. The reference beam is obtained by splitting the probe beam in 2 (one that is the actual probe, and the other that becomes the reference). This reference beam does not go through the sample, and is here to monitor the probe spectrum fluctuations. In-

	1	2	3(CaF_2)	3(Sapphire)	4	5
Frequency	80MHz	5kHz				
central wavelength	800nm		300-900nm	400-1000nm	400nm	240-2600nm
typical FWHM	50nm		broadband	broadband	40nm	30nm
typical pulse duration	40fs	40fs	70fs	70fs	45fs	40fs

Table 2.1: Characteristics of the pulses at different points in the setup (figures from 1 to 5 relates to those in Fig. 2.2). Probe pulses (3) are really broad continua, but only reduced bands of ~ 300nm are used at once, in order to use an optimized (stable) spectrum. NOPA generated pump pulses (5) are now generated by a Light Conversion TOPAS-Prime optical parametrical amplifier.

deed, there are variations from one laser pulse to the other, which lead to even larger variations in the white light generated. Those variations are recorded by the CCD but are not part of our sample's dynamics, and thus we want to get rid of them. If the reference beam is correctly aligned with the probe beam, so that it enters the spectrometer and the CCD in a similar way (but on a different strip of pixels), we can record the changes in the reference continuum, and use them to correct the probe fluctuations. If this alignment is correct, one can drastically reduce the noise in the signal, reducing the peak to peak variations by a factor 2, down to $3 * 10^{-3}$, which is again reduced by averaging the spectra over several measurements (usually 50, reducing the noise to below $5 * 10^{-4}$). This reference-correction is even more useful when we scan different delay times: slight changes in the probe beam path (beside the total length) may alter the continuum generation, which is also taken care of by this correction.

Some other sources of noise coming from the CCD can be mentioned: dark noise, shot-noise and read-out noise. As the measurements are fast and the CCD chip cooled (at $-60°C$) the dark noise is negligible. Setting the chip on "low gain" and "high capacity" also improve the S/N ratio, as it allows to convert many photons in few electrons (low gain) and to count a lot of electrons (16 bits, meaning a dynamic range spreading from 0 to 65536), meaning that instead of doing lots of "few photons readings" we can measure a lot of photons at once, reducing the shot noise and the readout noise.

2.3.4 Non linear optic: SHG,WLG, NOPA,...

Besides the laser pulses generation, non linear effects are also involved in two other main parts of the pump-probe spectroscopy: the White Light Generation (WLG) that creates the continuum of the probe, and the generation of the pump, either via Second Harmonic Generation (SHG), or a Non-collinear Optical Parametric Amplifier (NOPA).

The white light generation is a complex process in which an input beam spectrally broadens while propagating in a high third-order susceptibility (χ^3) medium. A detailed description can be found in[20]. Briefly, the phenomenon is mainly governed by Self-Phase Modulation (SPM): the index of the material changes with the intensity of the pulse, as that field is not only space dependent but also time dependent, the index becomes time dependent, which in turn impacts the phase of the pulse. The pulse electric field frequency gets shifted by that phase modulation, resulting in a time dependent (within the pulse duration) frequency shift proportional to the pulse envelope derivative ("steeper" pulses would produce larger shifts). For our setup, 2 different crystals where used for WLG: a CaF_2 crystal that allows generation of a continuum ranging from ~300 nm to ~900 nm, and a Sapphire crystal that was limited to ~400 nm in the UV side, but allows to reach IR wavelengths up to ~1000 nm.

Second Harmonic Generation[21] is a second order polarization effect (implying χ^2) where a pulse at frequency $\omega_{SHG} = 2\omega_0$ is generated from a first pulse at a frequency ω_0. Several conditions have to be met in order to generate this SHG. First of all, a medium with a non-zero χ^2 is needed, which implies a non-isotropic crystal without inversion center, in our setup a Beta Barium Borate (BBO) is used. Second, as the χ^2 is much smaller than first order susceptibility, we need a very intense electric field to observe any effect, which is not much of a problem with femtosecond pulses. Third, energy conservation has to be respected. As a photon at $2\omega_0$ has twice more energy as a photon at ω_0, 2 photons have to be annihilated for every 1 created photons. Finally, as the intensity of the generated pulse is varying as $sinc(\Delta k)$, with $\Delta k = k_{\omega_{SHG}} - 2k_{\omega_0}$ and $k_\omega = n(\omega)\omega/c$,maximum intensity is achieved when we meet phase-matching conditions within the crystal, c.f. Eq.2.8:

$$\hbar k_{\omega_{SHG}} = 2\hbar k_{\omega_0} \tag{2.8}$$

This implies that we need a material where $n(2\omega) = n(\omega)$ to propagate the beam. This is possible in birefringent materials (such as

the BBO) that have an ordinary and an extraordinary axis, with different refractive indices. Propagating the incoming linearly polarized photons along the ordinary axis (with an index $n_{ord}(\omega)$), we can obtain the SHG along the extraordinary axis (with an index $n_{ext}(2\omega) = n_{ord}(\omega)$).

Besides the SHG that allows us to get a pump-beam at 400 nm, we also use a Non-collinear Optical Parametric Amplifier (NOPA)[22] to generate other wavelengths (from 400 nm to 800 nm, which can in turn be doubled via SHG). This system makes use of similar processes as in the SHG, but with different conservation of energy and k-vector, as shown in Eqs.2.9 and 2.10, where indexes p, s and i denote respectively the pump, the signal and the idler (respectively the resulting wavelengths with the highest and lowest energy).

$$\hbar\omega_p = \hbar\omega_s + \hbar\omega_i \tag{2.9}$$

$$\hbar k_{\omega_p} = \hbar k_{\omega_s} + \hbar k_{\omega_i} \tag{2.10}$$

In terms of energy, this means that instead of creating one high energy photon out of 2 half-energy photons, a high energy photon can generate 2 lower energy photons with different energies. For example, a pump photon at 400 nm could generate one at a wavelength between 400 nm and 800 nm which will be our signal, and a second one wielding the missing energy in the infrared, the idler. This would be Optical Parametric Generation. In our case we use Optical Parametric Amplification: the signal is already present (through WLG), and a part of this broad spectrum is amplified. A detailed analysis of the OPA phenomena (both in collinear and non-collinear configuration) can be found in[23]. To sum it up, making use of the birefringence of a crystal (usually made of βBarium Borate, BBO), one can match the conditions of Eqs.2.9 and 2.10 for a given pump wavelength and a desired signal wavelength, through tuning of both the incidence angle of the beams and the crystal orientation. Sending a pump-pulse (generally a UV pump achieved through SHG) and a broad pulse (obtained through WLG) to the crystal, the pump signal may interact and amplify the spectral components of the broad pulse that respect the phase-matching conditions, thus amplifying a given spectral range in this broad pulse. A schematic of a classical OPA (or NOPA if $\theta \neq 0$) is shown in Fig. 2.5.

Using the non-collinear conformation allows for a spectrally broader

amplified signal: indeed in an OPA, all three components (pump, signal and idler) are collinear, and do not propagate at the same speed. This drastically reduces the parameters one can tune to match the conditions of Eqs.2.9 and 2.10, and results in a rather small spectral band for amplification. In the non-collinear conformation, one can change the angle between pump and signal propagation direction(s) so that in the BBO the projection of the idler group velocity along the signal propagation direction matches the signal group velocity. In such case, the phase matching condition is verified on a much broader spectral width, and allows to generate broader signals.

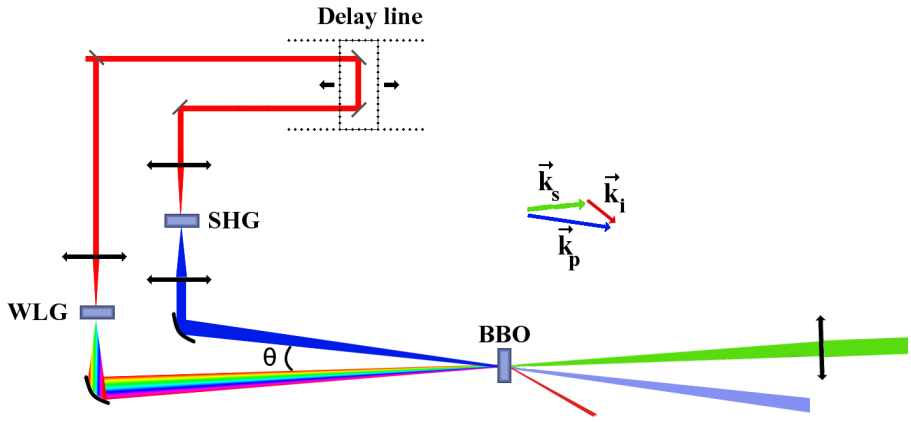

Figure 2.5: Schematic of a (Non-collinear) Optical Parametric Amplifier: the original 800 nm beam is split in two beams: one used for WLG and another for SHG. The later is used as pump to transfer its energy into the spectral component of the former that matches the equations 2.9 and 2.10 within the BBO crystal. In a non collinear conformation, the angle $\theta \neq 0$. A small delay line allows to adjust the temporal overlap between the two pulses.

2.3.5 Results interpretation, detected phenomena

The 4 phenomena we can infer from the ΔA obtained through the pump-probe setup (Eq. 2.7) are schematized in Fig.2.6 and are : Ground State Bleaching (GSB), Stimulated Emission (SE), Excited State Absorption (ESA) and Photoproduct Absorption (PA).

The easier one to characterize is the GSB : once the sample is excited, there are less electrons in the ground state able to do transitions to higher levels, which reduces the absorption of the sample. This will result in a negative contribution in the ΔA with the same characteristics as the static absorption spectrum. A second phenomenon is the SE: molecules in their excited state may return to the ground sate through emission of photons and amplification of the probe. This will also results in a negative contribution in the ΔA, with the same characteristics as the static fluorescence. The 2 remaining phenomena (ESA and PA) are induced absorptions, as electrons in excited state can now undergo by new transitions to even higher electronic states.

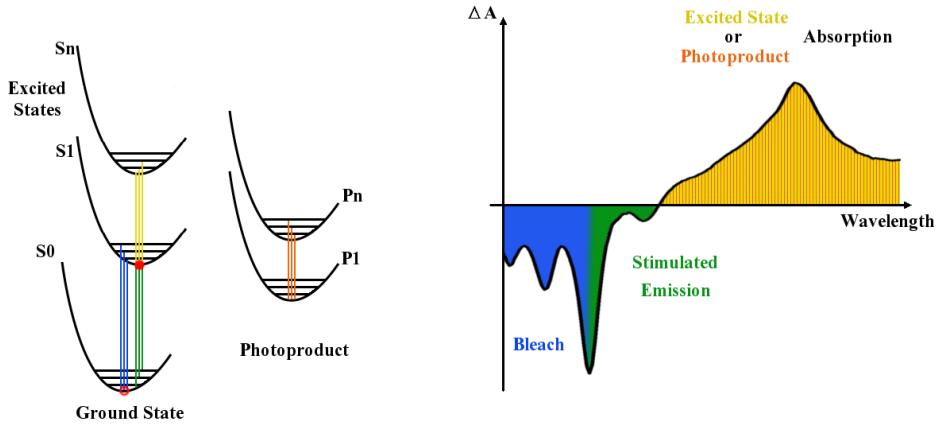

Figure 2.6: implied phenomena in photoreactions and their observable consequences in pump-probe spectroscopy. Excitation of the molecules promotes electrons from the electronic ground sate (S0) toward an excited state (e.g. S1): the transitions from S0 to S1 (in blue), responsible for the static absorption of the molecule, are less probable and thus GSB is observed in the ΔA spectrum. Those excited electrons (in S1) may now go to higher excited states (Sn), leading to new absorption bands (excited state absorption, in yellow), or return to ground state via amplification of the probe (stimulated emission, in green). If the molecule undergoes changes (isomerisation, charge transfer,...), ESA and SE are not possible, instead photoproduct absorption is observed (in orange)

From those observed signals in the ΔA spectra at a given time Δt, we can deduce what is the actual state of the molecules. The GSB is very useful when several species are present in the sample. It is indeed easy to get a static absorption spectrum of the different species, which gives us the ground state extinction coefficient $\epsilon_{GS}(\lambda)$ that characterizes each species. At any time Δt of the photoreaction, if a species is excited in

any way (either by the pump, energy transfer, charge transfer, ...) the population of its ground state c_{GS} is reduced, and thus ($c_{GS}(\Delta t)$-c_{GS0}) get negative, and the ΔA spectra will yeld the $\epsilon_{GS}(\lambda)$.

If the GSB allows the identification of involved species, it does not indicate in which state those species are. To obtain that information, we have to use the other phenomena: SE and ESA of a species that denote its excited state, or PA that indicates a photoproduct (charge transfer state, isomer,...). The Stimulated Emission of a given species can be identified from the static fluorescence spectrum (as defined by relations between Einstein coefficients[24–26]) which can be obtained with a static fluorescence experiment or the streak camera (in which case we also get indication of life time). The ESA spectrum cannot be predicted, but will follow the same dynamics as the SE. If the molecule doesn't goes back to its ground state, the excited state decay leads to the formation of a photoproduct. In this work, the photoproduct will be in most of the cases a charge transfer state, whose absorption can be identified with a spectro-electro-chemistry experiment (c.f. chapter 2.5).

2.4 Data treatment

The data recorded in the pump-probe experiment can be improved with the implementations presented in 2.3.3, but still contain elements that have to be removed before the data can be correctly analyzed. Indeed, even if the noise was reduced, bubbles can seldomly pass through the sample, diffusing a lot of pump and probe light, leading to a random differential spectrum with no sense, similarly, radiation may hit a pixel of the CCD, saturating it and leading to a spike in the recorded spectrum. In some cases the molecule ends its dynamic in a triplet state, which can be extremely long lived. As the sample is probed and pumped at 5 kHz, if this lifetime is over 200 μs, a non-zero differential spectrum will be recorded while probing the negative delay time (instead of really probing at Δt <0, it is probing at Δt= ~200 μs). Beside those 2 effects, the solvent may also give rise to some signal, that have to be subtracted. Finally the refractive index of the materials the probe goes through is wavelength dependent, inducing a group velocity dispersion (GVD). This chirp of the probe pulse results in a difference in the time overlap of the pump and the different wavelengths of the probe, which leads to a distortion of the data (illustrated in Fig.2.7).

2.4.1 Data cleaning

The final differential spectra at each delay Δt are calculated as the average of several spectra recorded for this delay on different scans (e.g. : 5 scans from -1ps to a few ns). If a differential spectrum is invalidated by a bubble (or any other phenomenon) in one scan, its standard deviation std(ΔA) with respect to the same spectra in the other scans will be far over the noise level. So, calculating this std(ΔA) for each spectra of each scan and removing all those above a chosen threshold effectively remove all nonsensical spectra.

2.4.2 Solvant correction

As shown in Eq.2.7, the recorded ΔA spectra will reflect any pump-induced changes in the concentrations, even if the solvent has a small -but not zero- absorption, it is in huge excess and it will also give some signal. Beside, cross phase modulation (XPM) takes place: the pump pulse will induce changes in the probe when both pulses overlap. These

changes as also recorded as part of the signal but are not related to the molecule dynamics and thus have to be removed.

Those contributions are corrected by recording the pump-probe signal on solvent alone after the experiment on the sample of interest. Indeed in this case we record only the signal originating from the solvent, and the cross phase modulation signal is independent of the sample (the phase changes induced by the sample molecules can be neglected), and only change with the exact alignment of the experiment (which imply that we have to do the solvent experiment just after the sample experiment, without changing anything). Then, correction is done by subtracting the solvent's dataset from the sample's one, as shown in Eq.2.11.

$$\Delta A(\lambda, \Delta t)_{cor} = \Delta A(\lambda, \Delta t)_{sam} - fact * \Delta A(\lambda, \Delta t)_{sol} \tag{2.11}$$

Where the index "cor","sam" and "sol" relate respectively to the corrected data, the sample data and the solvent data, and "fact" is a factor to be determined. This factor accounts for the fact that in the "molecule" experiment, a noticeable part of the light is absorbed by the molecule, weakening the solvent's signal.

2.4.3 GVD

As the probe is generated inside a crystal (CaF_2 or Sapphire in our case), and propagates via some reflections, it does get impacted by the non-uniformity of the refractive index versus the wavelength, which results in Group Velocity Dispersion (GVD). As a consequence the bluer components of the probe arrive on the sample after the redder ones. This implies that, if we define the t_0 as the position of the delay line that overlap the pump and the central wavelength of the probe, this overlap will be found in negative times for the bluer wavelengths (the delay line define a shorter path for the probe), and in positive times for the redder ones (longer probe path). This effect is dramatic for spectra interpretation at short times: e.g.: a signal that should rise at the same time in short and long wavelengths will appear to rise first in the shorter wavelengths and later in the long ones. This effect, also called "chirp" can be seen in Fig.2.7.

This effect can be corrected by fitting the chirp (as shown with the black curve on Fig.2.7), which can usually be modeled using the Sellmeier equations. This allows to determine for each wavelength the

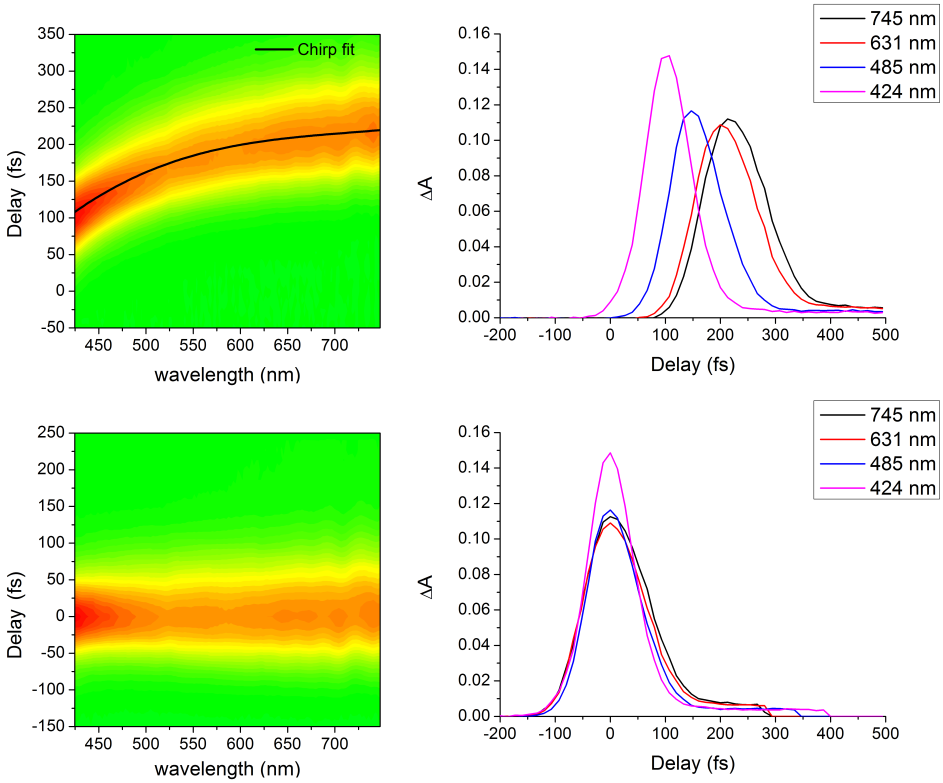

Figure 2.7: Top-left panel: bi-dimensional plot of actual pump-probe results on a ZnS sample, at short delay times, with an important chirp twisting the data: the signal in the red side appears to rise almost 100 fs later than on the UV side, though this signal -arising from cross phase modulation (XPM) between pump and probe pulses- is only present at the actual "zero time" corresponding to the temporal overlap of pump and probe. The black line highlights the position of time zero, defined as the maximum of this XPM signal. Top-right panel: selected kinetic traces that reveal this "temporal shift". Bottom-left panel: the same dataset, after chirp correction: no more twist is to be seen. Bottom-right panel: kinetic traces at the same wavelengths as previously, showing that within a small error, the effects of the GVD are corrected.

amount of time $\delta t(\lambda)$ induced by the GVD. The data is then corrected as shown in Eq.2.12 by interpolating the signal at each wavelength at a new time t_{cor}=t+δt. Results of this correction is shown on Fig.2.7B.

$$\Delta A_{cor}(\lambda, \Delta t_{cor}) = \Delta A(\lambda, \Delta t + \delta t(\lambda)) \qquad (2.12)$$

2.4.4 Data Fitting

Once the data are corrected from any unwanted signals or effects, analysis can be made. The phenomena detailed in 2.3.5 allow to identify the different steps involved in the studied reactions (for example: excitation of a compound A, energy transfer to a compound B, then charge transfer,...), if this is enough to follow the reaction and does give some indications about the time constants implied, it doesn't provide the exact values of the reaction rate. To obtain these, we look at the data not along the spectral axis at some chosen times, but along the time axis at some chosen wavelengths. Doing so shows kinetic traces (as shown in Fig. 2.8, black plain lines), pertaining to the rises and decays of the different populations c_i as expressed in the equations 2.3 to 2.7. We then fit those kinetics with a model function (corresponding to a hypothetical reaction scheme): if the agreement between data and the fit is deemed good, we can use the fitting parameters to precisely describe the molecular reaction. In the following section, the usually used fitting function is described, through the analysis of a simple model reaction. More developed analysis techniques will then be described

2.4.4.1 Fitting function

Assuming a model reaction in which P_0 molecules out of a total population P_{tot} from state S_0 are excited into a first state S_1, decay into state S_2 with a rate constant k_{12}, and this state S_2 relaxes into state S_0 with a rate constant k_{20} (as represented in reaction scheme 2.13), we can write the respective populations c_i as in Eq. 2.13:

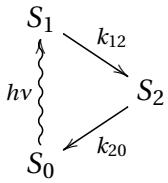

(2.13)

$$\frac{dc_1(t)}{dt} = -k_{12}.c_1(t)$$

$$\frac{dc_2(t)}{dt} = -k_{20}.c_2(t) + k_{12}.c_1(t)$$

$$\sum_{i=0}^{2} c_i(t) = P_{tot}$$

Solving Eq. 2.13 leads to the concentrations following decaying exponentials (Eq. 2.14), for t>0:

$$\begin{aligned} c_1(t) &= P_0.e^{-k_{12}.t} \\ c_2(t) &= \frac{P_0.k_{12}}{k_{12}-k_{20}}.(e^{-k_{20}.t} - e^{-k_{12}.t}) \\ c_0(t) &= \frac{P_0}{k_{12}-k_{20}}.(k_{20}.e^{-k_{12}.t} - k_{12}.e^{-k_{20}.t}) + P_{tot} \end{aligned} \tag{2.14}$$

Assuming a sample thickness of 1 cm, absorption of this sample when unexcited (all the P_{tot} molecules are in S_0) would be Eq. 2.15:

$$A_0(\lambda) = P_{tot}.\epsilon_0(\lambda) \tag{2.15}$$

And (still assuming a sample thickness of 1 cm) absorption at any time t≥ 0 of this sample would be Eq. 2.16:

$$A(\lambda, t) = c_1(t).\epsilon_1(\lambda) + c_2(t).\epsilon_2(\lambda) + c_0(t).\epsilon_0(\lambda) \tag{2.16}$$

As we consider the differential absorption at a given wavelength λ and time t, it becomes Eq. 2.17:

$$\begin{aligned} \Delta A(\lambda, t) &= A(\lambda, t) - A_0(\lambda) \\ &= c_1(t).\epsilon_1(\lambda) + c_2(t).\epsilon_2(\lambda) + (c_0(t) - P_{tot}).\epsilon_0(\lambda) \\ &= c_1(t).(\epsilon_1(\lambda) - \epsilon_0(\lambda)) + c_2(t).(\epsilon_2(\lambda) - \epsilon_0(\lambda)) \\ &= P_0.e^{-k_{12}.t}.\epsilon_1(\lambda) + \frac{P_0.k_{12}}{k_{12}-k_{20}}.(e^{-k_{20}.t} - e^{-k_{12}.t}).\epsilon_2(\lambda) \\ &\qquad + \frac{P_0}{k_{12}-k_{20}}.(k_{20}e^{-k_{12}.t} - k_{12}e^{-k_{20}.t}).\epsilon_0(\lambda) \end{aligned} \tag{2.17}$$

Which can be re-written with the exponentials as common factors:

$$\begin{aligned} \Delta A(\lambda, t) = &\left(P_0.\epsilon_1 - \frac{P_0.k_{12}}{k_{12}-k_{20}}.\epsilon_2 + \frac{P_0.k_{20}}{k_{12}-k_{20}}.\epsilon_0\right).e^{-k_{12}.t} \\ &+ \left(\frac{P_0.k_{12}}{k_{12}-k_{20}}.\epsilon_2 - \frac{P_0.k_{12}}{k_{12}-k_{20}}.\epsilon_0\right).e^{-k_{20}.t} \end{aligned} \tag{2.18}$$

That in turn can be written as a sum of exponentials, Eq. 2.19:

$$\Delta A(\lambda, t) = \sum_i^n A_i . e^{-k_i . t} \tag{2.19}$$

Where A_i are constants. This model can be further developed, to account for more states S_n, which can be shown to result in an equation similar to Eq. 2.19, with a sum over a larger number of time constants k_i.

Taking into account the fact that we have a limited instrument response function (that we assume to be a gaussian with a width σ), using time constants (τ_i) instead of rate constants (k_i, with k_i=$1/\tau_i$), and adding a potential delay t_0 to account for small errors in the correction of the GVD, we obtain Eq. 2.20:

$$A(\lambda, t) = \sum_i A_i . e^{-\frac{(t-t_0)}{\tau_i}} \otimes \frac{1}{\sigma\sqrt{2\pi}} e^{-\frac{t^2}{\sigma^2}} \tag{2.20}$$

With a numerical computation software (in our case, Scilab), we can run a fitting function using this equation to fit our kinetic traces (the curve $A(\lambda, t)$ at a selected wavelength). As we are not supposed to know a priori the exact reaction scheme, we run the fitting function with an increasing number of exponential until we get a correct fit, as shown on Fig. 2.8. This mean finding the parameters (time constants τ_i, amplitudes A_i, zero time t_0 and standard deviation σ) to reduce the difference between experimental curve (ΔA_{exp}) and the previous (Eq. 2.19) function using those parameters, defined as the χ^2 value, shown in Eq. 2.21:

$$\chi^2 = \int \left| \Delta A_{exp}(\lambda, t) - A_{fit}(\lambda, t)|_{A_i, \tau_i, t_0, \sigma} \right|^2 dt \tag{2.21}$$

Ideally the difference between those 2 curves (called residual, and shown in blue on Fig. 2.8) should only be the sum of the different noises affecting our measurement, as such the residuals should not hold any structure and look like random noise.

2.4.5 Singular Value Decomposition and global fitting

Yet all wavelengths do not hold signal from all molecular states (if $\epsilon_i(\lambda) = 0$), and a single fit is not enough to reveal the whole dynamics.

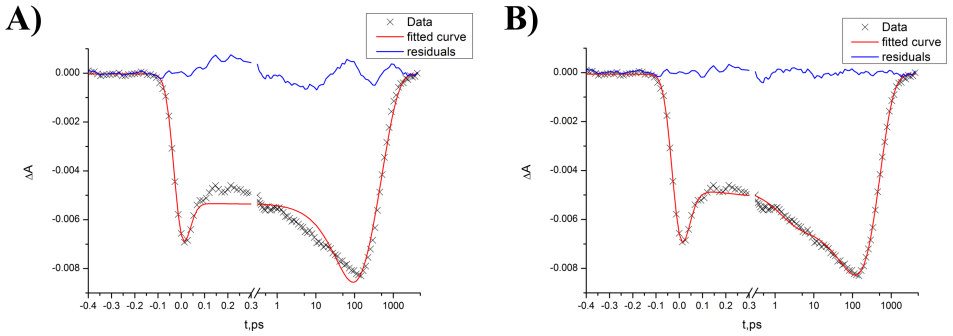

Figure 2.8: A kinetic trace from a pump-probe experiment (black crosses in both figure) and its fit (red lines) using equation 2.19 with 3 or 4 time constants (respectively part A and B). If a first inspection of the data would suggest to use only three time constants (fast decay in less than 100fs, rise again in about 100ps, and the decay in about 1ns), the residuals obtained with 3 time constants show that more are needed, those obtained with 4 are a random noise around 0, which indicates that we cannot significantly improve the fit.

In order to get all the time constants, a global fit is done, meaning that all the kinetic traces are fitted at once, using the same time constants for all of them (with independent amplitudes). While this is possible, this would take quite an extensive amount of calculations, and can be made much easier through the use of Singular Value Decomposition (SVD) filtering on the data, which has the double advantage to allow to do this global fitting by fitting only a few transient traces, and to filter out a lot of noise.

SVD is a mathematical operation on a matrix $m * n$ matrix $M_{m,n}$ that decompose it in 3 separate matrices $U_{m,m}$,$S_{m,n}$ and $V_{n,n}$ as in Eq. 2.22:

$$M_{m,n} = U_{m,m} S_{m,n} V_{n,n} \tag{2.22}$$

Where U (resp. V) contains m "left-singular vectors" as columns (resp. n "right-singular vectors" as lines), and S is a diagonal matrix consisting of the singular values. Those matrices are created so that the diagonal values of S are in decreasing weight order. In our case the $M_{m,n}$ matrix consist in our differential absorption data (or time resolved fluorescence): each column is a kinetic trace and each line contain a (differential) spectrum. The matrix U then contains transients as columns, and the matrix V spectra. The weight sorting of the singular values implies that the most important "behavior" in the data

is reflected by the first transient of U and the first spectrum of V, the second of each having less importance, and so on. The consequence of that is that reconstructing our data with a given number n of singular values will reproduce the original data with more and more accuracy as n is getting larger.

This data reconstruction from a n number of singular values allows to get rid of a lot of noise: indeed the "meaningful" data (related to our signal and not noise) is correlated in both dimensions (time and wavelengths), which implies that its weight in the decomposition will be much larger than the one of the noise. Practically, we can check in a residual matrix (difference between original data and reconstructed data with n singular values, or reconstructed data from all the "non-used singular values") that no signal is left. The interest here is to keep as few singular values as possible, while not forfeiting any data, and doing so we both remove as much noise as possible, and reduce our data to n transients and spectra.

Usually the number of singular values to keep is really low (1 or 2 for time resolved fluorescence, up to 4 or 5 for pump-probe). As those few kinetics and spectra are enough to reproduce our data, fitting those few transients is equivalent to fit all the kinetics we had before, making the problem much easier.

2.4.6 Decay Associated Difference Spectra

Another useful feature for analysis is the Decay Associated Difference Spectra (DADS). Each DADS is associated to a time constant and corresponds to the spectral evolution happening within this time constant. The $DADS_i$ associated with the τ_i time constant can be obtained through global fitting either on the "raw" data (in which case it is simply the spectrum obtained by plotting all the amplitudes A_i with respect to λ) or on the SVD reduced data (in which case the DADS are the product of the fitted amplitudes, the n singular values and the n first V matrix spectra).

Those DADS are helpful to identify the steps of the molecular dynamics, as each of them is related to one time constant, describing one DADS allows to identify the species involved in the reaction before and after the associated time constant. As they correspond to decreasing exponentials, a positive value for $\mathrm{DADS}_i(\lambda)$ imply that $\Delta\mathrm{A}(\lambda)$ is decreasing (either a positive signal disappearing or a negative signal appearing), and vice versa for negative values. Fig.2.9 shows an exam-

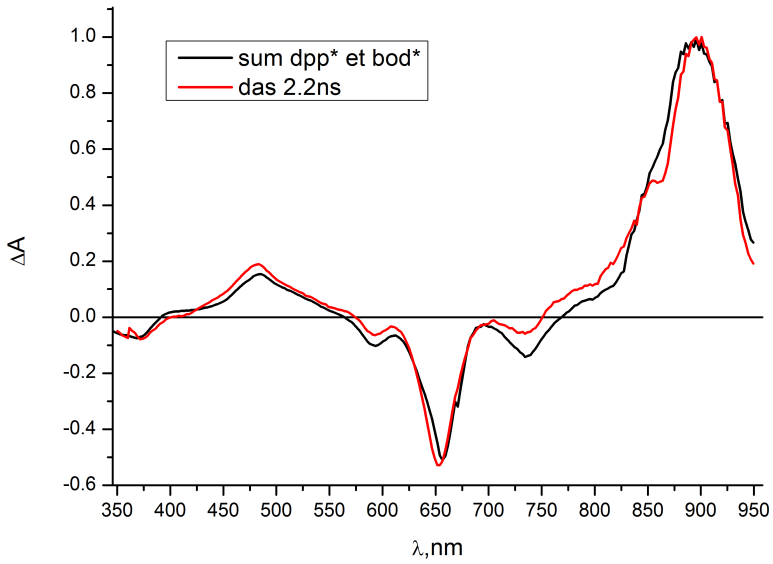

Figure 2.9: Example of a Decay Associated Difference Spectra (red line), and its comparison with the sum of 2 differential spectra obtained in other experiments (and the signature of the ground state, which is null). Those 2 other spectra correspond to the excited state of 2 molecules (dpp and bod, molecules described in chapter 3.1). This DADS indicates that before this 2.2 ns time, the molecules are in state implying both dpp and bod in their excited state, and that this population is decaying back to the ground state.

ple of a DADS obtained for the "cascade molecule" (described later in chapter 3.1), associated to a 2.2 ns time constant: this DADS overlaps well with a reconstructed spectra (black line), made by the sum of 2 differential spectra associated to excited species. This implies that what we are observing at times around 2.2 ns is the decay of those excited species.

2.4.7 Global target analysis

A last tool used in some of the data analysis is the software GloTarAn (source: glotaran.org), used to do Global Target Analysis. The software allows to chose a model to fit our data, meaning that we can set sequential or parallel processes, with chosen branching rates and time constants as starting parameters. The program then tries to fit the

data with the set model, adjusting the parameters to reduce the χ^2. The interesting part of this program is that the output are not only the residuals (who allow to determine whether the data was fitted), but also the DADS and SADS (Species Associated Differential Spectra, more on them later) associated with each state and the transition it undergoes. Indeed, many different models could fit the data with similarly good residuals, and the analysis of these DADS and SADS, based on a priori knowledge gained from independent experiments, is a very good way to determine whether the assumed model is correct or not.

Assuming a given reaction model, it is indeed possible to decompose the data into the sum of the contributions of implied species (in simple sequential cases, as in Eq.2.17, or more complex equations if we assume parallel reaction paths). Each species is then associated to a contribution called Species Associated Differential Spectrum (SADS, which should for a species i be similar to ϵ_i), and each time constant to a DADS. Analysis of these DADS and SADS then requires to know the expected shapes and spectral features of the supposed species: as we built the model, we know that we expect a given molecular state at a given step of the reaction (by example an excited donor as the first step), and as such the SADS should be relevant (in this example, it should present the bleach and SE of the donor - which we can acquire with absorption and fluorescence experiments - and a positive ESA). If any of the resulting SADS and DADS presents an abnormal feature, we can define the model as wrong.

To illustrate that, we create an artificial data set, as shown in Fig. 2.10. We will assume a reaction involving 3 states (the ground state and 2 different excited states), with the mock absorption spectra given in the top left of Fig. 2.10. To prove that we can identify precise dynamics, we define the reaction shown in the top right quarter: the population of S0 is excited in the state 1, in two groups (which can be caused by different conformations), with 67.5% of the molecules going in the excited state 1 to immediately relax in S0, with a 6.66 ps time constant, and the remaining 32.5% going through state 1 to a state 2 with a 7.14 ps time constant, and then relaxing in 500 ps. Corresponding kinetics are shown in the bottom left (induced differential concentrations) : the state S0 is depopulated from the beginning as S1 is populated, and then is partially repopulated through the first relaxation process. The second process transfers the population from state 1 to state 2, before going back to S0. The last quadrant shows

a 2D map of the corresponding mock data, on which some white noise was added.

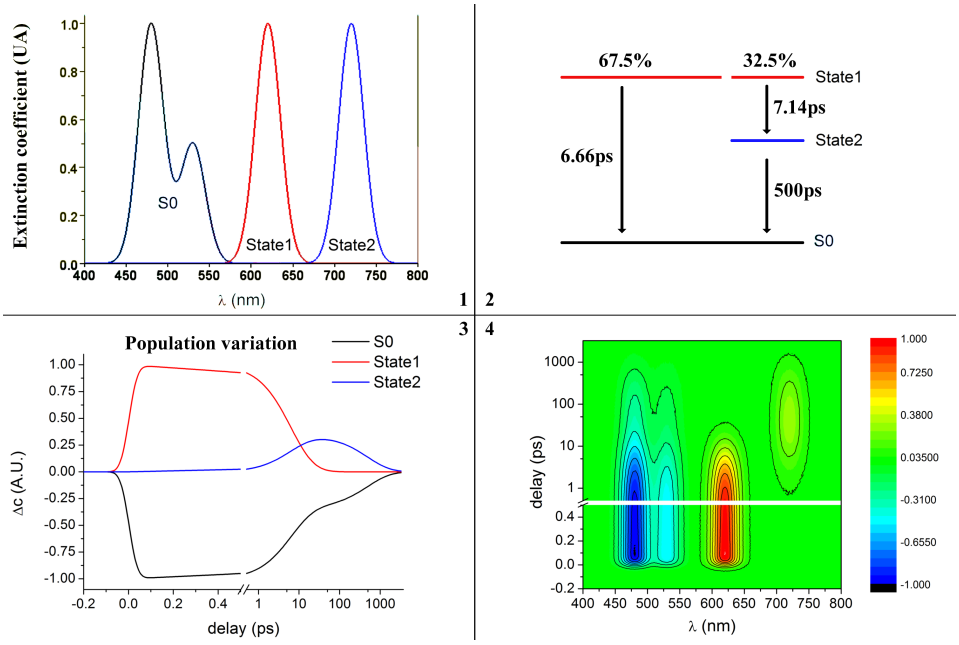

Figure 2.10: Test dataset creation, in order to test the global target analysis. Assuming the reaction scheme from 2), one can calculate the population variations in the 3 implied states as shown in 3). Assuming the spectra from 1), we can create a dataset, shown in 4) after the addition of some white noise

Now that we have a dataset corresponding to a known reaction, we can check how the global target analysis behaves when one uses different models. The results are shown in Fig. 2.11, in 3 columns each corresponding to a different model, represented in the first line. The first column correspond to a fit with correct parameters (the ratio set for the 2 populations in state 1 is fixed at the correct value, and the time constants initial values are approximate for the fitting procedure). Second column corresponds to the simplest sequential model. The third column makes also use of the correct model, but with a ratio in the state 1 populations fixed at 60% and 40%. The kinetics representing the population in the different states are shown in the 3rd line, with linear time axis until 400 fs, and logarithmic scale at longer times.

The second line of Fig. 2.11 shows the 2 first transients of the residuals after the fitting procedure: in each case, those transients are a white noise, which means that all of the meaningful signal has been

fitted. If these residuals are an indication for the quality of the fit (a sum of 2 exponentials in the case of the sequential model resulted in residuals that still contained some pertaining data, indicating the need for a third one), it is clear that it is not enough to determine which model is the correct one.

So, in order to determine the best model, more informations are needed, shown here on the 4th line (the SADS) and 5th line (DADS, vertically shifted for the first and third models). Here, if the model is correct, then the SADS should correspond to the spectra of the 3 states as defined in Fig. 2.10 (with the exception of S0 signature, that should be negative as it is bleached). While the first and third models result in good SADS (state 1 has the bleach of S0 and the absorption band at 620 nm, state 2 has the bleach of S0 and the absorption band at 720 nm), it is not the case of the second model: the SADS associated to the state2 has peaks both at 620 nm and 720 nm, which should not be.

As well, looking at the DADS allows to rule out the third model: the second DADS, associated to 7.14 ps, should in this model correspond to a transfer from State 1 to State 2, and no change in the bleach of S0 is expected. Yet this DADS shows the signature of S0 bleach reduction: this is an aberration.

Of course, such an analysis requires to know a lot about the molecules and the state-associated spectra, and is not so easy in the case of real systems. For example, it is usually hard to obtain an excited species spectrum, but we may determine charged species absorption spectra, or the associated fluorescence spectrum and analyze the stimulated emission instead. But the principles are the same, and the results are quite powerful, as even slight differences in the starting ratios can be determined.

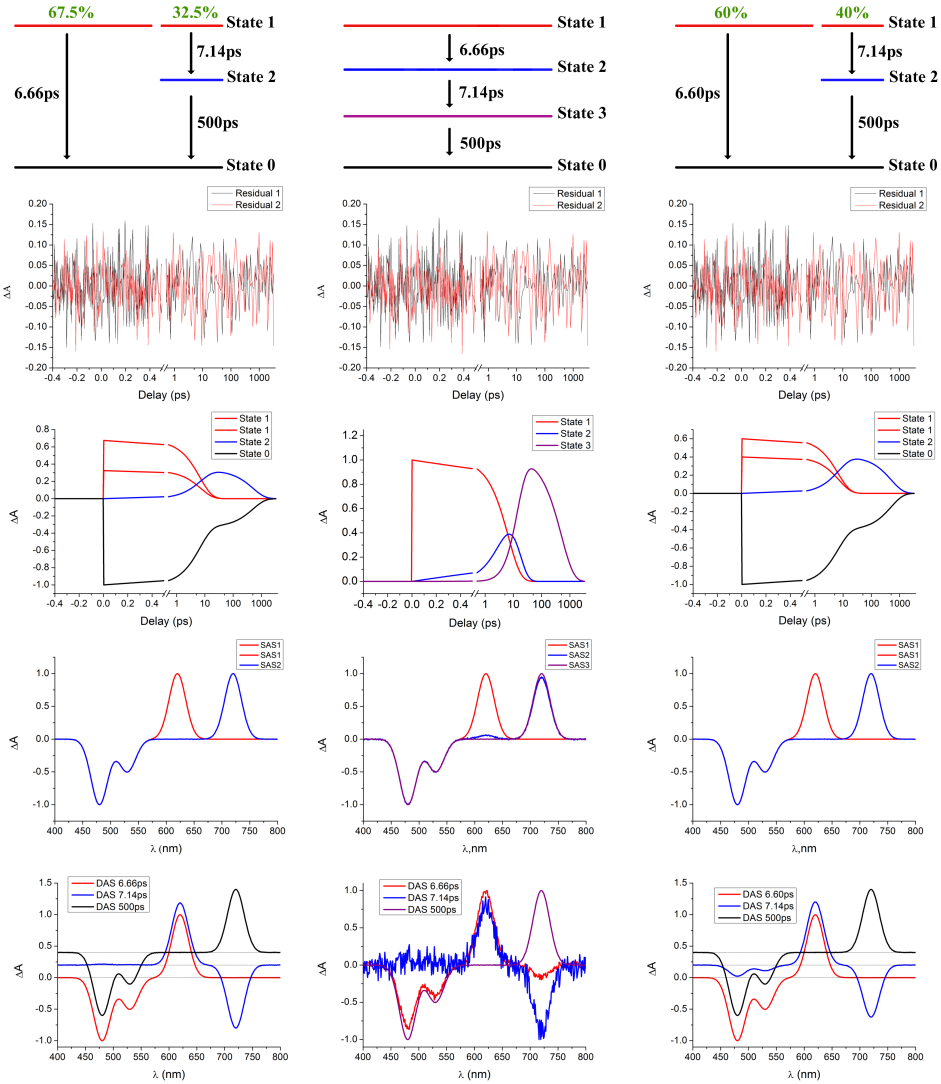

Figure 2.11: Example of 3 different input models for a global target analysis on the dataset shown in Fig. 2.10. Each model is represented in the first line, with its corresponding kinetics shown on the third line. As the second line shows, the residuals of all these fits are equally good, and cannot differentiate the correct model (first column) from the others. Only the analysis of the SADS of state 2 in the case of the second model and of DADS 7.14ps for the third model indicate that those models are false. DADS of the first and last models were vertically shifted for easier reading.

2.5 Spectro-electro-chemistry

2.5.1 Interest for species identification

As said in 2.3.5, the contributions of many species can be mixed in the differential spectra. Obtaining the absorption spectra of the charged species will allow identification of said species. Moreover as we are studying molecules for photovoltaic applications, we are expecting to see this charged state, and confirming the presence of these species (or their absence) in the molecules dynamics if of prime importance. These are the reasons who led to a collaboration with the team led by Sabine Ludwigs, in Stuttgart, where spectro-electro-chemistry experiments were performed.

2.5.2 Principle

The idea behind spectro-electro-chemistry is to record the absorption spectra of oxidized or reduced species[27]. This is achieved by mixing a "classical" absorption spectroscopy setup with a cyclo-voltametric setup. As in cyclo-voltametry, the current flowing between a working electrode and a counter electrode is measured as a function of the applied potential between the working electrode and a reference electrode.The particularity of this setup is that, in order to have a homogeneously charged sample to probe, the working electrode is a flat round surface surrounded by a circular counter electrode, held at a controlled distance from the bottom of the recipient. With an optical fiber, light coming from a broad spectrum lamp is sent through the bottom of the sample, reflected by the working electrode, and again collected by the fiber, so that it can be sent to a spectrometer, as shown on Fig.2.12. The thickness of the probed sample is controlled by a micrometric screw, and the sample can be kept under nitrogen atmosphere to avoid unwanted oxidation. As a result of this experience, we obtain spectra each associated with a point on the cyclovoltametric curves. On those spectra, we can see the absorption of the neutral state disappear while the sample is oxidized or reduced, as the absorption of the cation or anion rise. If the potential is high enough, one can also get the absorption spectra of the di-cation/anion.

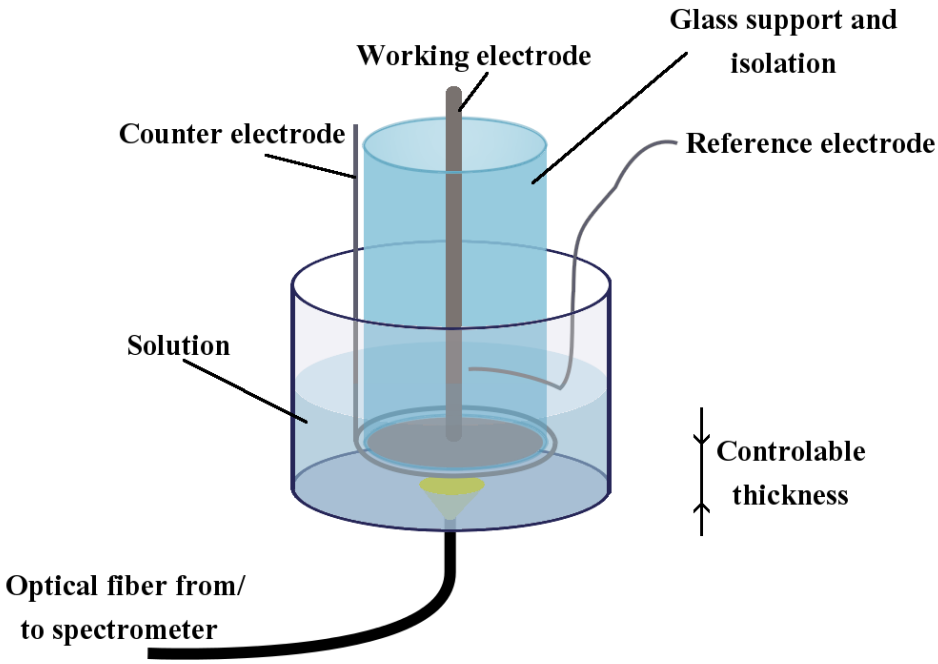

Figure 2.12: Simplified schematic of a spectro-electro-chemistry setup. The sample to be studied is solvated with a spectrally neutral salt and placed in a cuve. A chosen potential is applied between the working and reference electrodes, while the resulting current is measured between the working and counter electrodes. In order to get in-situ spectra, an optical fiber coming from a lamp (and going back to a spectrometer) brings light, that is reflected on the working electrode used as a mirror.

Part II

Results

3

A light harvesting molecular triad

3.1 Antenna principle

3.1.1 Introduction

Within the recent developments of organic materials for photovoltaic applications, a huge variety of molecules and methods where developed, some of which leading to devices reaching the 10% efficiency[28,29]. Among these, the blend P3HT/PCBM (acronyms standing for *poly(3-hexylthiophene)* and *[6,6]-phenyl-C_{61}-butyric acid methyl ester* respectively) is still considered as a reference system[30]. Many solutions are considered in order to improve the efficiency of these P3HT/PCBM devices, among which better control of the structuration[31–33] (an idea developed in chapter 4.2) or combination of several layers with complementary absorptions[34]. Yet, another path is to use different materials with better overall characteristics[35]: if the donor P3HT conductivity

and charge transfer properties are well recognized, they are limited by an absorption spectrum that -depending of the deposition methods and treatments- does not absorb at wavelengths above 550 to 600 nm. As a consequence, it is interesting to develop a new efficient donor dye with a broader spectrum to the IR side able to transfer charges to an acceptor (usually based on fullerenes)[36,37].

The BODIPY dyes (boron-dipyrromethene) are a widely studied class of molecules, that proved efficient at charge generation in various systems[38–44]. In other applications BODIPY is appreciated for its high fluorescence quantum yield, stability, and chemical versatility. Here, the BODIPY (latter abbreviated as BOD) dye developed and synthesized by E. Heyer and R. Ziessel was substituted with styryl groups in positions 3 and 6, in order to bathochromically shift its absorption and emission spectra, while polyethylene groups were attached to the boron center and the styryl groups to increase the solubility. This results in a Bodipy dye with an absorption between 550 nm and 670 nm (Fig. 3.3 red spectrum).

In order to strengthen the antenna effect of this donor group two other groups were added, whose efficiency for charge generation is proven: a thiophene type diketopyrrolopyrrole (DPP[45–52]) and a triphenylamine (TPA[53–56]), resulting in a triad of 3 moieties of decreasing electro-negativity (relevant oxidation peaks of TPA, DPP and BOD are respectively 1 V, 0.9 V and 0.6 V). The complete triad TPA-DPP-BOD and the separated components are sketched in Fig. 3.1. The three components have complementary absorption spectra (Fig. 3.3), the intended effect is that no matter where in the molecule a photon is absorbed, the resulting excitation localizes on the BOD, where an electron can be transferred to an acceptor, like PCBM. We will verify whether or not it is happening via ultra-fast spectroscopy, while pumping in the UV (at 320 nm), and if possible find hints for improvements.

First observations can be made on the absorption spectra of the molecules. In the following, all experiments are done on molecules in solution in THF (tetrahydrofurane), except for the electro-chemistry experiments in which case DCM (dichloromethane) with NBu_4PF_6 as supporting electrolyte was used. As one can see in Fig. 3.2, the choice of DPP as the central moieties of our triad was made because in the un-substituted form its absorption band (in black, 440-570 nm) is a perfect fit to complement the absorption of BOD. Yet, we discovered later that in the triad (Fig. 3.3 black spectrum), no such absorption was observed. After analysis of the absorption of DPP alone (with

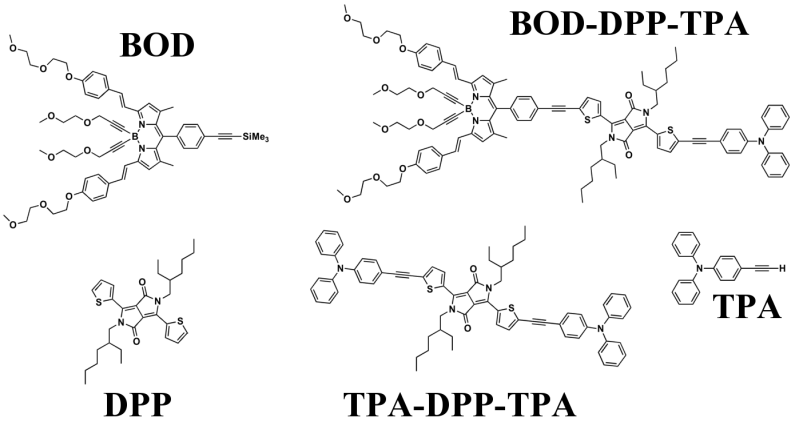

Figure 3.1: Chemical structure of the studied molecules: the triad BOD-DPP-TPA, and the 3 separated components, with DPP being substituted by 2 TPA groups or un-substituted, as its spectrographic properties vary upon substitution.

bromine instead of TPA) and substituted with one or two TPA group (whose absorption band is centered at 324nm and negligible above 400 nm), we observed that its main absorption band red shifts from 547 nm when un-substituted to 582 nm and 624 nm when substituted one or two times (resp.). As a consequence, in the following we will use the TPA-DPP-TPA (shortened in DPP) molecule as our reference to identify the contribution of DPP in the triad.

If this spectral shift is not too big of a problem for the absorption of the molecule (the absorption spectrum of the triad is not filled, but it is still enhanced by DPP), this will prove problematic for the pump-probe spectroscopy, where the signatures of DPP and BOD bleach will overlap. Even worse, their fluorescence spectra are also very similar, as seen in Fig. 3.8 (dotted spectra): identification of the species in the differential spectra will be complicated.

Another observation on the static absorption spectra (Fig. 3.3) is that the sum (Triad$_{sim}$, in green) of those of BOD (blue line), DPP (through the spectrum of TPA-DPP-TPA minus two times the spectrum of TPA, pink line) and TPA (red line), reproduce rather well the triad's one, at least at wavelengths longer than 500nm. This indicates that we can use the absorption of TPA-DPP-TPA as a reference for the absorption of DPP lowest absorption band (500 - 650 nm). The additivity of the spectra is not as good in the near-UV, thus question-

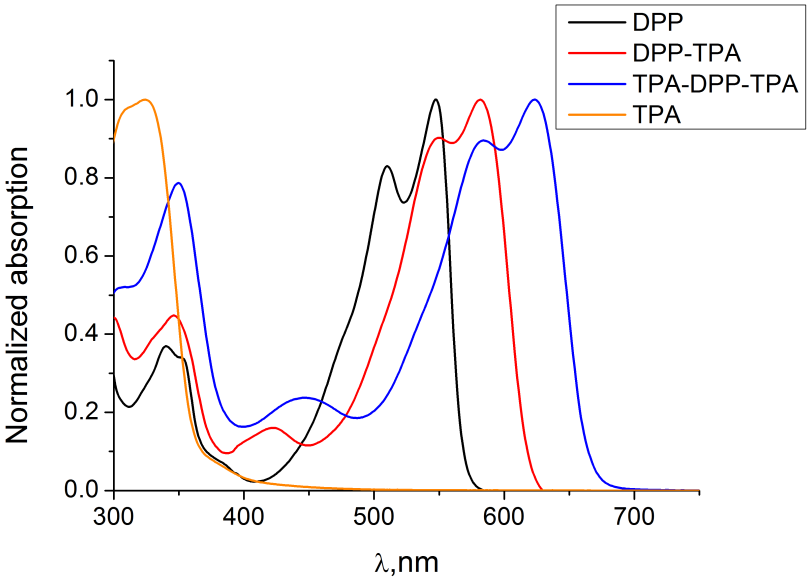

Figure 3.2: Absorption spectra of DPP, TPA, TPA-DPP and TPA-DPP-TPA in THF: upon substitution of DPP, its absorption band shifts from 547 nm to 582 nm and 624 nm.

ing our approach to obtain the single DPP near-UV spectrum from that of TPA-DPP-TPA. We assume in the following that at 320 nm a mixture of all three molecular components is excited.

In order to understand the time-resolved spectroscopy of the triad, we will need to carefully analyze the relevant Decay Associated Differential Spectra (DADS), with the support of information from other experiments (absorption spectroscopy, fluorescence spectroscopy, time-resolved fluorescence spectroscopy and electro-chemical spectroscopy) made on the three reference molecules (TPA, TPA-DPP-TPA and TPA-BOD). If the analysis will still be complex, we will be able to determine which species are implied at each step of the triad photo-reaction, by reproducing the DADS with linear combinations of these species' spectra.

3.1.2 Results

3.1.2.1 Experiments on isolated components

Faced to the result of the pump-probe, as shown on Fig. 3.4, the problem of the species identification arise: if the BOD ground state

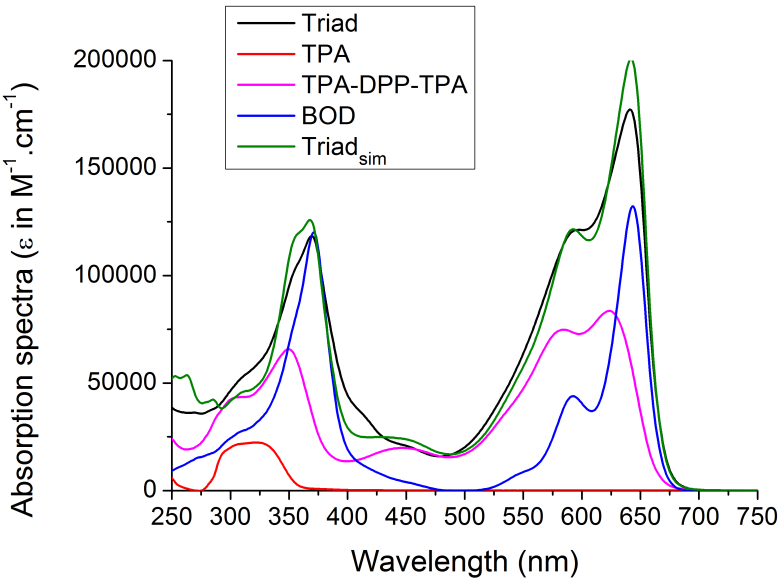

Figure 3.3: Extinction coefficient of the triad, TPA, TPA-DPP-TPA, BOD alone, and the simulated triad (with Triad$_{sim}$=TPA+TPA-DPP-TPA+BOD-2∗TPA , in THF. BOD's absorption is well defined by 2 peaks at 644 and 593 nm for its S_1 band and 371nm for its S_2 band. DPP absorption (in TPA-DPP-TPA) is characterized in its S_1 band by 2 nearby peaks at 623 nm and 585 nm. TPA's spectrum consists in an absorption band centered at 324 nm. As shown by the sum of the 3 individuals spectra, the triad is basically the sum of those contributions in the red (>500 nm) part of the spectrum. The UV side of the spectrum is more questionable, and we assume that at 320nm (excitation wavelength, vertical line), all three moieties absorb.

bleaching (GSB) is easy to identify, through the two negative peaks at 593 and 645nm, the only other certain observation is that we observe a stimulated emission (SE) from BOD* or DPP* (or both), as a trough at 720 nm.

In order to get enough information to identify the species, we also did pump-probe experiments on TPA-DPP-TPA and TPA-BOD, which allowed us to obtain a good identification of the differential spectra for their excited states. Fig.3.5 shows some relevant ΔA spectra for DPP, showing the 2 temporally distinct spectral shapes observed. The first (black curve, 320 fs) may be attributed mostly to a vibrationally excited S_1 state of the DPP, as we recognize it's GSB. Yet we excite at 320 nm where DPP does not absorb, indicating that an extremely fast energy transfer from TPA* to DPP took place, which is possible

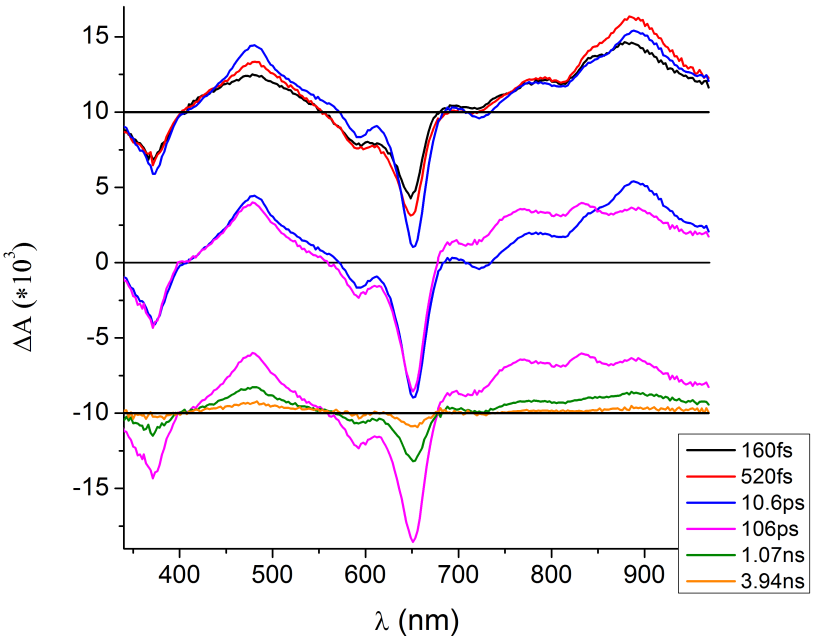

Figure 3.4: Selected differential absorption spectra obtained for the triad in THF after excitation at 320 nm. At the shorter times, we have a strong contribution of both DPP* (with the ESA band around 890 nm) and BOD* (with its ESA at 483 nm). The former ESA decays in ps (red to blue spectra), indicating a decrease of the population of DPP* (top curves, shifted by +0.01). A new absorption rises between 700 and 850 nm within 100 ps, as a new species is formed (middle curves, blue to pink), that disappears in the following ns.(bottom curves, shifted by -0.01)

as the TPA's fluorescence maximum is at 388 nm and ranges up to 500nm (see Fig. 3.8 inset), in resonance with DPP's higher absorption bands. After some ps, the molecule relaxes to its S_1 state, and presents a stronger stimulated emission (shifting the maximum of the negative signal from 633 nm to 654 nm, and revealing a peak at 730 nm), as well as an increased ESA with a strong absorption around 890 nm. This second state lives several ns, as the ΔA spectra at longer times indicate. In the following, we use the average over many ΔA spectra at times >25 ps as our reference for DPP*, using the fact that this ΔA(t>25 ps) spectrum is proportional to $\epsilon(DPP^*)$. As well, we can define a mean of ΔA(t<<25 ps) spectra as proportional to $\epsilon(\mathrm{DPP}_{S_n})$.

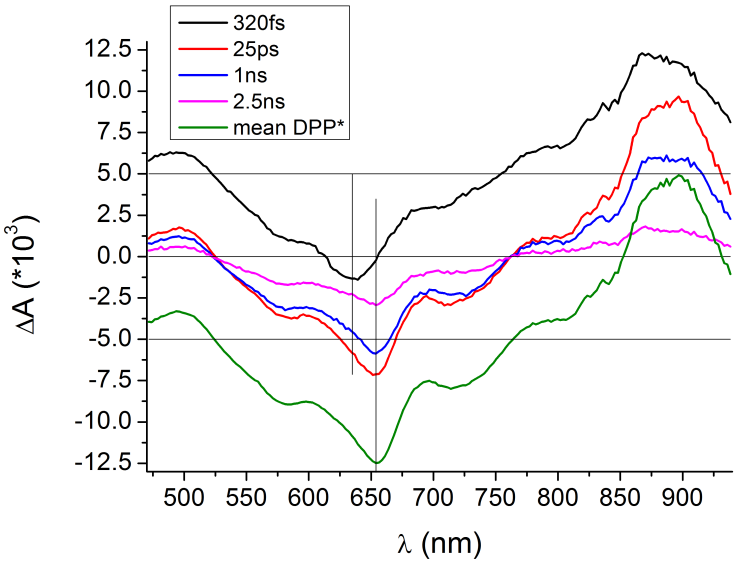

Figure 3.5: Selected differential absorption spectra obtained for TPA-DPP-TPA in THF after excitation at 320 nm. Two characteristic spectra are observed: a first one at short times (black curve), with a minimum at 632 nm, corresponding mostly to the DPP bleach and a weak and sightly blue shifted SE, and a second quasi-stationary spectrum with an increased stimulated emission, shifting the minimum to 654 nm. (the two vertical bars are visual helps to highlight this effect), and an intense ESA band at 890 nm. This second spectrum decays in nanoseconds, and is attributed to the relaxed DPP S_1 state, whose average spectrum is shown in green. The first (320 fs) and last (average) ΔA spectra are shifted (respectively by +5 and -5×10^{-3}) for clarity.

The same was done with BOD, the results being summed up in the Fig.3.6, with a reaction scheme similar to that of DPP (apart from the initial FRET): after excitation in a S_n state, the molecule relaxes in a few tens of picoseconds in its S_1 state. The average spectra over delays longer than 30 ps is used as our reference spectrum for excited BOD*, proportional to $\epsilon(BOD^*)$. Just as with DPP, we can define a mean of ΔA(t<<30 ps) spectra as proportional to $\epsilon(\mathrm{BOD}_{S_n})$.

Thanks to those two spectra, we can better identify the contributions in the triad, and identify when the dynamics is dominated by the excited species DPP* and BOD*. Yet, this is still not enough to completely understand the data from the triad, as we miss some additional induced absorption (absorption bands in the 700-850 nm range, visible on the 106ps ΔA spectrum, that are not identified), as well as a clear

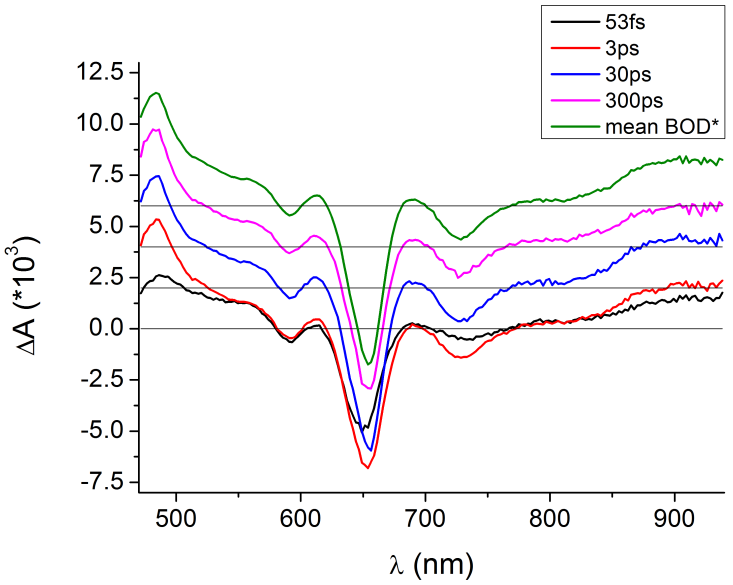

Figure 3.6: Selected differential absorption spectra obtained for BOD in THF after excitation at 320 nm. As for DPP, BOD is excited in its S_n state and relaxes into S_1 in less than 1 ps, where it then lives for several ns. Differential spectra from this state are averaged yielding the green curve. The ΔA spectra for 30 ps, 300 ps and the average spectra are all shifted by +2 in order to highlight the lack of changes past the first few ps.

view of the dynamics of these excited species population.

Concerning the missing absorption, the antenna itself may behave as a donor-acceptor molecule (the TPA being a good electron donor), and as such the formation of charge transfer (CT) states is possible, and can explain these additional absorption. To correctly prove (or infirm) this, we recorded the absorption spectra of the different species charged states. The main results are shown in Fig. 3.7. TPA cation (black curve) is a broad peak centered at 730 nm, BOD anion (red curve) shows a main peak centered at 595 nm and a smaller peak at 455 nm, DPP anion peak is centered at 753 nm. As those spectra were obtained during a cyclovoltametric cycle, we can use in each case the difference between the absorption spectrum of the charged state (radical anion or cation) and that of the neutral specie: doing so results in differential spectra ΔA that correspond to the extinction coefficient of the charged specie (for example for DPP, it will account for both the bleach of DPP and the absorption of DPP^-). We use these to determine $\epsilon(TPA^+)$, $\epsilon(BOD^-)$ and $\epsilon(DPP^-)$.

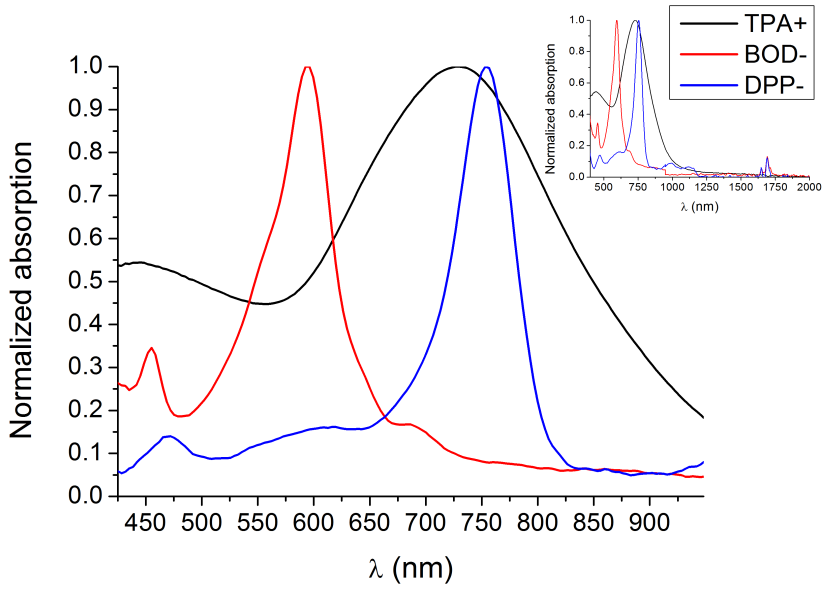

Figure 3.7: Normalized absorption spectra of the expected charged species, in DCM with NBu_4PF_6 as supporting electrolyte: TPA cation (black), BOD anion (red, obtained on BOD-TPA) and DPP anion (blue, obtained with TPA-DPP-TPA). Inset: Extended spectra, up to 2 μm.

Finally, we also recorded the time-resolved fluorescence of our three molecules (DPP, BOD and triad) using the streak camera with 10 ps resolution, which gave us access to a more precise information about the excited species lifetimes, as they can be obtained directly from these experiments (in opposite to the pump-probe, where the SE signal can be hidden or modified by an overlapping ESA). The main results from these experiments are summed up in Fig. 3.8 as DAS obtained after global analysis. While in the isolated forms both DPP and BOD exhibit simple decays (represented by a single DAS, dotted in the figure), associated respectively to a time constant of 2.2 ns and 4.5 ns (not shown), the triad signal require a multi-exponential decay to be fitted.

This is not unexpected since the 320 nm excitation is in resonance with transition for all three molecular components of the triad. Thus the short excitation pulses create a linear combination of the three possible wave-functions, that will break up into 3 different localized excitation: TPA*, DPP*, and BOD*. The fluorescence measured with 10 ps time resolution in the red spectral region (600 - 800 nm) captures only the fluorescence of the latter two. Monitoring the near-UV region,

where TPA is fluorescing, does not show any fluorescence above the noise level for the triad. This indicates that TPA is quenched in a very small fraction of the streak camera IRF, and we estimate the excited state lifetime to be shorter than 200 fs. In the red part of the spectrum, the fluorescence of the triad is fitted with 3 time constants (error bars in brackets) that are 63 ps (1), 518 ps (4) and 2.3 ns (0.02), associated to 3 slightly different DAS.

These different time constants by themselves indicate that several processes occur in the molecule, that quench its fluorescence. Comparing the DAS gives a bit more informations about what happens in the triad, through the differentiation of the shoulders at 723 nm: the first DAS (63 ps) is very similar to the DAS associated to DPP, while the 518 ps DAS is closer to that of BOD, and the last one (2.3 ns) seems to be in between and thus implies both DPP* and BOD*. This means that we have at least 4 different populations: for both DPP and BOD we have two conformations, one that results in an "active" population of the excited state that is quenched (in 63 ps or 518 ps) by new processes occurring in the triad and one that results in an "inactive" population that decays much slower (2.3 ns), with a time constant close to that of isolated moieties. The relative amplitudes associated to these DAS (resp. 30%,45% and 25%) allows us to determine that, assuming the last DAS is a 50/50mix of DPP and BOD, about 70% of the DPP molecules and 78% of the BOD molecules are in the "reactive" state.

To sum up all these preparatory results, we can summarize the main spectral characteristics of the species in the Table 3.1, which will help us identify the involved species in the triad photo-dynamic, alongside the results from the time-resolved spectroscopy that indicate a decay of DPP* in 63 ps, a decay of BOD* in 518 ps, an finally a decay of both DPP* and BOD* in about 2.3 ns.

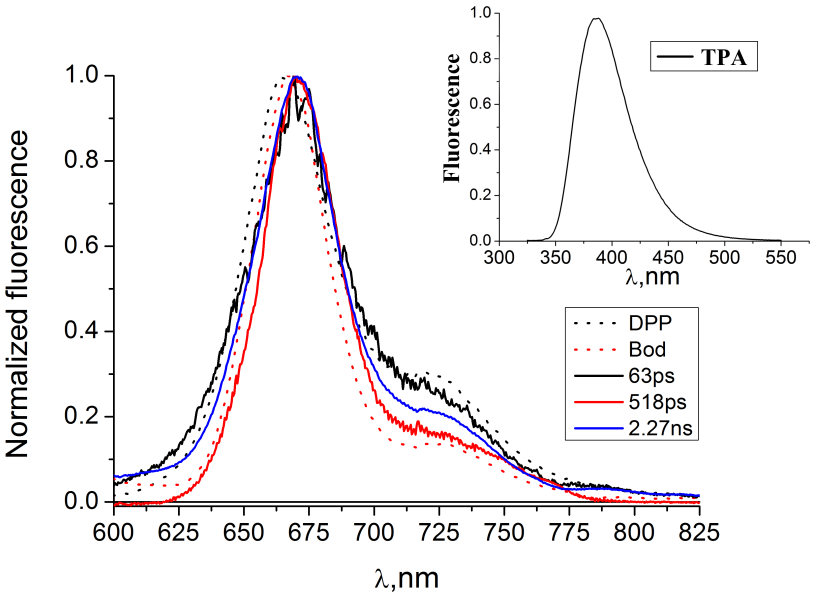

Figure 3.8: Full lines: DAS associated to 63 ps, 518 ps and 2.27 ns obtained by global fitting of the time resolved fluorescence of the triad in THF. Dotted lines: fluorescence spectra obtained for DPP and Bodipy. Comparison of these leads to the identification of the 3 decays: the faster decay is associated with DPP, the intermediate one with Bodipy, and the longer one with a mix of these species. Insert: Fluorescence of TPA

Molecule	State	Characteristic peak(s)
DPP	GSB	349 nm, 582 and 622 nm
	ESA	890 nm
	SE	665 nm and 720 nm
	anion	753 nm (narrow)
BOD	GSB	370 nm, 593 and 645 nm
	ESA	483 nm and >850 nm
	SE	665 nm and 720 nm
	anion	595 nm (narrow)
TPA	cation	732 nm (broad)

Table 3.1: Spectral characteristics of the different participating species. Central wavelengths of the main peaks are given, except for BOD's ESA in the near IR, for which the visible limit of the band is given.

3.1.2.2 Analysis of the antenna pump-probe data

Now that we have the needed information to identify all the species we may encounter in the triad photo-reaction, we can carefully analyze the results from the initial pump-probe experiment. Rather than analyzing the hundredth of differential spectra obtained, we performed a global analysis of the triad's data, fitting it with a sum of 5 exponentials associated to 5 time constants of 290 fs, 6.3 ps, 52 ps, 0.50 ns and 2.2 ns. This leads to five DADS that we can analyze one-by-one indicating at each step which species are involved.

Those DADS were calculated using the data reconstructed after SVD filtering, keeping the 6 first elements. As shown on Fig. 3.9, this mean that we dropped out signals that had less than 1% of the weight of the main signal, much below the level of noise on our data. The inset shows the main spectrum (corresponding to the first singular value, in blue), and the sixth one in green. To better point out how small even this 6^{th} one is, it was magnified 10 times in orange. The fit used 5 constants as shown in Fig. 3.10: using only 4 did not reproduced well our data (mostly at long delay), while using 5 left only white noise, with an amplitude of 1.10^{-3}.

To simplify the description of the reconstructed DADS ($DADS_{rec}(\tau)$) as a sum of different contributions, the implied species that disappear will be given negative contributions, while those that arise will have positive contributions. No quantitative concentrations are given for each contributions because the reference spectra are only proportional to the actual extinction spectra of the molecules. The fits are deemed good when the features of the DADS (position and signs of the peaks) are reproduced. Slight differences result mostly from small changes in the overlap of the pump and probe pulses: as the latter is not spectrally uniform, and even if the pump spot is a bit larger than the probe one, any small change in their overlap changes the amount of excited molecules that a particular part of the probe sees. More problems may arise on short times (<1 ps), as the chirp correction will dramatically impact the differential spectra at these times: since the spectra evolve temporally (not only through vibrational relaxation, but also because of uncertainties on the GVD correction), the global fit assumption is not appropriate at such times. A good example of that phenomena can be seen on the figures 3.15 and 2.9: both are DADS obtained through global fitting of the pump-probe data for the full antenna and correspond to the 2.2 ns time constant. If the analysis of the two datasets leads the same results in terms of time constants (within small error

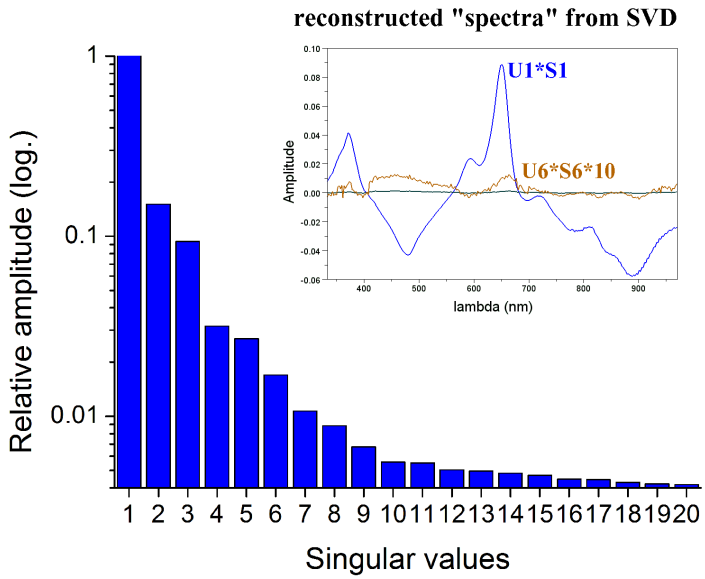

Figure 3.9: Relative values of the 20 first singular values obtained on the triad's pump-probe data, shown in logarithmic scale: the 3rd value is already one tenth of the first one, the seventh is about one percent of it. Inset: reconstructed spectra corresponding to the first value (blue) and the sixth one (green, multiplied by a factor 10 in orange).

bars), it is obvious that their shape is different (the DADS shown in Fig. 2.9 has a much more intense ESA band between 800 and 950 nm). Yet, this is only related to a given configuration of the experimental setup (overlap between pump and probe spots in the sample), as proven by the similarly good fit obtained in each case: if the data used for the analysis of a given experiment comes from the same set of experiments (same experimental conditions), we will obtain the same conclusions for the reaction schemes.

An alternative would have been the global target analysis to generate those DADS (and associated SADS). But as explained in chapter 2.4.7, target analysis needs a tentative reaction scheme as an input parameter. We have seen that TPA and BOD are simultaneously excited, and the streak camera data indicate that the populations of BOD and DPP are spread in reactive and non-reactive populations. Therefore, we would have to treat at minimum five different species with unknown relative concentrations, creating a much too large set of reaction schemes to be tested by target analysis.

The first DADS is represented (in black) along its fit (red spectrum)

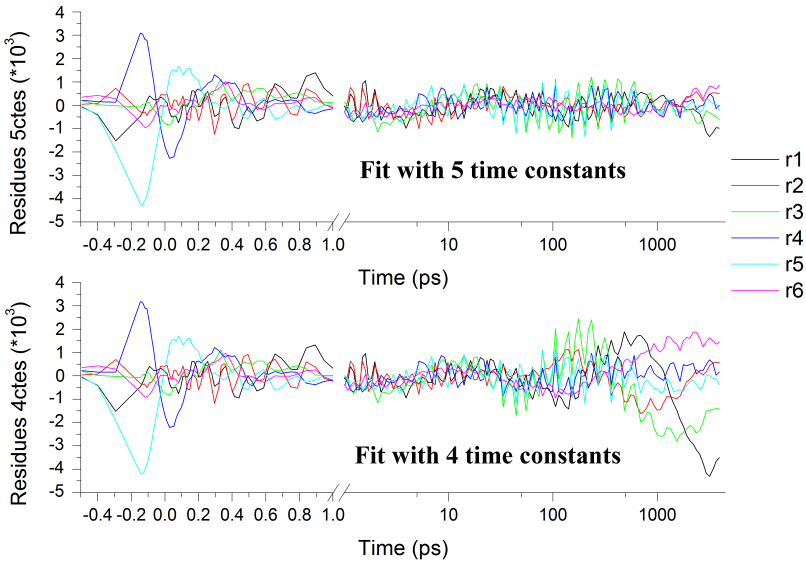

Figure 3.10: Residues of the 6 principal components resulting from the SVD of the triad's pump-probe data, with 4 or 5 time constants (difference between the transients and the fits). Using only 4 time constants leads in a fit that doesn't reproduce well the data at long times and residues that are not similar to blank noise, here particularly visible at times longer than 100 ps.

in the Fig. 3.11. The reconstructed spectra is the best fit found, and is the sum of the spectra corresponding to the transitions from S_n to S_1 of DPP and BOD (differences $\epsilon(DPP^*)$-$\epsilon(\mathrm{DPP}_{S_n})$ and $\epsilon(BOD^*)$-$\epsilon(\mathrm{BOD}_{S_n})$, plus an additional formation of DPP*:

$$DADS_{rec}(291fs) \propto (a_1 + a_3) * \epsilon(DPP^*) + a_2 * \epsilon(BOD^*) - a_1 * \epsilon(DPP_{S_n}) - a_2 * \epsilon(BOD_{S_n}) \quad (3.1)$$

This indicates that as in the separated molecules the very first step of the reaction is a relaxation from the S_n states to S_1 of BOD and DPP, and another reaction that populates DPP* (associated to a_3) notably contributing to the rising ESA at wavelength above 800 nm. The most probable explanation is that the energy transfer from TPA* to DPP* is not temporally distinguished from the relaxation of BOD and DPP, all these ultrafast phenomena being fitted with only one time constant.

The second time constant of 6.3ps is associated with the DADS

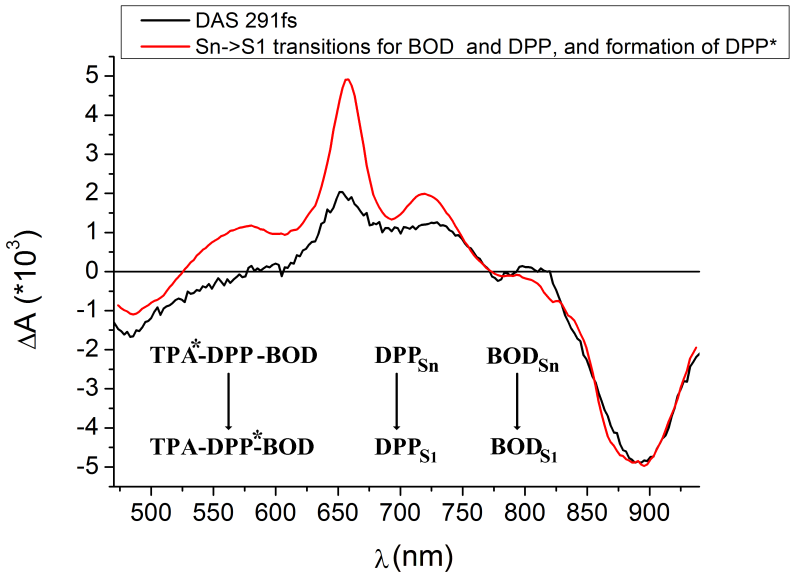

Figure 3.11: Black spectrum: DADS associated to the 291 fs time constant obtained through global analysis of the triad's pump-probe data. Its features are reproduced by the red spectrum, calculated as the relaxation of DPP and BOD from S_n to $S1$ (spectra obtained from the pump probe experiments on these molecules), and the formation of DPP* (FRET from TPA*)

shown in black on Fig. 3.12, which is very well reproduced by the difference between the spectra of DPP* and BOD*, shown in red:

$$DADS_{rec}(6.3ps) \propto b_1 * \epsilon(BOD^*) - b_2 * \epsilon(DPP^*) \qquad (3.2)$$

This indicates that an energy transfer from DPP* to BOD* occurs within 6.3ps. The amplitudes b_1 and b_2 associated to the extinction coefficients are in theory equal, but the actual values used for the calculation are different, as we used differential spectra that are only proportional to extinction coefficients, and dependent of the number of excited molecules in the experiments. Such an energy transfer is possible, as their is an overlap (even if relatively small) between DPP's emission and BOD's absorption.

Fig. 3.13 shows the third DADS, associated to the 52 ps time constant. Fitting this DADS was done thanks to the indication of the time resolved fluorescence: we know that we must include a decrease of the DPP's SE, which corresponds to a decrease of DPP*. Beside

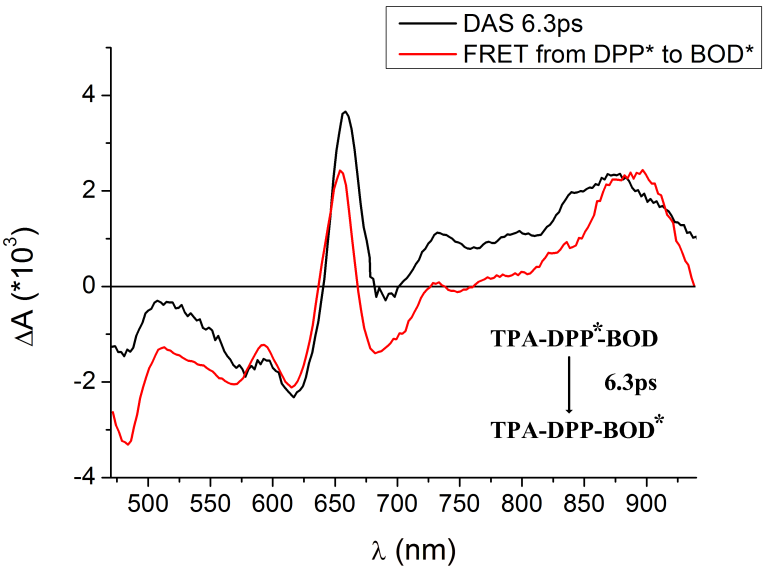

Figure 3.12: DADS associated with the 6.3 ps time constant from the pump-probe data global analysis. The DADS (black curve) features are well reproduced by the simulated red curve, corresponding to a fret from DPP* to BOD* (obtained from the ΔA spectra of DPP* and BOD*)

this contribution, we had to include the formation of TPA^+ and DPP^-, and an increase of DPP's bleach to obtain a correct fit.

$$DADS_{rec}(52ps) \propto c_1 * abs(DPP) - c_2 * \epsilon(DPP^*) + c_3 * \epsilon(DPP^-) + c_4 * \epsilon(TPA^+) \quad (3.3)$$

This combination of contribution is a bit surprising, for one expect the charge transfer state (TPA^+ and DPP^-) to be populated from DPP* (through a hole transfer), but this would not imply an increase of DPP's bleach. We could propose two explanations: either there is a population of TPA* that goes unseen on our spectral range that realizes an electron transfer to unexcited DPP, while in addition some new constraints imply a temporally coincident quenching of the DPP's SE. Or the hole transfer does occur (due to excitation of DPP* only, through the reaction TPA-DPP*→TPA^+-DPP^-), but leads to a state where the DPP GSB is for some reason increased. As fluorescence experiments indicated that no excited TPA is to be seen after the first few hundreds of fs, the former explanation does not hold, and only an increase of the DPP bleach explains our observations.

As for the previous DADS, the constants c_3 and c_4 are in theory equal, but differ here because of the uncertainty on the proportionality between the recorded ions spectra and their extinction coefficients.

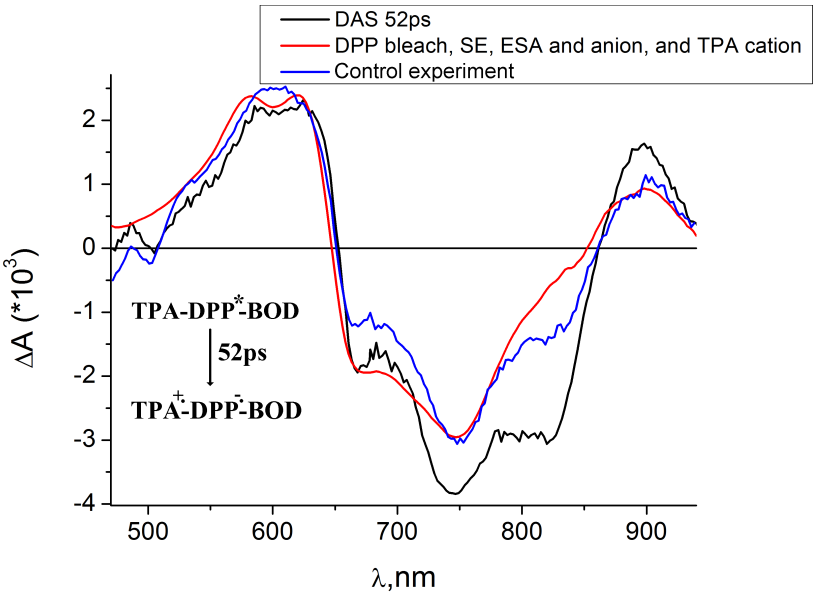

Figure 3.13: DADS associated with the 52 ps time constant from the pump-probe data global analysis. The DADS (black curve) is fitted with a decrease of DPP's excited state population (as hinted on by the time resolved fluorescence data, using DPP*), and with an increase of its bleach. Absorption of the TPA cation and DPP anion fit well the negative part of this DADS, indicating the formation of a charge transfer state. The blue spectrum results from a control experiment where particular attention was given to removing any noise in the 700 – 800 nm range.

The fourth DADS (500 ps) is shown in Fig. 3.14 , and is fitted (in red) by the disappearance of the CT state and BOD*, that happen to occur on the same time scale. Once again, the time resolved fluorescence correlates our observation, indicating that there is a decrease of BOD fluorescence within 500ps.

$$DADS_{rec}(500ps) \propto -d_1 * \epsilon(BOD^*) - d_2 * \epsilon(DPP^-) - d_3 * \epsilon(TPA^+) \quad (3.4)$$

The corresponding dynamics is the disappearance of the ions, and the relaxation of BOD*. For the same reasons as before, we expect (and do not actually have) $d_2 = d_3$. The quenching mechanism of BOD* remains unclear, since no clear photoproduct spectrum is being

formed. We attribute it tentatively to S_1S_0 internal conversion.

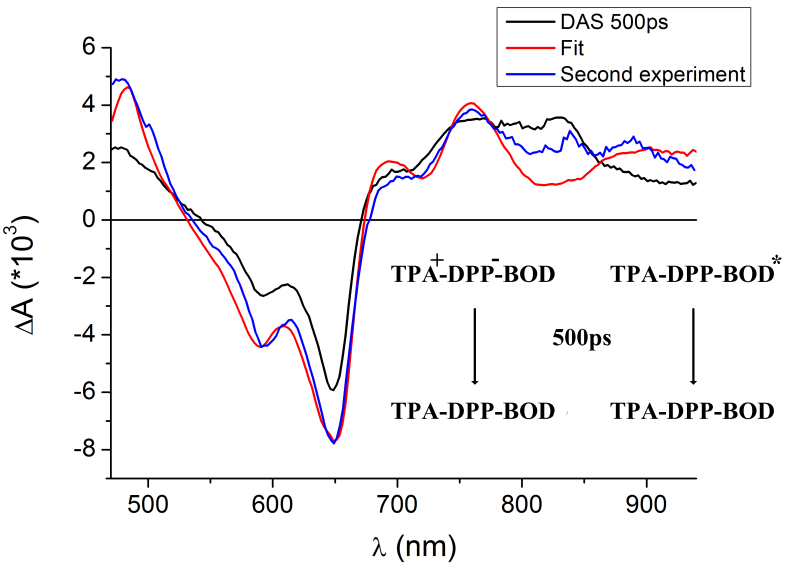

Figure 3.14: DADS associated with the 0.50 ns time constant from the pump-probe data global analysis. The DADS (black curve) fits very well with the simulated red curve, corresponding to a decrease of BOD* (as shown by the fluorescence data), and a decrease of the CT state population. Blue curve is the DADS resulting from a control experiment.

Lastly, the DADS associated to 2.2 ns is shown on Fig. 3.15, and reproduces the observations made with the time resolved fluorescence: both DPP* and BOD* relax to their ground states.

$$DADS_{rec}(2.2ns) \propto -e_1 * \epsilon(DPP^*) - e_2 * \epsilon(BOD^*) \qquad (3.5)$$

The different processes we observe for both DPP* and BOD* (the different reaction paths) translate a variety of populations in these states. The fact that DPP* is populated from TPA* via FRET may explain part of that: the fluorescence of TPA covers the two higher energy absorption peaks of DPP, which may results in the formation of DPP in its S_2 and S_3 states, each with a different decay pathway, that could lead to different spectrally undistinguished excited state conformations, and thus reaction paths. As well, BOD* is partially populated via FRET by DPP*, but the resonance between their absorption and fluorescence will allow only the lower vibrational states of BOD's S_1 states to be populated, while the direct excitation of BOD

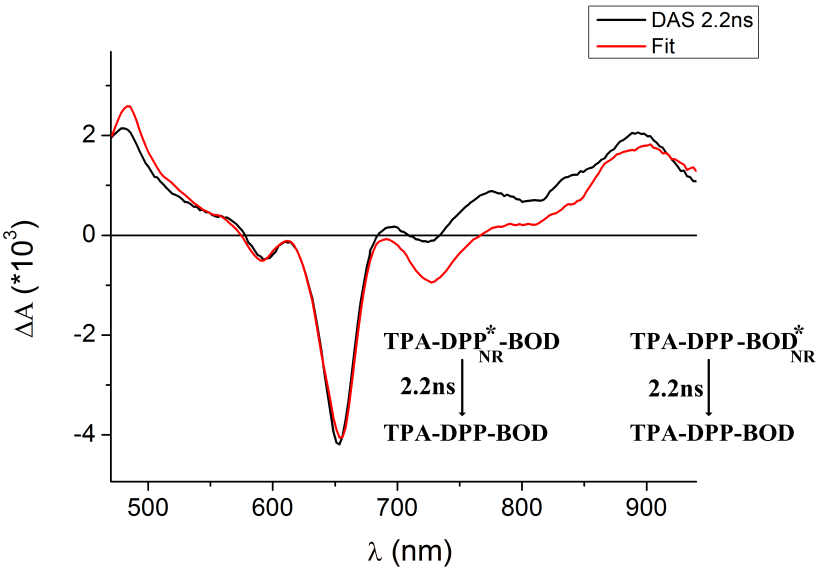

Figure 3.15: DADS associated with the 2.2 ns time constant from the pump-probe data global analysis. The DADS (black curve) fits well with the simulated red curve, corresponding to the sum of the DPP* and BOD* ΔA spectra, meaning that both excited species are decaying together. The "NR" index in the reaction scheme indicates that those excited populations seems to be non-reactive, as their lifetime is close to that of the isolated components.

(at 320 nm) goes through higher energetic states.

Using all those observations as blocks, we can construct a complete reaction scheme, depicted in Fig. 3.16. After excitation by the 320 nm pulse, the BOD and TPA moieties are excited as TPA* and BOD**. Within 300 fs, energy transfer(s) from TPA* to DPP occurs, immediately (indistinguishable in our experiment) followed by BOD and DPP relaxation from their S_n states to their S_1 states. This is followed in 6.3 ps by another energy transfer from a fraction of the DPP* population to BOD*. In 52 ps the CT state implying TPA^+ and DPP^- is formed, through a hole transfer from DPP* that for some unclear reason increases the amplitude of the bleach of DPP. This CT state lives for 500 ps and decays on the same time scale as a fraction of BOD*. Finally, the non-reactive fractions of DPP* and BOD* relax in 2.2 ns.

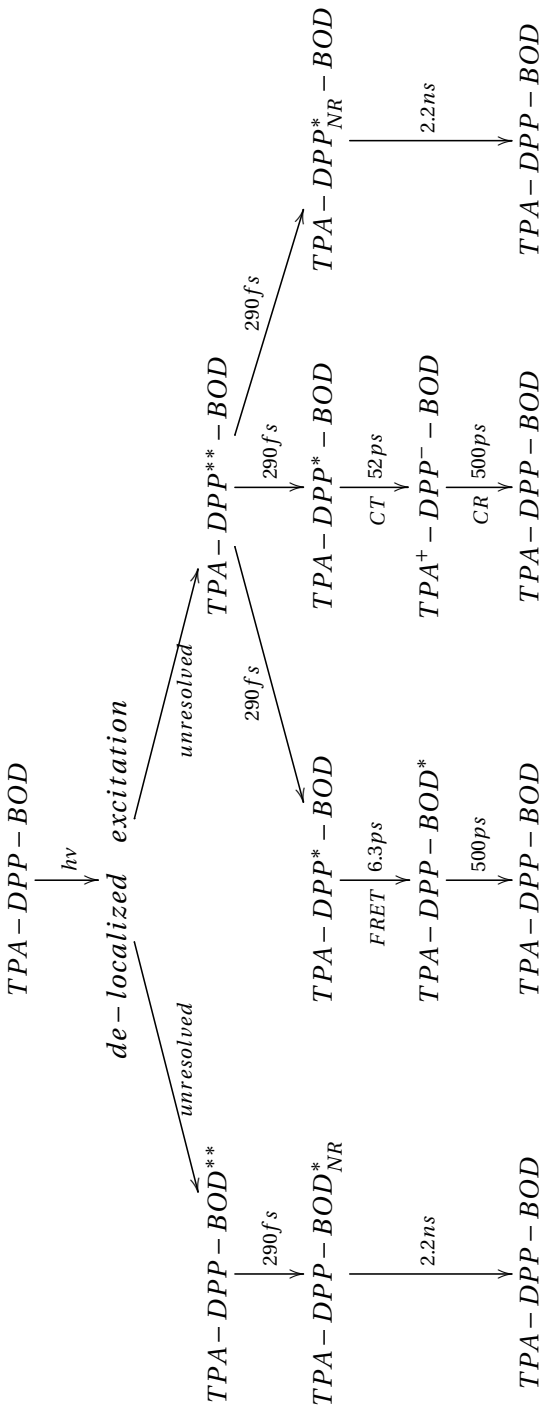

Figure 3.16: Reaction scheme compiled from the quantitative analysis of the DADS. See text for detailed explanations.

3.1.2.3 Conclusions

Two aspects can be developed here: the perspectives for the molecule, and the qualities of the methods used.

Taking into account that we studied the isolated molecule, instead of a blend with an acceptor, the performances of the antenna seem promising: indeed, we do have a fast energy transfer toward the BOD moieties validating the antenna effect, and even the formation of an intra-triad CT state, and since in a blend the time scale for CT formation is bellow 50 ps, it is expected that all longer-lived BOD* and DPP* will lead into CTs.

In a more general consideration, we showed that despite intricate signatures of the different species (and conformations), we can determine a rather precise reaction scheme using complementary experiments and a careful analysis of some relevant differential spectra, without resorting to a bi-dimensional spectroscopy experiment (that would directly reveal the different interactions between populations). Note that if we had used the target analysis approach, which would involve a trial-and-error procedure with a very large set of possible reaction schemes, the so-obtained SADS would also have to be validated by spectral decomposition of the individual species associated difference spectra. Our approach thus turns out to be very pragmatic and powerful in terms of identifying the most prominent reaction pathways in this flexible triad, obviously presenting a large degree of structural heterogeneity.

4

Liquid-Crystal Donor Acceptor

4.1 Principles

One of the main problems encountered with polymer blends is that they usually have very poor organization properties, and bad conductivity. The organization is of prime importance, as dissociation of the exciton into separated charges can only happen at an interface between the donor (D) and the acceptor (A). This implies that an ideal structure would present D/A interfaces separated by less than twice the diffusion length, typically 5 to 10 nm. The random organization obtained with blends of polymers can hardly provide such structures, as domains will be created of each material, with uncontrolled inter-digitation. As shown on Fig.4.1 A), some material may be too far from an interface to lead to a charge separation and some domains may be isolated from electrodes, leading to trapped (and lost) charges.

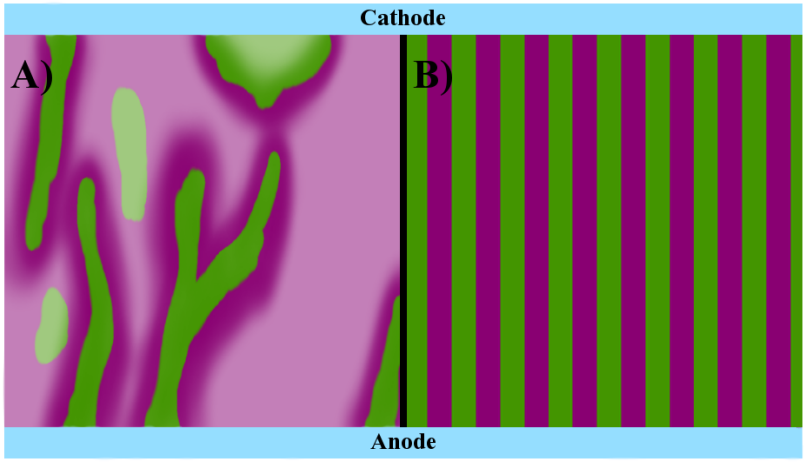

Figure 4.1: Schematic of a photovoltaic cell based on a polymer blend (left, "A)") or a liquid crystalline molecule (right, "B)"). Acceptor and Donor materials are depicted in green and pink. Only the material within the diffusion length of an interface and connected to an electrode is efficient, implying that a lot of the volume (which is represented here by a white halo) is lost for the photoconversion in the randomly organized polymer cell, whereas the liquid crystalline one -beside probable better conductivity- make use of all the material.

The use of molecules composed of both Acceptor and Donor moieties insures that an interface D/A will be at a minimum distance (<2 nm) from the photo-created exciton. If the material additionally shows liquid-crystal (LC) properties, this allows for a very good self-organized

structuration, where donors and acceptors will stack on each other, creating walls of each materials as sketched on Fig.4.1 B. This results in a cell where no material is wasted, and where good conductivity can be achieved [57,58], for example the first material discussed ("GHR") achieve a mobilities in the order of $10^{-3}.cm^2.V^{-1}.s^{-1}$ [59]. Among others, molecules based on a perylene bisimide core (as acceptor) substituted with a donor (usually an aromatic chain) were shown to be able to achieve such desired structures([60,61]), and promising performances (reaching 2.7% efficiency[62]).

4.2 First Generation Liquid-Crystal Donor-Acceptor Molecules "GHR"

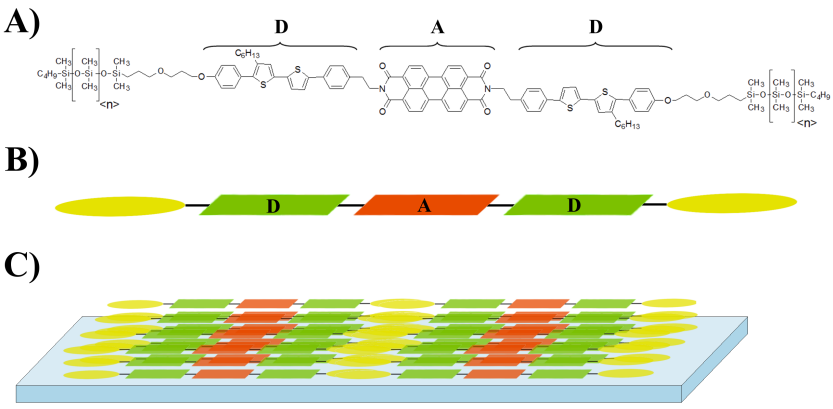

Figure 4.2: A) Chemical structure of the GHR molecule: the core acceptor(A) is a perylene diimide, surrounded by donor groups (D) made of a phenylthiophene derivative. Siloxane chains are attached at each end of the molecule, to assure the liquid crystal properties at ambient temperature. B) and C) Schematic representation of a GHR molecule and its organization in films: the different moieties of neighboring molecules stack to each others creating a possible 2D channel of conductance in a plan orthogonal to that of the substrate, and siloxane chains of different such "walls" also stack, aligning the whole structure into something close to what is shown in Fig.4.1 B

The molecules developed by Stéphane Méry and Gilberto Hernandez Ramirez[59] (thus the acronym GHR) are depicted in Fig.4.2 as well as their organization in liquid crystal film. The core of the molecule,

inspired by[63], is a perylene bisimide (A in the following), known as an acceptor with very good stacking properties, due to its flat structure. The donor groups attached at both sides of the perylene are phenylthiophene derivative (D). Siloxane chains of chosen length are then attached at the extremities of the molecules, providing the LC properties, their length defining the temperature range in which the smectic phase is achieved. Pump-probe spectroscopy experiments were first done on the separated components D and A, and then on the full molecule (DAD) in solution (in chloroform, $CHCl_3$), where the molecules are isolated from each other, and finally in film.

The results obtained by ultrafast spectroscopy are published in Ref.[64] and[65].

4.2.1 Preliminary results

Prior to the actual pump-probe experiments, static absorption and fluorescence spectra were recorded for the complete molecule as well as for A and D alone. As shown on Fig.4.3, we can characterize A's absorption as 3 vibronic bands, whose peaks are at 458, 490 and 527nm, and D's absorption as a broader band centered at 368nm. The absorption of DAD is the sum of the absorption of A and (twice) the one of D, revealing that almost no coupling happens between the different moieties of the molecules. This implies that within the full DAD molecule, we can consider the A and D moieties as separate entities, and that exciting the DAD molecule with a 400nm pump will excite only the donor part. That last element is quite important, as it gives us a fixed point for the analysis of the molecule dynamics: we will always start the process by the excited state of D.

Fluorescence spectra of the separated components and the full molecule were also recorded, as shown in Fig.4.3. D's fluorescence (starting at 410nm and ranging to over 550nm) overlaps with A's absorption, allowing for energy transfer between the 2 moieties. That's why we can recognize A's fluorescence (the mirror image of its absorption, with peaks at 536, 574 and 620nm) in the DAD fluorescence, even when exciting the D moieties at 350nm. Yet, this fluorescence of the triad is extremely weak (about 150 times smaller) compared to that of the separated molecules, which indicate that new phenomena occur in the triad, that quench its fluorescence.

Finally, a third set of preliminary experiments were made by Sabine Ludwigs and Olena Yurchenko by spectro-electro-chemistry (see chap-

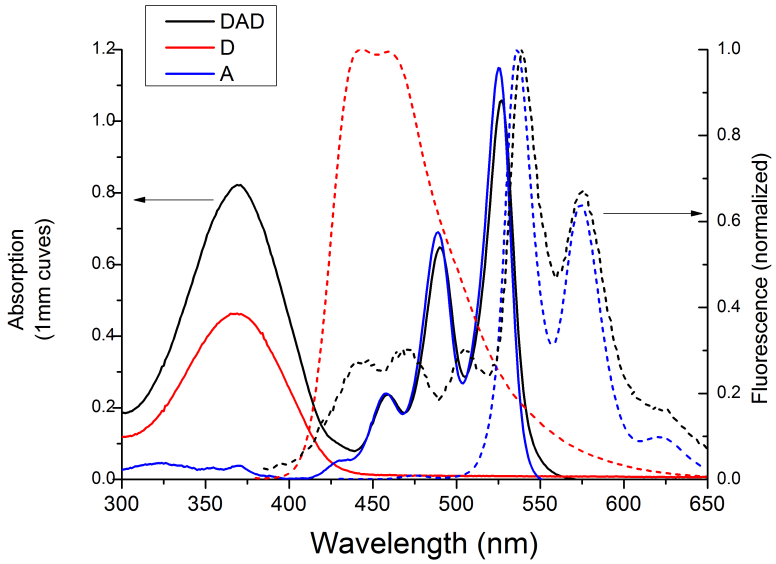

Figure 4.3: Plain lines: Absorption Spectra of D, A and DAD in a 1mm cuve, at a $1.5 * 10^{-4}$ $M.L^{-1}$ concentration in $CHCl_3$. Almost no coupling effect can be seen as DAD's spectrum is very close to the algebraic sum of D and A's spectra. Dashed lines: Normalized fluorescence spectra. DAD fluorescence is ~ 150 times weaker than the ones of isolated D's and A's.

ter 2.5). As we are aiming at identifying the presence (or absence) of charged species, knowing their spectral signatures is of great help to analyze the ΔA spectra and support our conclusions. These spectra, obtained in dichloromethane (DCM) are shown in Fig.4.4. A^- is easily recognizable as it is characterized by three distinct peaks at 717, 796 and 957nm. D^+ signature consists in two peaks, at 538 and 623nm.

4.2.2 Ultrafast transient absorption in solution

4.2.2.1 The perylene diimide, block A

The A moiety was first studied alone in $CHCl_3$ by pump-probe spectroscopy, in order to have an identification of the spectral signature of A*. As the absorption of A is almost null at 400 nm, third harmonic of the laser was used (at 266nm) as pump. This results in the excitation of A in its S_2 state. Fig.4.5 A) shows a few selected ΔA spectra that reveal the dynamics of A.

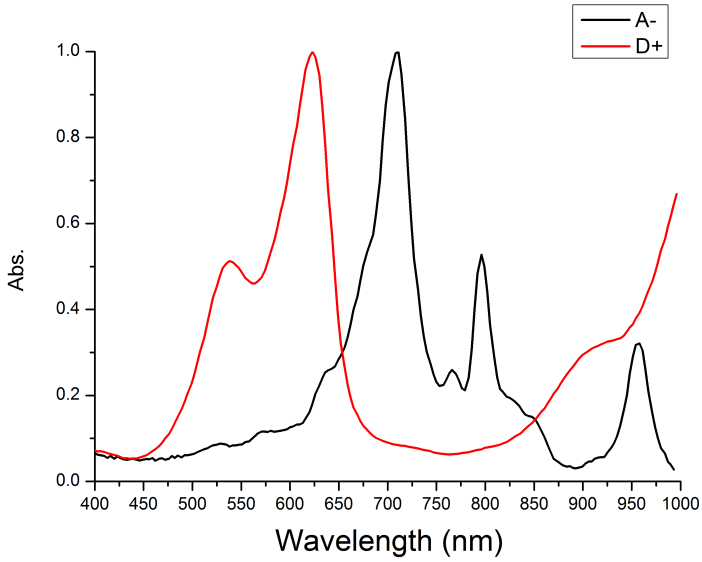

Figure 4.4: Normalized absorption spectra of D cation (D^+) and A anion (A^-) radicals obtained by spectro-electro-chemical measurements in DCM. A^- shows 3 sharp peaks at 711nm, 796nm and 957nm. D^+ has a main absorption peak at 623nm, with a smaller one at 538nm

While the bleach component (with negative peaks at 458, 490 and 527 nm) stays constant after excitation, the stimulated emission (negative peaks at 536, 574 and 620 nm, the first peak merging with the last peak of the bleach at 527 nm) rises over several ps (until 35 ps) and then no more changes in the spectra can be observed. Fig.4.5 B) overlaps the ΔA spectrum at 85 ps (representative of A*) with the static absorption and fluorescence of A, showing the almost perfect concordance between those 3 and that the attribution of these ΔA spectra to A* is correct. From this, we can characterize the ESA of A as bands below 440 nm and above 640 nm.

4.2.2.2 The diphenyl bithiophene, block D

The same study was performed for the donor moiety. As seen on Fig.4.6, after excitation (at 400 nm), the molecule first undergoes very fast changes in the first picosecond (not shown), and the stimulated emission can be detected in the 450-500 nm region until **~ 100** ps, at which point the shape of the ESA changes. The sub-ps relaxation can be attributed to intra-molecular relaxation or to rotations of the cycles

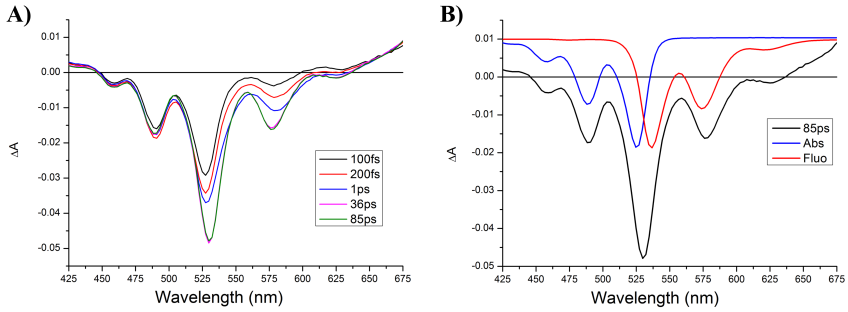

Figure 4.5: A) chosen ΔA spectra showing the dynamic of A after excitation at 266nm in its S_2 state, and B) comparison with absorption and fluorescence of A, scaled and shown upside-down. The bleach of A is instantaneous, while the stimulated emission rises slowly as the S_2 state decays in S_1

in the donor chain leading to a planarization of the molecule[66,67,64]. The latter changes are attributed to intersystem crossing, and the formation of the triplet state of D, following refs[66] and[67].

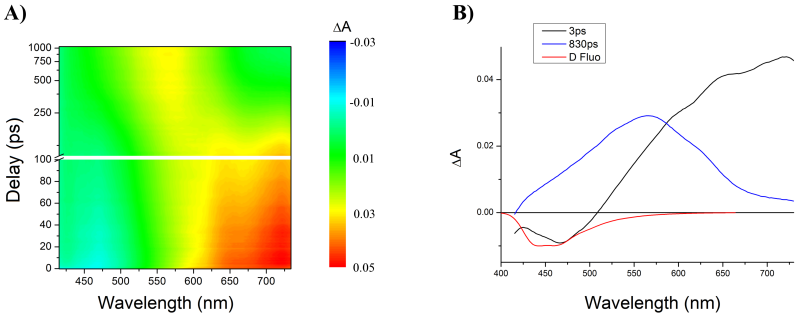

Figure 4.6: A) 2D map of D's differential absorption after excitation at 400 nm, and B) chosen ΔA spectra showing the 2 different states observed, and the fluorescence of D, scaled and shown upside-down. After a first fluorescing state, the molecule relaxes into a non-radiative triplet state in about 100 ps.

4.2.2.3 DAD

The signature of the two separated components being known, we then carried out the experiment on the full DAD molecule. Selected ΔA spectra are shown in Figs.4.7 and 4.8. The former one shows the early dynamics, while the latter presents the end of the reaction, alongside pertaining reference spectra. On Fig.4.7 top panel, we can see that the donor GSB (the negative band between 350 nm and 420 nm) increases immediately as expected when exciting at 400 nm, but decreases after 100 fs in favor of the acceptor GSB (negative peaks at 458, 490 and 527 nm) and stimulated emission (negative peaks at 536 and 574 nm). This reveals a fast FRET (Förster resonant energy transfer) from the donor excited state (noted D*) to the acceptor excited state (A*), made possible by the good overlap between the donor's emission and the acceptor's absorption (for indication, the calculated förster radius is larger than 4 nm). As those differential spectra were recorded up to 750 nm, we can identify better A* ESA, which is the main positive signature after 200 fs: a broad absorption at wavelengths longer than 640 nm, with a peak at 708 nm.

The later dynamics are shown in Fig.4.8: from 540 fs to 10 ps, while the acceptor GSB is constant, its stimulated emission decreases, the donor GSB increases again, and the ESA changes from a peak at 708 nm to two peaks at 717 and 623 nm. The coexistence of the 2 bleaches indicates that both species are implied, and comparison of the induced absorption with the spectra obtained via spectro-electrochemistry shown on the bottom panel (slightly red shifted, which can be explained by the change of solvent from DCM to chloroform) reveals that the charged species were formed (D^+A^-D). ΔA spectra at longer times only show a decrease of the signal amplitude, with no changes in their shapes, as the charged species recombine to the ground state of the molecule.

From those observations, we can identify the different steps of the DAD's photo-induced dynamics as the following:

$$DAD \xrightarrow{h\nu} D^*AD \xrightarrow{FRET} DA^*D \xrightarrow{CT} D^+A^-D \xrightarrow{recombination} DAD$$

Fitting the kinetic traces was needed in order to obtain the time constants associated to each transition. This was first done on selected traces (as shown on Fig.4.9) to isolate each phenomena, and then on the whole data via global fitting. Those fits revealed 3 time constants: 130

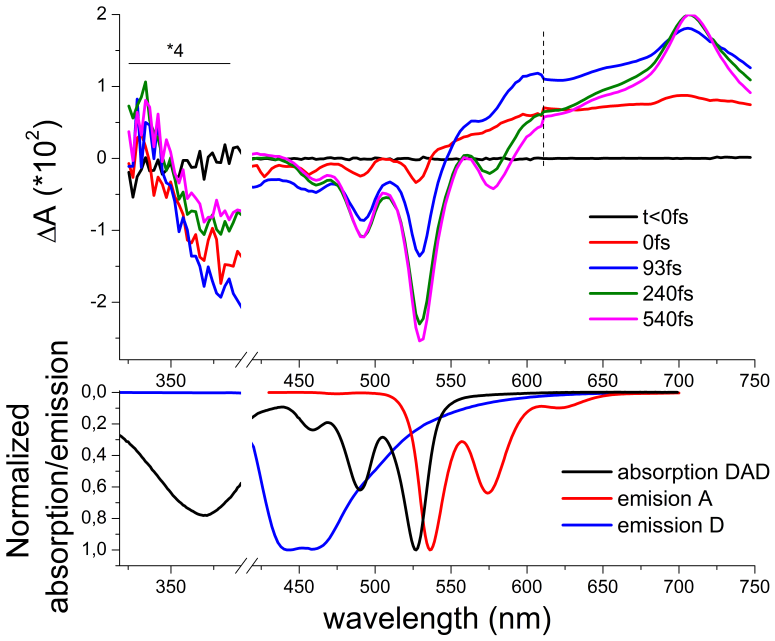

Figure 4.7: Top panel: chosen ΔA spectra from 0 to 540fs, showing the rise of the excited donor's signal (D*, from 0 to 93 fs) and its decay to the signal of excited acceptor (A*, later ΔA spectra). Dotted line shows where the two sets of data were merged. Bottom panel: upside-down absorption spectrum of DAD (black) and emission spectra of A (red) and D (blue)

fs, 2.7 ps and 55 ps, respectively associated to the energy transfer from D* to A*, the charge transfer state formation, and the recombination to the ground state (c.f. table 4.1).

Which allows us to get a more precise reaction scheme:

$$DAD \xrightarrow{h\nu} D^*AD \xrightarrow[130fs]{FRET} DA^*D \xrightarrow[2.7ps]{CT} D^+A^-D \xrightarrow[55ps]{recombination} DAD$$

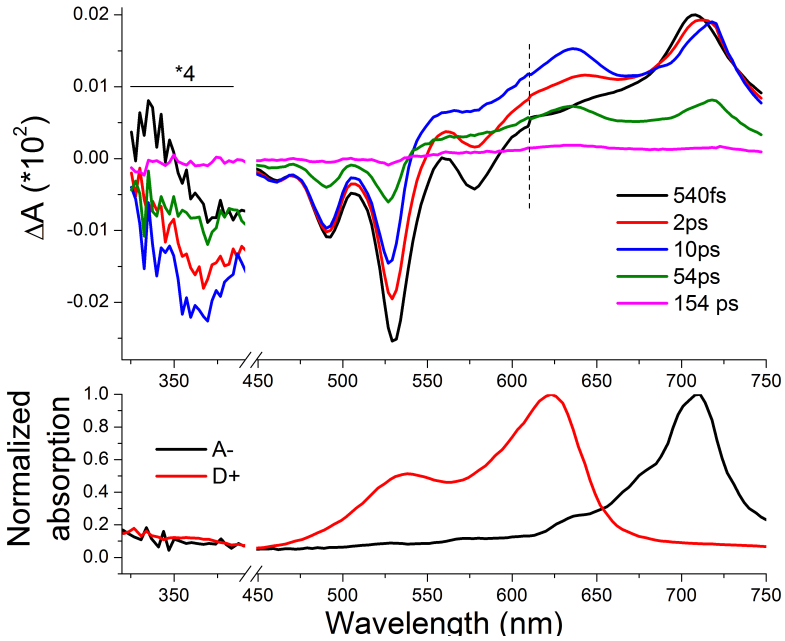

Figure 4.8: Top panel: chosen ΔA spectra from 540 fs to 154 ps, showing the transition from A* to the charge transfer state (D^+A^-D, from 540 fs to 10 ps), latter spectra show the decay to the ground state. Dotted line shows where the two sets of data were merged. Bottom panel: spectra of the two charged species in DCM. A small shift can be observed for both peaks in the ΔA spectra (from 623 to 635 nm and from 711 to 718 nm), which can be attributed to the different solvent used (chloroform)

4.2.3 In films

The study of the DAD molecule in solution gave us insights on the behavior of individual molecules. The study of the molecule in films will add the interaction effects between neighboring molecules, in conditions close to those in an actual solar cell (under short circuit conditions, V=0). Films were made by spin-coating a highly concentrated solution of DAD on fused silica substrates under protective atmosphere (nitrogen filled glove boxe). To avoid bleaching during the pump-probe experiments, films were held on a loudspeaker oscillating at 1 Hz. To prevent oxidation they were studied either in a nitrogen filled box (with fused silica windows for the laser beams), or encapsulated with another fused silica plate glued on the substrate.

As shown in Fig.4.10, an inter-molecular excitonic coupling between neighboring DAD molecules leads to a red-shift of the absorption bands

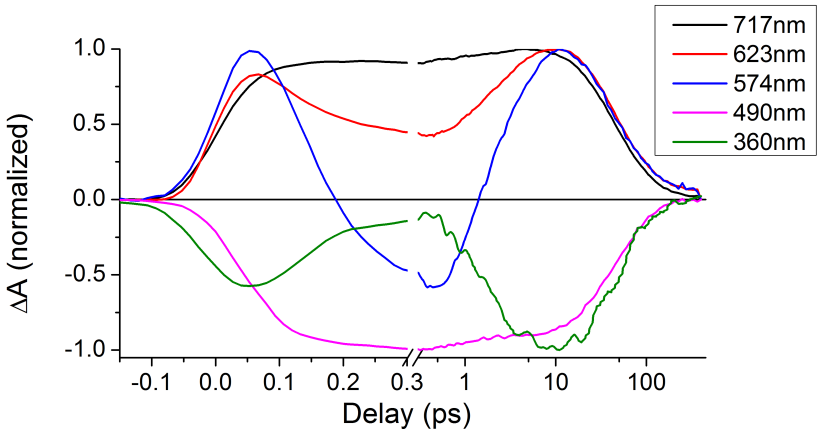

Figure 4.9: Kinetic traces of DAD in $CHCl_3$ at selected wavelengths: 717 nm (black, after a few ps: maximum of the A^- absorption), 623 nm (after a few ps: maximum of D^+ absorption), 574 nm (between 100 fs and a few ps: stimulated emission of A), 490 nm (A's bleach), and 360 nm (D's bleach). One can clearly see here that A's bleach rises when D's one decreases, just as A's SE rises. The latter decreases as D's bleach increases again when the charged species are formed, as shown by the rise of the 2 ions absorption bands.

of 0.1 eV (for example the reddest peak shifts from 527 nm to 551 nm), a decrease of the relative amplitude of the acceptor absorption band, and the appearance of a broad tail in the red side of the absorption band, between 575 and 675 nm. This bathochromic shift suggests excitonic coupling under J-aggregates-like conformations, meaning that the stacked molecules are not aligned side-by-side, but displaced with respect to each other along the molecular axis[68]. This matches well the first molecular organizations computed by Cyril Bourgogne using considerations about the molecular areas, that indicated an organization either in "Z" or "stretched" (see page 95 of[59]). Further investigations concerning the simulation of the dynamics are in progress by Irene Burghardt and her team (Frankfurt University, ANR-DFG project MolNanoMat).

The dynamics revealed by the pump-probe experiments (as shown in Fig.4.11) are quite different from those observed in solution. Indeed even at very short times (top panel) no stimulated emission of A^* is detected, and both bleaches rise almost simultaneously, indicating that the excited state D^* is extremely short lived (better seen with the 448 nm kinetic trace on Fig.4.12 A panel). The species then formed imply both D and A, with two shallow and broad absorption bands at 640 and

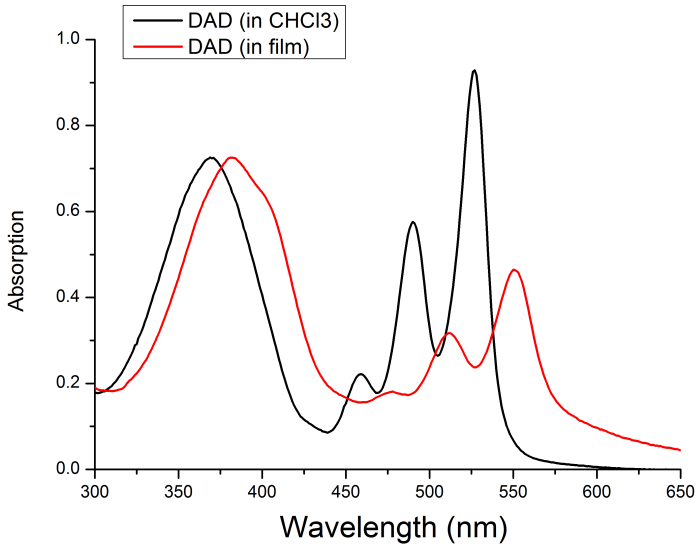

Figure 4.10: Absorption spectra of DAD in solution and in film. The relative amplitude of the acceptor absorption band decreases in film compared to the one of the donor, and a red-shift of about 0.10 eV occurs. A low-energy tail appears in the 575-675 nm region.

730 nm (spectra for t > 440 fs). Those are attributed to (respectively) D^+ and A^-, red shifted with respect to the spectra in solution. This charge transfer state then decays over more than 100 ps into the ground state and some triplet states (DAD^T) are formed (more precisely the triplet state of A, as shown on Fig.4.12 panel B[69,70]), as shown in the bottom panel, where even differential spectra at delays longer than 3 ns still indicate a bleach of A. So, the first observation made is that in film the FRET from D to A is overcome by a faster charge transfer.

Further observations need the fitting of the data as previously done in solution. Here the expected dynamics is :

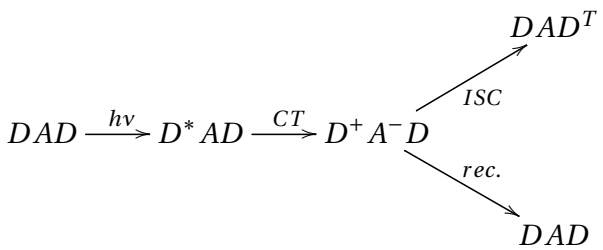

However, fitting the kinetic traces (example shown on the 552 nm

	Solution	Film		
	τ	τ	Bleach D	Bleach A
RET	130 (20) fs	-	-	-
CT	2.7(0.2) ps	<100 fs	-	-
Rec1	-	1.1 ps (0.2)	36 %	37 %
Rec2	55(5) ps	70 ps (10)	46 %	40 %
Rec3	-	1.3 ns (0.3)	18 %	10 %
Triplet	-	> 5 ns	-	13 %

Table 4.1: Time constants (with incertitude) and amplitudes for fits of DAD in solution and in film. The three CT recombination processes are denoted Rec1 to Rec3. Relative amplitudes in films are given for the bleach of D and A to highlight the difference in relative amplitudes due to the triplet formation.

trace in Fig.4.12 panel A, due to bleach of A) reveals that the decay of the charge transfer state takes place via 3 different channels. Indeed, the time constants needed to fit the GSB data of A are: 60 fs, 1.1 ps, 70 ps, 1.3 ns and an "infinite" time constant (used for the triplet lifetime, which is much larger than the maximum possible with our delay line). The first time constant (60 fs) is a rise time, attributed to the formation of the charge transfer state, and the 3 following ones correspond to recombinations. This first time constant of 60 fs is extremely short, and almost unresolved. Yet, comparing the IRF-limited rise time of the traces at 448 nm (Fig.4.12 panel A, attributed to D* SE), 641 nm and 730 nm (both related to the ESA of D) with the rise time of the 552 nm trace (attributed to A GSB), one can see that the latter is not as sharp, and correspond to the decay of the SE of D at 448 nm. This means that we do observe the decay of the donor SE in favor of the bleach of A, as the CT state is formed. The 70 ps recombination process occurs on a time scale comparable to what is observed in solution, and thus attributed to an intra-molecular recombination. Longer recombination occurring on 1.3 ns is assigned to inter-molecular recombination, for charges that were delocalized on neighboring molecules (as they are further separated, their interaction becomes weaker and leads to a slower recombination). The fastest recombination component (1.1 ps) can either be attributed to a faster intra-molecular recombination channel made possible by geometrical constraints, or to a bimolecular recombination process (in which case 2 charges pairs were created on neighboring molecules, and recombine).

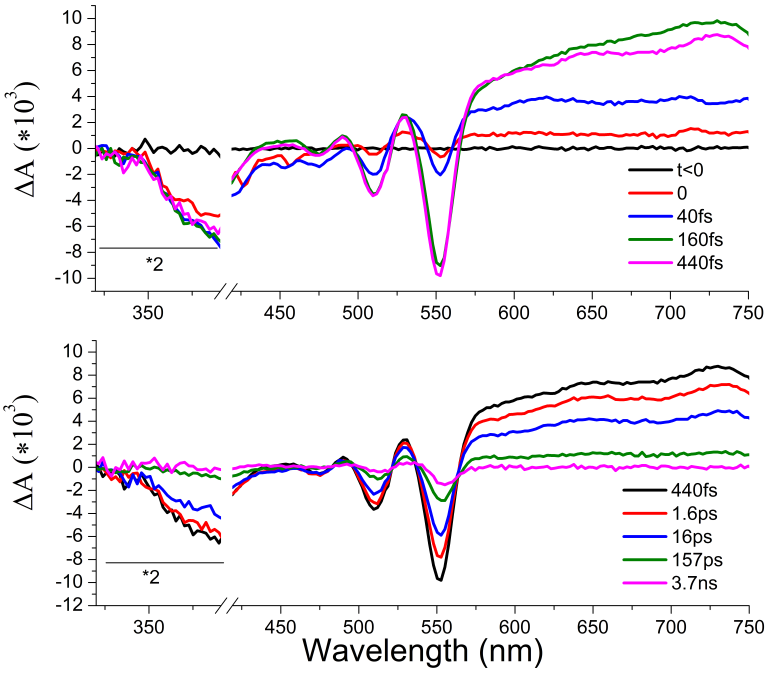

Figure 4.11: Top panel: chosen ΔA spectra of DAD in film, from 0 fs to 440 fs, showing that in 160 fs, both D and A GSB are at their maximum amplitude, with only a very short lived SE of D below 500 nm that has already disappeared at 160fs, and a very broad ESA that overlaps with A bleach over 450 nm . At longer delay (already at 440 fs), one can instead see 2 broad bands centered on 640 and 730 nm that we associate to the charged species. Bottom panel: chosen ΔA spectra at longer times (from 440 fs to 3.7 ns, showing the decrease of the signal intensity, and the remaining signal at very long times (>3 ns) associated to the formation of triplet states.

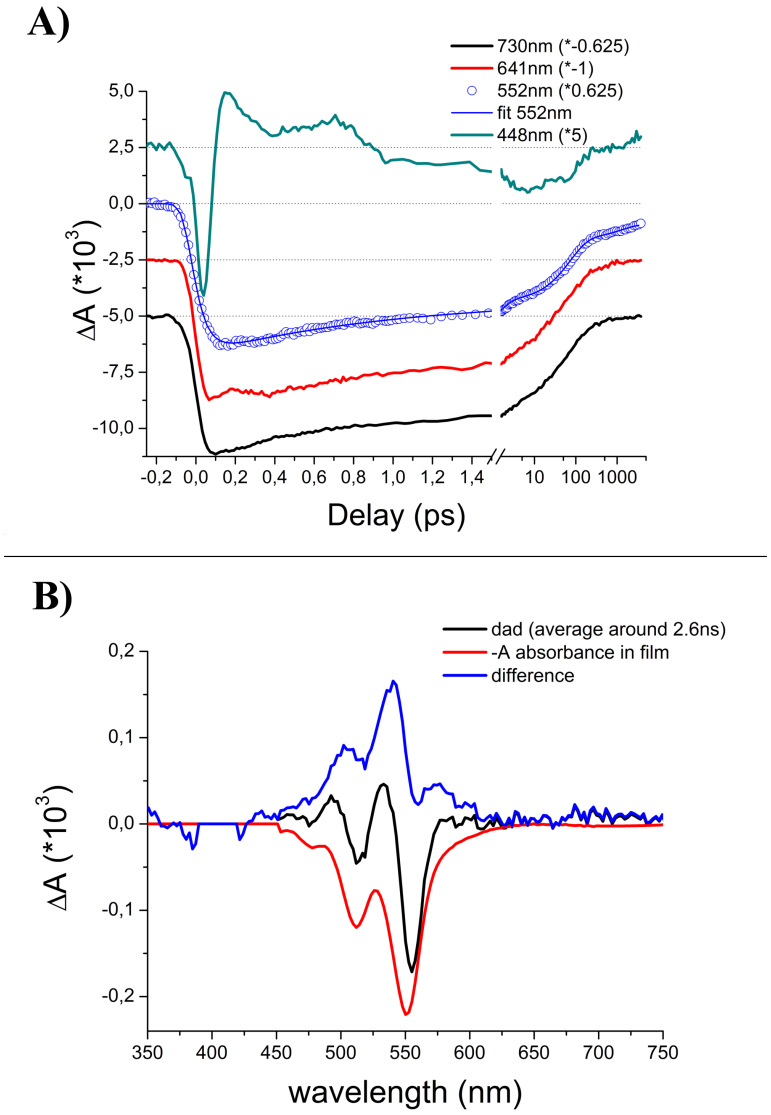

Figure 4.12: A) Kinetic traces at selected wavelengths of DAD in film, normalized and shifted for easier comparison. Only a very brief stimulated emission from D can be observed (at 448 nm) during the first 100fs, after which A's bleach (552 nm) and ions absorptions (641 and 730nm) follow the same dynamics. The only difference lies in A's bleach that doesn't recovers to 0 at long times, as some triplet states are formed. B) Average of the differential spectra at long times showing residual signal. Comparison of this signal with expected bleach of A reveal an induced absorption similar to the perylene triplet absorption[69,70].

4.2.4 Discussion

The different recombination times observed in films are associated to different CT states, eventually formed on neighboring molecules. This is explained by the extremely fast formation of this CT state, that is faster than the usual localization time of excitons. This means that the charge transfer occurs while the excitation is still delocalized over several neighboring molecules, and that the subsequent localization of the "positive and negative charges" may not occur on the same molecule. Compared to solution, the dynamics in the films seem favorable to an efficient conversion of light into charges: indeed the charge transfer state is achieved almost immediately, leaving very little time for other processes (radiative relaxation) that could reduce the conversion efficiency. Yet, very poor performances were achieved in the solar cells that were tested, with a record power conversion efficiency (PCE) below 0.01%. Besides organization problems (most of the self-assembled conduction layers are parallel to the substrate instead of orthogonal as on Fig. 4.2), this can be understood as the consequences of two hindrances. First, the relatively short lived charge transfer state, as almost 80% of the CT states recombine in less than 100 ps, leaving a very short time for charge separation in the device. Second, the formation of triplet states, which are very long lived and will accumulate in a continuous excitation regime: if these triplets do not contribute to the PCE, this leads to the effective loss (for photo-conversion) of all the molecules in this triplet state[71].

4.3 Second Generation Liquid-Crystal Donor-Acceptor Molecules "POS"

4.3.1 Introduction

Following the results on the previous "GHR" DAD molecules, the work was extended in order to keep the idea of a self-organizing structure alternating donor and acceptor domains, but with several improvements. The conclusions we had from the "GHR" molecule were that the rather short life-time of the CT states and -to a lesser extent- the triplet formation were major problems. Beside the siloxane chains, if very convenient for the LC state, had no use in the photodynamics and are thus "wasted volume".

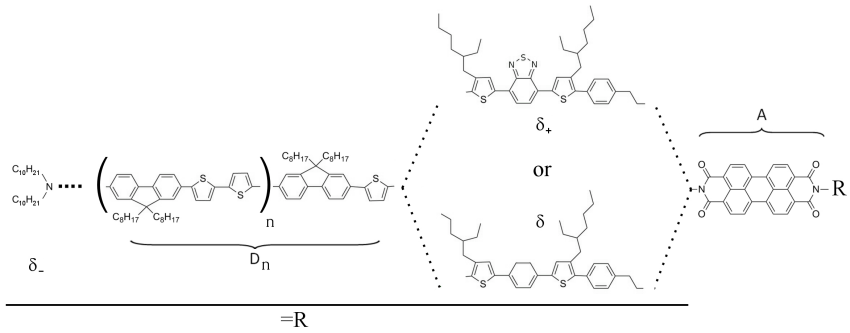

Figure 4.13: Sketch of the chemical structure of the DAD and DA molecules.

The new molecules "POS" (from the name of Pierre-Olivier Schwartz that developed them with S. Méry[72]) form a whole family of molecules with slight variations possible, so that we can study the impact of several parameters. This family is depicted in Fig. 4.13: around a perylene diimide core as acceptor a donor block of variable length can be attached, composed of a thiophene and a fluorene group, and a variable number n (from 0 to 2) of fluorene-bithiophene units noted D_n. This donor block is separated from the acceptor group by a bridge more or less electrodeficient noted (respectively) δ_+ or δ. This bridge is made by a benzene and a thiophene unit, either a benzothiadiazole (for δ_+) or a benzene (for δ) and a second thiophene unit. Furthermore, a terminal amine can be added at the other end of the donor

block, then noted δ_-. Those molecules where produced both as dyads (D-A) and triads (D-A-D or A-D-A).

This variety of donors is expected to change independently the location and energy of the donor's HOMO with respect to the acceptor LUMO, which should impact on the molecule dynamics and more importantly on the charge transfer formation rate and lifetime. The effect of the δ_- group was later shown to effectively re-localize in its vicinity the donor group HOMO, as shown on Fig. 4.14, where the calculated HOMO and LUMO of $A\delta_+D_2$ and $A\delta_+D_2\delta_-$ are represented. In the following, we will study the behavior of a variety of these molecules, to identify the effects on the dynamics of these parameters with a special emphasis on the CT state formation and recombination times. Then, we will discuss those results within the frame of the Marcus theory.

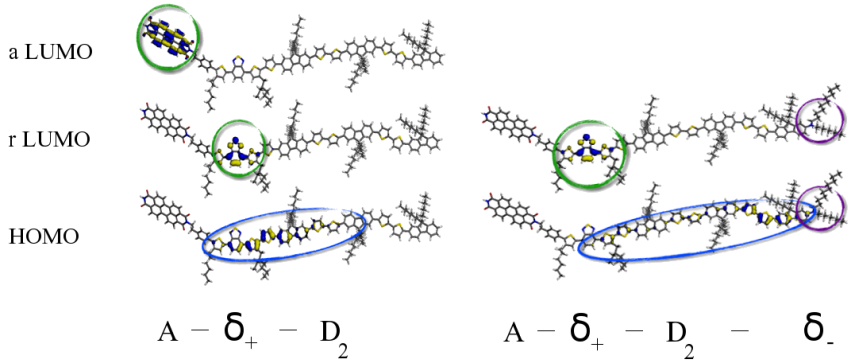

Figure 4.14: Calculated HOMO and LUMO orbitals of the $A\delta_+D_2$ and $A\delta_+D_2\delta_-$ dyads. Addition of the terminal δ_- group shifts the HOMO from the vicinity of the bridge to that of δ_-. Calculations and figures from Guido Ori.

Besides isolated components (D_n, δ_+, $D_1\delta$, $D_1\delta_+$ and A), the different studied molecules are (grouped by comparisons): $D_1\delta A\delta D_1$ and $D_1\delta_+A\delta_+D_1$ to highlight the effect of the δ_+ group, then $D_1\delta_+A$ to compare with the former to check whether dyads and triads behave identically (and allows for further comparisons, as most of the possible molecules combinations were synthesized as dyads). The effects of the δ_- group are then investigated by the study of both $\delta_-D_1\delta_+A$ and $\delta_-D_1\delta A$. In a second time, $D_0\delta_+A$, $D_2\delta_+A$ and $D_3\delta_+A$ were used to check the effects of the donor length. A recapitulation of these molecules can be found in Table 4.2.

		donor length →			
		D_0	D_1	D_2	D_3
donor composition ↕	$\delta_- D_n \delta$		$\delta_- D_1 \delta A$		
	$D_n \delta$		$D_1 \delta A$		
	$D_n \delta_+$	$D_0 \delta_+ A$	$D_1 \delta_+ A$	$D_2 \delta_+ A$	$D_3 \delta_+ A$
	$\delta_- D_n \delta_+$		$\delta_- D_1 \delta_+ A$		

Table 4.2: Table showing the studied molecules among all the possible arrangements. We chose to study a selection of molecules so that we can examine the effects of the donor length (along a given line) and of the donor composition (along a column).

4.3.2 Results

4.3.2.1 Steady-state Spectroscopy

The static absorption and fluorescence spectra of D, δ_+ and $D\delta_+$ in solution in chloroform are reported in Fig.4.15, and reveal that there is an electronic coupling between the D and δ_+ parts, as the resulting absorption and fluorescence are red shifted: the main absorption peak from D shifts from 408 nm to 421 nm, and the reddest band of δ_+ shifts from 480 nm to 504 nm; fluorescence from δ_+ shifts from 598 nm to 647 nm. On the opposite, no significant change neither in absorption nor in fluorescence occurs when δ_- is added (not shown). Furthermore, we can already note that if D's fluorescence overlaps well with A's absorption (from 450 nm to 540 nm as previously shown[65]), this is not the case with $D\delta_+$, which indicates that no energy transfer should be expected from $D\delta_+$ to A. Also, the absence of shift of the respective absorption peaks of the donor and acceptor moieties in the spectrum of $D_1\delta_+A$ indicates that there is no electronic coupling between them.

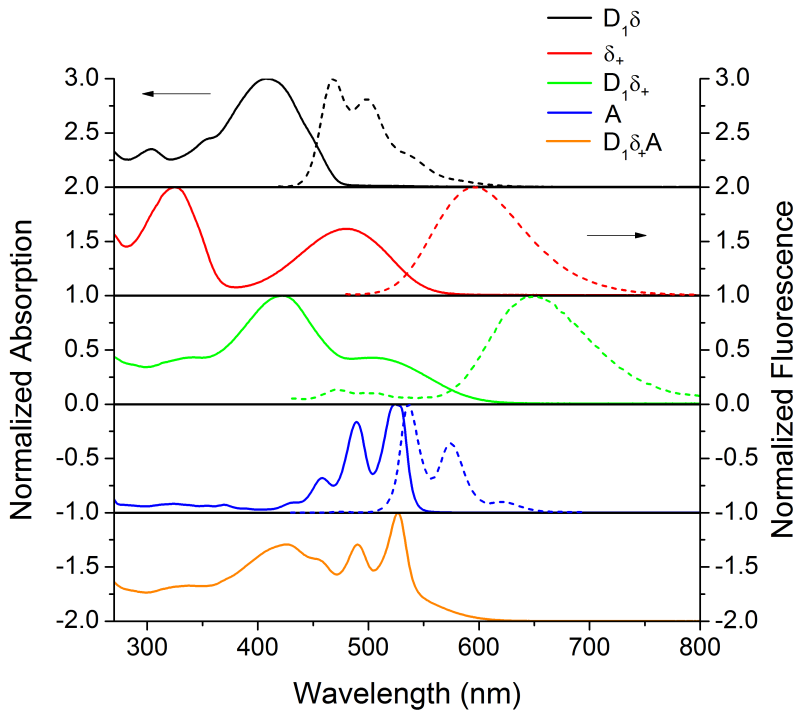

Figure 4.15: static absorption (plain) and fluorescence (dashed) spectra of D (black), δ_+(red), $D_1\delta_+$ (green), A (blue), and $D_1\delta_+$A in $CHCl_3$, normalized and vertically shifted for easier reading. Both absorption and fluorescence show a red shift when associating D and δ_+. Additionally, one can note that the fluorescence of D is quenched in $D\delta_+$ in favor of the one of δ_+

4.3.2.2 Dynamics

Fig.4.16 shows a few selected ΔA spectra obtained for $\delta_- D_1\delta A$, whose dynamics will be used as reference in the following. Comparison between those ΔA spectra and spectra obtained in separate transient absorption experiments for isolated components allows the identification of the different steps of the molecule dynamics.

In this case, comparison of the first ΔA spectrum (93 fs, black line) with the sum of absorption and fluorescence spectra of $D_1\delta$ shows that we indeed have the excitation of the donor moieties of the molecule, with the GSB and SE of the donor group $(\delta_- D_1\delta)^* A$. Analysis of the second ΔA spectrum (4.1 ps) reveals that we have a decrease of the excited donor group signatures (bleach and stimulated emission), in

Molecule	State	Characteristic peak(s)
D	GSB	409 nm
	ESA	697 nm
	SE	468 nm and 499 nm
	cation	707 nm
δ_+	GSB	323 nm and 478 nm
	SE	598 nm
Dδ_+	GSB	343 nm, 420 nm and 510 nm
	SE	651 nm
A	GSB	460 nm, 490 nm and 526 nm
	ESA	709 nm
	SE	536 nm and 575nm
	anion	719 nm, 803 nm and 970 nm

Table 4.3: Spectral characteristics of the different participating species. Central wavelengths of the main peaks are given. ESA values for δ_+ and Dδ_+ are not given as several excited states are observed.

favor of the appearance of GSB and SE of A, which indicates that we observe an energy transfer from $(\delta_- D_1 \delta)^*$ to A^*, with an ESA at wavelength over 600 nm similar to that observed in Fig. 4.7, with its characteristic peak at 708nm. For those two ΔA spectra, reconstruction of the expected GSB+SE (for D or A) is overlapped (dashed lines). The two last ΔA spectra (102 ps and 3.4 ns) reveal the CT state of the molecules, which can be seen through the presence of the bleach of both A and D, no SE, and the characteristic absorption bands of the ions (at 720, 806 and 965 nm). This is confirmed by the good agreement between the induced absorption and the sum of $D^+ + A^-$ absorption (dashed line).

Comparison of pump-probe results on the other molecules mainly reveal three effects of the molecule architecture on their photo-dynamics, that are developed in the following. First is the impact of the electronegativity of the δ group on the short times: in presence of the δ_+ group, no energy transfer (FRET) can be seen between the donor and the acceptor moieties of the molecules. The second effect is the stabilization of the CT state obtained by adding the δ_- group, that relocate the HOMO farther from the acceptor's LUMO (cf. Fig 4.14). Lastly we can observe that changing the donor length (D_0 to D_3) does not impact significantly the dynamics.

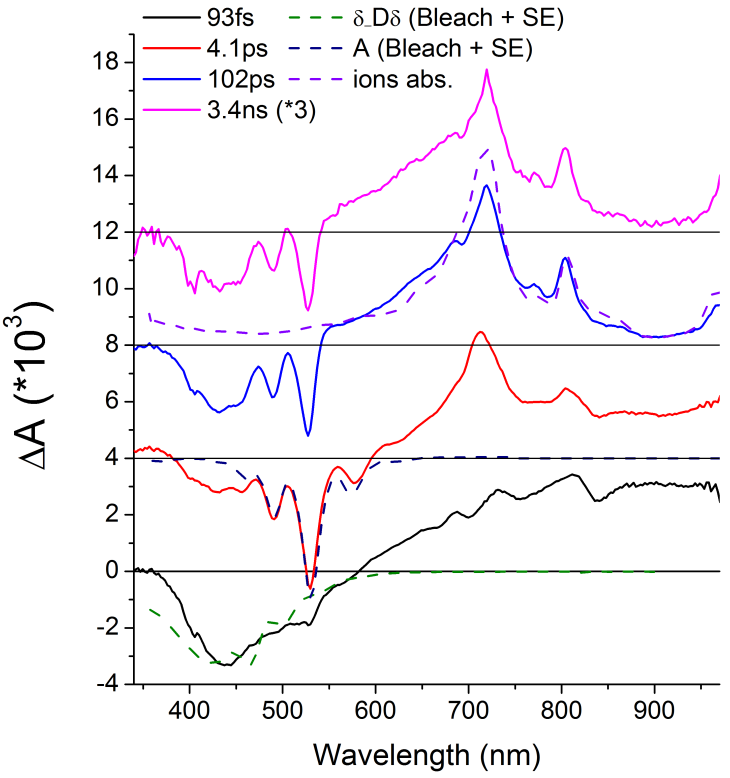

Figure 4.16: Selected ΔA spectra recorded at Δt = 93fs (black), 4.1ps(red), 102ps (blue) and 3.4ns (pink, scaled *3) on the molecule $\delta\_D_1\delta A$ in $CHCl_3$, after excitation at 400 nm. Comparison with spectra recorded separately (of known species) allows to identify for each ΔA spectrum the actual state of the molecules, which are (respectively): excited donor (D^*), excited acceptor (A^*), charge transfer state (D^+A^-), decaying population of CT state

4.3.2.3 impact of δ_+ on FRET

In molecules without δ_+ groups, such as $D_1\delta A\delta D_1$ and $\delta\_D_1\delta A$, after selective excitation of the donor a rapid FRET (within ps) to the acceptor can be observed, as shown in Fig. 4.17. Indeed, compared with the 80 fs spectrum of δ_D$_1\delta$A, the one at 3.5 ps shows a decreased bleach of D (400-450 nm band), increased bleach of A (460, 490 and 526 nm), and more importantly SE of A (536 and 575 nm).

The addition of the δ_+ group red-shifts (from 500 to 650 nm, cf.

Fig. 4.15) the fluorescence of the donor group, removing any overlap with the absorption of A, which results in the absence of FRET in the molecular dynamics. This is illustrated in Fig.4.17 through the differential spectra of $\delta\_D_1\delta_+A$, at the same delays: in this case, the difference is only a slight change in the ESA, probably related to relaxation of the molecule. It can be noted that despite A not being excited in this last case (no stimulated emission from A nor anion absorption is observed), we still see a signal that is very close to the expected A's bleach.This is explained by the LUMO and thus the charge distribution being localized on the δ_+, resulting in an electrostatic interaction between the dipole moments of $(D\delta_+)^*$ and A, that shifts A's energetic levels and absorption (Stark effect). This is confirmed by the fact that this 450-600 nm part of the spectra is well fitted by a sum of the bleach of A and its absorption shifted by 3 nm to the blue (not shown).

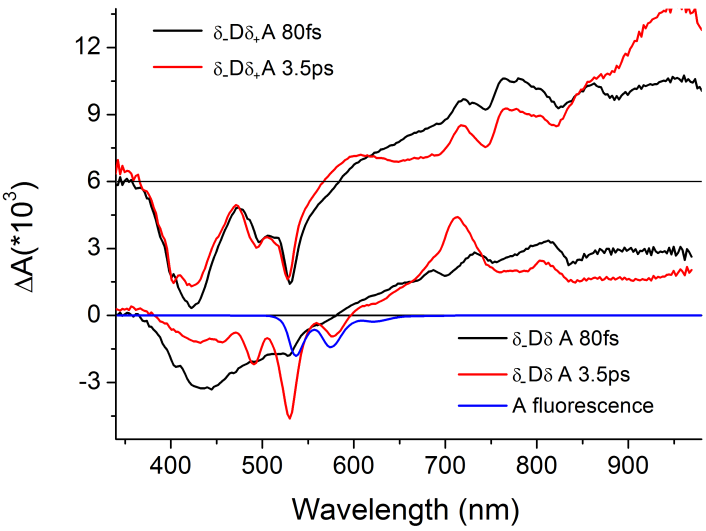

Figure 4.17: ΔA spectra for short times of diads $\delta\_D_1\delta A$ (bottom) and $\delta\_D_1\delta_+A$ (top, shifted for easier reading) in $CHCl_3$ after excitation at 400 nm, showing the impact of δ_+.The molecules without δ_+ display a clear energy transfer from the donor to the acceptor within a few ps, as shown by the reduction of the donor bleach at 425 nm and the appearance of bleach (490 and 529 nm), SE (536 and 573 nm) and ESA (708 nm) bands of A. On the other hand, no FRET can be seen for the molecules with δ_+, where no SE nor ESA from A appears. Only a bleach associated to A shifted can be observed.

The effects of the nature of the bridge on the reaction are high-

lighted on the selected kinetic traces in Fig. 4.18. For $\delta\_D_1\delta A$ (black lines), GSB of D (bottom, 432 nm trace) decreases in the first few ps, while GSB of A (532 nm, middle) increases, which corresponds to the energy transfer. In the following tens of picoseconds, the donor GSB increases again as the CT states are formed, which also results in the disappearance of the SE of A (thus the simultaneous decrease of the 532 nm trace), and the increase of the absorption at 719 nm, at the anion's maximum absorption. This clearly indicates that in this case, the reaction follows:

$$\delta\_D_1\delta A \xrightarrow{h\nu} (\delta\_D_1\delta)^* A \xrightarrow{FRET} \delta\_D_1\delta A^* \xrightarrow{CT} (\delta\_D_1\delta)^+ A^- \xrightarrow{rec.} \delta\_D_1\delta A$$

This reaction scheme is to be compared to that of $\delta\_D_1\delta_+ A$ (red traces in Fig4.18): in contrast to the $\delta\_D_1\delta A$ case, no FRET from the donor block to A occurs.

$$\delta\_D_1\delta_+ A \xrightarrow{h\nu} (\delta\_D_1\delta_+)^* A \xrightarrow{CT} (\delta\_D_1\delta_+)^+ A^- \xrightarrow{rec.} \delta\_D_1\delta_+ A$$

4.3.2.4 Impact of δ groups on CT formation and lifetime

The presence of the CT states is easy to identify in our molecules, as A^- has a very characteristic absorption spectrum with three peaks at 719 nm, 806 nm and 965 nm (see Fig. 4.16 and Fig.4.19 where we reconstruct the ΔA spectrum associated with the CT state of $\delta\_D_1\delta A$ with a sum of both D and A bleaches and D^+ and A^- absorptions, and Fig.4.19 dashed green ΔA spectrum associated to the CT state of $\delta\_D_1\delta_+ A$). Thus, following the dynamics of the absorption at 719 nm reveals the formation and recombination of the CT states.

As can be seen on both Fig.4.18 and 4.20 (traces at 719 nm, where rise times >1 ps correspond to CT formation), both formation and recombination of the CT states are impacted by the δ groups.

The addition of the δ_+ group leads to a slower formation time as clearly indicated by the rise time of the CT state in its presence (red, blue and pink curves) which is ≥100 ps, while without the δ+ group (black and green curves) this formation time is about 10 times faster. Note that with the δ bridge, hole transfer occurs after FRET, unlike the case for δ_+ bridge, where we have a LUMO→LUMO charge transfer.

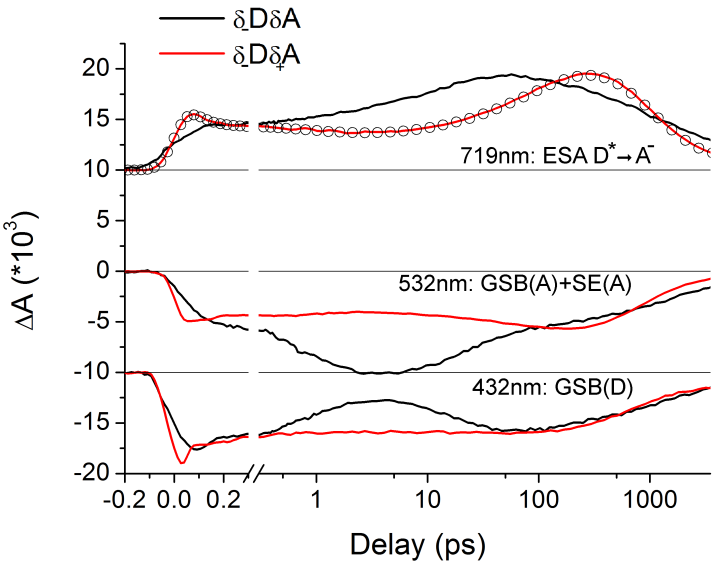

Figure 4.18: Kinetic traces at selected wavelength for diads $\delta_- D_1 \delta A$ (black lines) and $\delta_- D_1 \delta_+ A$ (red lines) in $CHCl_3$ after excitation at 400 nm. For the former, we can clearly see between a few hundreds of fs ans a few tens of ps that the donor's GSB (432 nm, curves shifted by -0.01) is reduced in favor of the acceptor's bleach and SE (532 nm unshifted curves). The difference between these 2 curves disappear when the CT states are formed, as only D and A GSB are visible in both curves at delays ≥100 ps. No such dynamic can be observed for $\delta_- D_1 \delta_+ A$'s kinetics. The 719 nm trace corresponds to the ESA of D* and A* at short times (<10 ps), and to the anion's absorption at longer delays. Hollow circles correspond to the fit of the trace with a sum of exponential decays.

Addition of the δ_- group allows for longer CT state lifetimes, as evidenced by the difference between black and green curve, or between blue and pink curves: the life time of the CT state changes from a few hundredth of ps to a few ns. Differential spectra at very long delays (several ns) reveal that some long lived species are formed, that we attribute to triplet states.

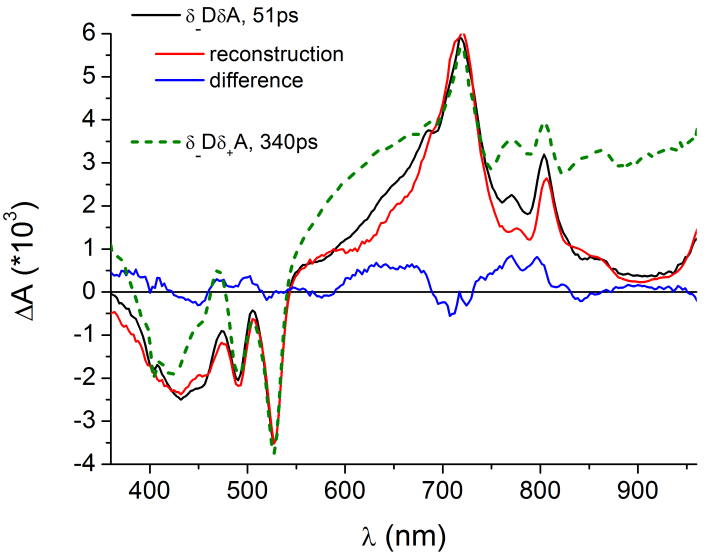

Figure 4.19: continuous lines: ΔA spectrum associated with the CT state of $\delta_- D_1 \delta A$, in $CHCl_3$. As the good correlation between the recorded (black) and the reconstructed (red) spectra shows, we can identify this CT state, as well as determine that almost all the molecules are in this CT state. A similar CT state can be observed for $\delta_- D_1 \delta_+ A$ (dashed green spectrum), overlapped with another ESA.

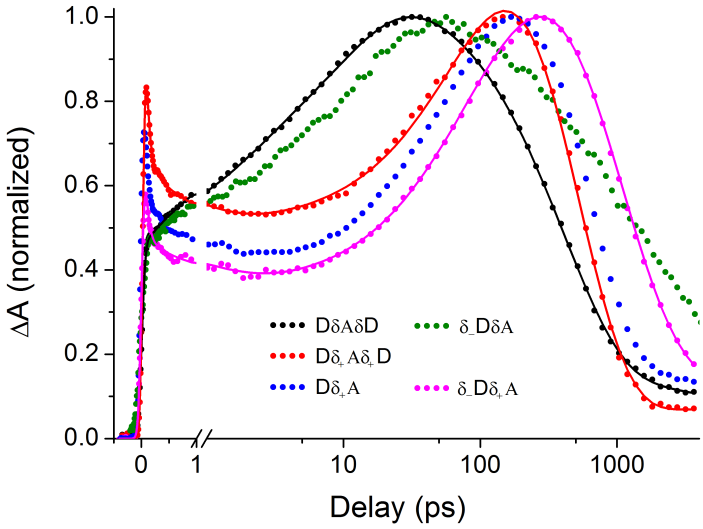

Figure 4.20: Kinetic traces at 719 nm of a selection of molecules, in $CHCl_3$ after excitation at 400 nm, revealing the effect of the various donors: CT states formation time increases with δ_+, their lifetime increases with δ_-. Lines correspond to fits.

4.3.2.5 Effect of the donor length

The Fig.4.21 shows kinetics at 719 nm, who as previously discussed indicate the formation and lifetime of CT states. It is clear that changing the donor length from $D_0\delta_+A$ to $D_3\delta_+A$ results in a very small change on the molecular dynamics. Indeed only D_0 has a slightly shorter CT state lifetime. Other differences are only in the first few ps, and are due to a different ESA shapes.

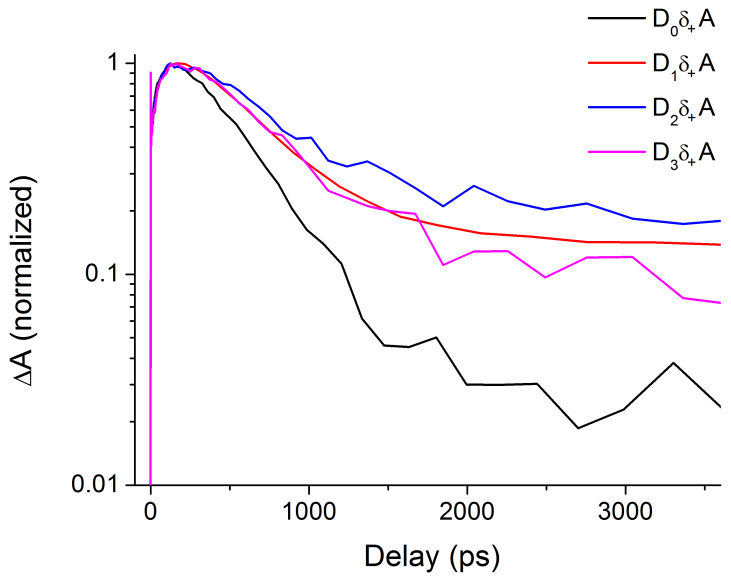

Figure 4.21: Kinetic traces at 719 nm for 4 similar dyads with increasing donor length, in $CHCl_3$ after excitation at 400 nm. The CT formation and recombination times are almost invariant as the donor length is increased from D_0 to D_3, and only the residual signal, associated to triplets, varies.

4.3.2.6 Global fitting and non-sequential models

Further analysis of the data revealed some more complexities in the dynamics of the different molecules: indeed "simple" fitting of the kinetics with sums of exponentials (assuming sequential models as shown earlier) proved to be insufficient in most cases. A thorough analysis of these datasets was done by LIU Li, using GloTarAn (cf. chapter 2.4.7), whose results are summarized in table 4.4. We devised models leading to the reactions schemes depicted below, which are the simplest models we could find in each case that resulted in sets of SADS and DADS that cohere with knowledge acquired from other experiments on separated components and spectra of excited or charged species. Most of the changes with respect to the models discussed before are simply parallel paths for the formation of the CT states.

For example, the molecule $D_1\delta A\delta D_1$ reaction scheme is represented in Eq.4.1 and follows the previously expected path (a FRET from the donor block to the acceptor in 860 fs, followed by the formation of the CT state in 7.1 ps, that lives for 380 ps before recombining either to the ground state or a triplet state):

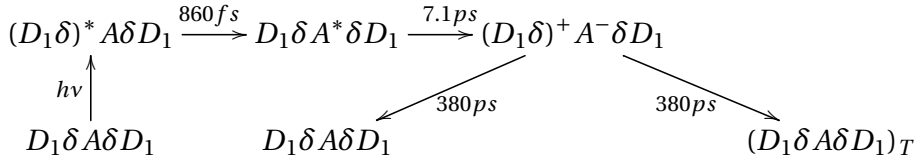

(4.1)

Note that compared with GHR molecules (cf. 4.2), the presence of the δ spacer increases the CT lifetime ~ 7 times.

But replacing δ by δ_+ does lead to a more complex reaction scheme, as shown in Eq.4.2 (tilted to fit in the page) for $D_1\delta_+A\delta_+D_1$. If we already knew that no energy transfer took place between donor and acceptor groups, we do discover that the formation of the CT state does not simply come from the excited donor state. Indeed, here a first relaxation occurs in 370 fs within the donor block from a higher energetic state (noted S_2, corresponding to the absorption of D) into a vibrationally excited state of δ_+ (noted S_1^+), before vibrationally relaxing within the S_1 state in 4.0 ps. This is evidenced by the SADS associated to these first steps, that include the donor bleach, and variations in both the ESA and SE, matching observations . Formation of the CT state occurs from the two latter states S_1^+ and S_1 with respective time constants of 14 ps (that competes with the 4.0 ps relaxation)

and 150 ps. The CT state then lives for 365 ps.

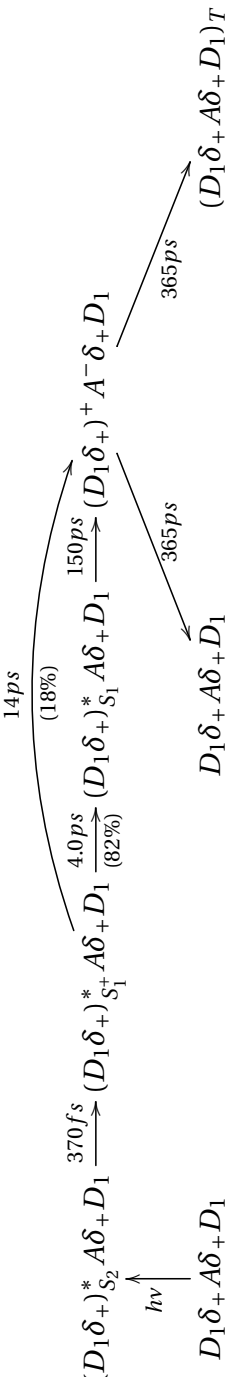

4.2

As observed before, the reaction scheme of $D_1\delta_+A\delta_+D_1$ and $D_1\delta_+A$ are very similar, with only slight changes in the time constants and ratios, as shown in Eq. 4.3. And in turn, as we saw previously that $D_1\delta_+A$, $D_2\delta_+A$ and $D_3\delta_+A$ showed very similar behavior, their reaction schemes are also found to be almost identical (Eq. 4.4 and 4.5)

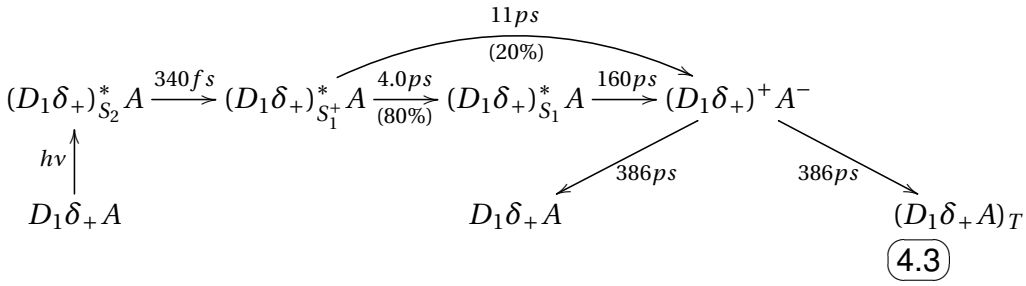

4.3

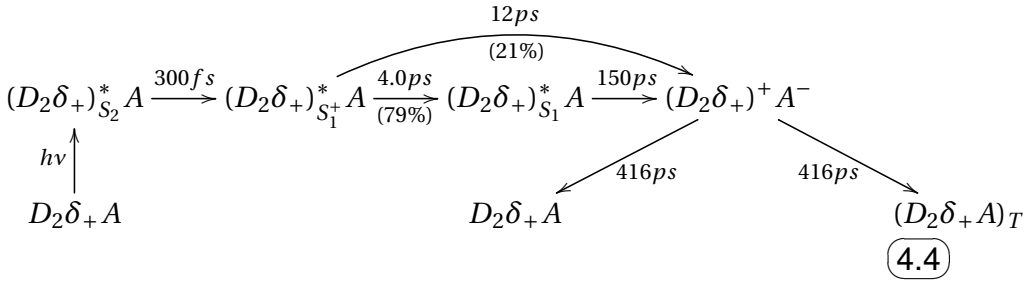

4.4

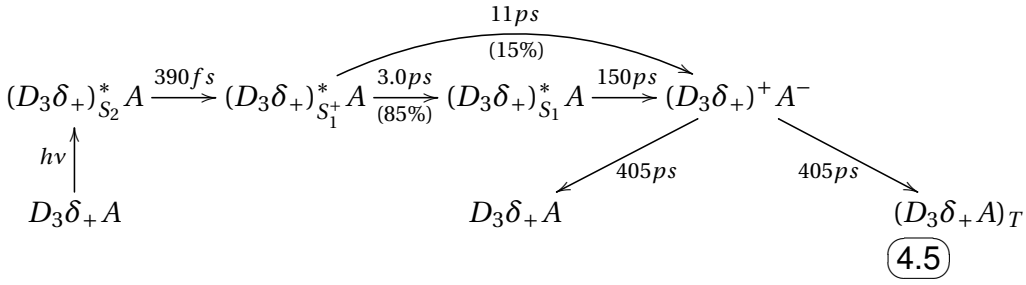

4.5

Surprisingly, even if the kinetics of $D_0\delta_+A$ showed very few differences with that of the longer dyads, a simpler reaction scheme is found, that only implies the relaxation of the hot S_1^+ state, and no parallel processes (Eq. 4.6)

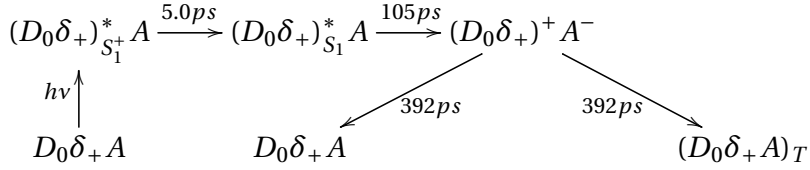

4.6

Finally, addition of the δ_- group does complicate these reaction scheme, as both the excited and charged states of the donor block now show two different states. Indeed, FRET occurs with two separate time constants, possibly due to different ground or excited state conformations. Likewise small spectral changes are interpreted as a ~200 ps relaxation of the CT leading to the long-lived $(\delta_-)^+D_1\delta_+A^-$. This results for $\delta_-D_1\delta A$ in the reaction 4.7:

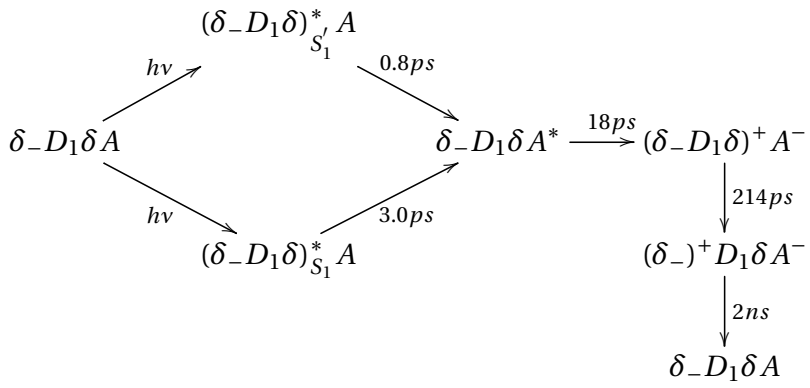

4.7

Molecule	Formation	Lifetime
$D_1\delta A\delta D_1$	7.1 ps	380 ps
$D_1\delta_+ A\delta_+ D_1$	14 ps (18%)/150 ps (82%)	365 ps
$D_0\delta_+ A$	105 ps	392 ps
$D_1\delta_+ A$	11 ps (20%)/160 ps (80%)	386 ps
$D_2\delta_+ A$	12 ps (21%)/150 ps (79%)	416 ps
$D_3\delta_+ A$	11 ps (15%)/150 ps (85%)	405 ps
$\delta_- D_1\delta_+ A$	14 ps (40%)/129 ps (60%)	1.2 ns
$\delta_- D_1\delta A$	18 ps	2.2 ns

Table 4.4: CT formation and lifetime in the different molecules studied, with the respective ratio of the two CT states formation path (when applicable) in each case.

4.3.3 Discussion

One can sum up all the previous observations in the table 4.4, that recapitulate the formation- and life-times in the different molecules.

To fully understand these results, we would like to use the Marcus theory framework. Indeed Marcus suggested that the rate k of a reaction can be written as in Eq. 4.8:

$$k_{et} = \frac{2\pi}{\hbar} V_R^2 \cdot FC \tag{4.8}$$

where V_R^2 relates to the electronic coupling and FC is the Franck-Condon-weighted density of states. The electronic coupling V_R^2 accounts for the exponential decay of the electronic wave-functions with respect to the distance R between donor and acceptor, with a coefficient β as described by Eq. 4.9:

$$V_R^2 = V_0^2 exp^{-\beta R} \tag{4.9}$$

The Franck-Condon term makes up for the overlap of the reactant and product nuclear wave-functions, and can be described through different models[73], accounting classical (FC_{cla}, Eq. 4.10) or quantum-mechanical effects (e.g. FC_{qua}, Eq. 4.11).

$$FC_{cla} = \frac{2}{\sqrt{4\pi\lambda k_b T}} e^{-\frac{(\lambda+\Delta G^\circ)^2}{4\lambda k_b T}} \tag{4.10}$$

Where λ is the reorganisation energy, and ΔG° is the energy difference between reactant and product states.

$$FC_{qua} = \frac{1}{\hbar\omega} \cdot e^{\frac{-\lambda}{\hbar\omega}(2n+1)} \cdot \left(\frac{n+1}{n}\right) \cdot \frac{-\Delta G^\circ}{2\hbar\omega} \cdot I_p\left(\frac{2\lambda}{\hbar\omega}\sqrt{n(n+1)}\right) \tag{4.11}$$

Where $\hbar\omega$ is the characteristic frequency of the harmonic oscillator, and $I_p()$ is a modified Bessel function of order p.

In our case, we don't have access to the characteristic frequency of our molecules, and thus will use the classical description.

Comparisons within this framework are only relevant for molecules in which the dynamics are similar: this equation relates to a transition from a given state A to another state B. By example, it is not relevant to compare the charge transfer generation in molecules with δ_+ (eg. $A\delta_+D_1$) and with δ (eg. $A\delta D_1$) from this "Marcus theory point of view", for in one case the CT state is formed from the donor excited state, while in the other it originates from the acceptor excited state.

ΔG° for the charge generation and recombination can be approximated from the oxydation/reduction potentials and absorption and fluorescence spectra of the respective moieties[74]. These potentials are directly related to the HOMO and LUMO levels reported in table 4.5. From this, we see that changes in the donor length (even from D_0 to $D_{n\geq 1}$) will have very little impact on ΔG° (a few tens of meV), as well as the addition of δ_-. Given λ values in the order of one eV, these changes should -a priori- not be responsible for sensible variations in the CT lifetime.

The same arguments hold for the effect of δ_-: appending δ_- decreases the HOMO of D block by no more than 80 meV, again negligible when compared with λ.

We rather think that the spatial shape of the HOMO of the donor block subsequently the electronic coupling V_R^2 are the central parameters influenced by the chemical composition of the donor block. Indeed as indicated by the preliminary results provided by G. Ori (cf. Fig. 4.14) and P. Eisenbrandt from I. Burghardt team (cf. Fig. 4.22),

Molecules ($\neq$ donor length)	$A\delta_+D_0$	$A\delta_+D_1$	$A\delta_+D_2$	$A\delta_+D_3$	A
LUMO (eV)	-3.13	-3.13	-3.15	-3.12	-3.90
HOMO (eV)	-5.19	-5.19	-5.20	-5.18	-6.20
Molecules ($\neq \delta$ groups)	$A\delta D_1$	$A\delta_+D_1$	$A\delta D_1\delta_-$	$A\delta_+D_1\delta_-$	A
LUMO (eV)	-2.61	-3.13	-2.53	-3.05	-3.90
HOMO (eV)	-5.17	-5.19	-5.11	-5.11	-6.20

Table 4.5: Values (in eV) of the energitical levels of the HOMO and LUMO, for the various studied molecules: changing the donor length does not impact these levels, but adding δ_+ does lower the LUMO level by about 0.5 eV, and δ_- does increase the HOMO level by 60 meV. Values for $D_1\delta A\delta D_1$ are identical to that of $A\delta D_1$. Results extracted from P.-O. Schwartz thesis [72].

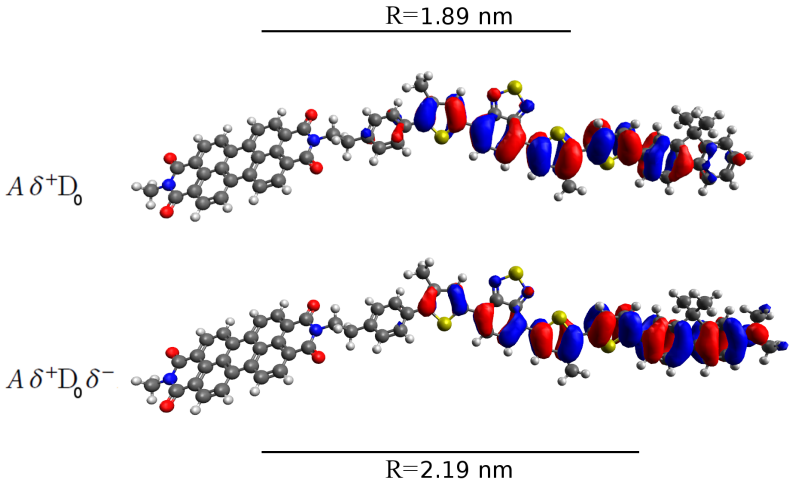

Figure 4.22: HOMO orbitals of the donor bloc for the molecules $A\delta_+D_0$ (top) and $A\delta_+D_0\delta_-$ (bottom), calculated by Pierre Eisenbrandt. Without the terminal amine δ_-, the HOMO is mostly located on the bridge δ_+ and first unit of D_n,while in presence of δ_- this HOMO is relocated at the end of the D block, towards the amine.

adding δ_- at the end of the donor moves the HOMO at its farthest end from the acceptor and its LUMO, thus reducing the overlap between their wavefunctions, and as a consequence the recombination rate of

the CT states. Considering all parameters constant except for the distance R (0.3 nm greater in presence of δ_-) and using Eq. 4.8 with the measured CT states life times, one get a value for β of $\sim$ 0.38 $Å^{-1}$, within usual values[75].

In a similar way, without δ_- the donor HOMO is localized on the first fluorene-bithiophene unit, and does not move away when additional units are present, which explain the similarities for $D_1\delta_+A$ to $D_3\delta_+A$. Additionally, this indicates that studying the impact of the length of the donor would make more sense on molecules with δ_-, as it should effectively reduce the orbitals overlap. Finally, it is also observed that the presence of δ_+ locates the donor LUMO on this bridge, implying a charge re-localization, leading to a blue-shift of the absorption of the acceptor.

Further theoretical study (mainly about the localization of HOMO and LUMO) are under progress by the team of Irene Burghardt, and may allow us to further understand our observations and confirm our interpretations.

Part III

General conclusions

5

Principal results

We used several complementary spectroscopy experiments (static or time-resolved) to study three sets of molecules, and determined their photo-induced dynamics.

The first molecule reported here is a BODIPY based antenna, that was developed in order to work in conjunction with an acceptor polymer. We observed that many parallel reaction paths exist, and that we even form charge transfer states in this antenna alone within 50 ps (with a CT lifetime of ~ 0.5 ns). This and the fact that we do observe an antenna effect, with the energy transfer toward the DPP and BOD moieties indicates that we may achieve the expected behavior (charge transfer toward the acceptor polymer) with a correctly chosen polymer.

The second reported study is centered around a Donor-Acceptor-Donor molecule with liquid-crystal properties. We first studied the molecule in solution, where we observed a very fast energy transfer (about 120 fs) from the donor to the acceptor, that was followed by an efficient CT state formation (below 3 ps), but with a very short lifetime

(about 55 ps). We then studied this same molecule in films, where its self-organization properties led to stacking of the molecules into a J-aggregate. The photo-dynamics were drastically changed, as the energy transfer is now overcome by the charge transfer, that occurs in less than 100 fs. This charge transfer state is generated before the localization of the excitation, leading to charge transfer states localized on one or more neighboring molecules, with different lifetimes, ranging from 1 ps to 1.3 ns. We also observe the formation of a triplet state. If the role of this triplet state for a possible charge generation is unclear, the very fast recombination of the charge transfer state (80 % recombine in under 100ps) is a major hindrance for the photovoltaic performances.

Based on the previous observations, new Donor-Acceptor-Donor molecules were developed, with many possible variations in the donor structure. The idea behind this was to find the ideal structure to increase the lifetime of the CT states while keeping the efficient charge generation. We studied several of these molecules in solution and showed that some characteristics of the donor structure do impact the photo-dynamic, while other do not. For example, we saw that adding the δ_+ group changes the dynamic from an energy transfer (in a few ps) followed by the charge transfer ($<$ 20 ps) to a direct formation of the charge transfer state, through two parallel paths (leading to an overall slower formation). On the other hand, changing the donor length did not resulted in meaningful changes. While the complete theoretical study is not yet achieved, these results seem to be understandable within the Marcus theory framework. First calculations of the frontier orbitals indicate that the electronic coupling between D and A is the main parameter that is modulated by the chemical design of D.

This thesis was made possible by the fruitful collaborations with Irene Burghardt (through the project MolNanoMat), Stéphane Méry (with the ANR PICASSO), Thomas Heiser and Raymond Ziessel (project Rhin-Solar), and Sabine Ludwigs.

6

Publications

This thesis work led to the publication of 2 articles on the first Donor-Acceptor-Donor molecule ("GHR", cf. 4.2):

Ultrafast broadband laser spectroscopy reveals energy and charge transfer in novel donor-acceptor triads for photovoltaic applications, *T. Roland, G. Hernandez-Ramirez, J. Léonard, S. Méry, S. Haacke*, **Journal of Physics: Conference Series**, 276, 1, 2011.

Sub-100 fs charge transfer in a novel donor–acceptor–donor triad organized in a smectic film, *T. Roland, J. Léonard, G. Hernandez-Ramirez, S. Méry, O. Yurchenko, S. Ludwigs, S. Haacke*, **Physical Chemistry Chemical Physics**, 14, 1, 2012.

Besides, two other articles are under work. One that report the results on the new Donor-Acceptor-Donor molecule ("POS", cf. 4.3.1):

Ultrafast Spectroscopy on New Donor-Acceptor Organic Molecules Reveals Importance of Chemical Composition on Donor in Charge Transfer, *T. Roland, L. Liu, J. Léonard, P.O. Schwartz, S. Méry, S. Ludwigs, O. Yurchenko, P. Eisenbrandt, I. Burghardt, S. Haacke*, in preparation.

And one on the molecular triad:

A detailed analysis of multiple photo-reactions in a light-harvesting molecular triad with over-lapping spectra by ultrafast spectroscopy, *T. Roland, L. Liu, E. Heyer, A. Ruff, S. Ludwigs, R. Ziessel, S. Haacke*, in preparation.

7

Perspectives

Starting from these results, we can better plan future experiments. Besides studying the BODIPY based antenna in an actual blend, the aim is mainly placed on the "new DAD" family of molecules, as they offer a lot of possibilities.

A first direction is to complete our analysis in solution, both with the help of theory (calculating the overlap between orbitals, and checking whether it fits the Marcus theory), and new experiments (as we now know that studying the donor length will make sense if we use molecules with a terminal δ_- group).

Going further, now that we have a better understanding of the dynamics in these "new DAD" isolated molecules, it would be interesting to proceed to the same kind of study we did on the "old DAD": doing the time resolved spectroscopy on films, where interactions between molecules will occur.

Even better, once a first study in films will be done, we hope to reproduce the experiments on full devices, so that we may study the

films under realistic conditions, and use electrical fields to better understand the charge generation and conduction. This is to be done in conjunction with the work of other teams (led by M. Brinkmann and T. Heiser, in the framework of the ANR project PICASSO), that aim at determining the structuration of the molecules in films and methods to insure that their structuration is indeed the wished one (cf. Fig.4.1) in actual photovoltaic devices, where the substrates and conductive layers change the self-organization properties of the molecules. For example, Fig.7.1 shows the organization obtained for the $D_0\delta_+A$ to $D_3\delta_+A$ dyads on glass substrates, revealing a very good organization of the molecules in a similar fashion as depicted on Fig. 4.2. Further details can be found in their article[76].

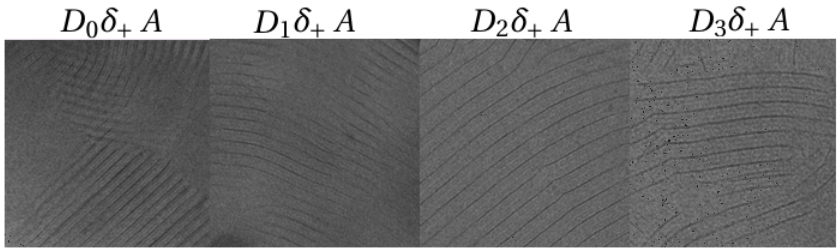

Figure 7.1: Organization of $D_0\delta_+A$ to $D_3\delta_+A$ films on glass substrates, obtained by TEM by Laure Biniek. Contrast corresponds to different electronic densities.

Hopefully, such a complete study will not only give us a good understanding of the many processes involved in the generation of photocurrent, but also allow us to develop new molecules on a more rational basis, and achieve high photovoltaic performances.

Part IV

Bibliography

8

Bibliography

[1] REN21, *Renewables 2013 Global Status Report*, 2013.

[2] H. Nifenecker, *Le nucleaire : un choix raisonnable?*, EDP Sciences, 2011.

[3] F. Dimroth, *ISE Fraunhofer*, 2013.

[4] B. O'Regan and M. Grätzel, *Nature*, 1991, **353**, 737–740.

[5] M. Grätzel, *Journal of Photochemistry and Photobiology C: Photochemistry Reviews*, 2003, **4**, 145 – 153.

[6] A. Yella, C.-L. Mai, S. M. Zakeeruddin, S.-N. Chang, C.-H. Hsieh, C.-Y. Yeh and M. Grätzel, *Angew. Chem.*, 2014, **126**, 3017–3021.

[7] T. W. Hamann, *Accounts of chemical research*, 2009, **42**, 1819–1826.

[8] T. W. Hamann, *Dalton Trans.*, 2012, **41**, 3111–3115.

[9] A. W. Hains, Z. Liang, M. A. Woodhouse and B. A. Gregg, *Chem. Rev.*, 2010, **110**, 6689–6735.

[10] S. Günes, H. Neugebauer and N. S. Sariciftci, *Chem. Rev.*, 2007, **107**, 1324–1338.

[11] G. Lanzani, *The Photophysics behind Photovoltaics and Photonics*, Wiley, 2012.

[12] J.-M. Nunzi, *C. R. Physique*, 2002, **3**, 523–542.

[13] K.-Y. Law, *Chem. Rev.*, 1993, **93**, 449–486.

[14] T. M. Clarke and J. R. Durrant, *Chem. Rev.*, 2010, **110**, 6736–6767.

[15] L. Zhao, J. L. P. Lustres, V. Farztdinov and N. P. Ernsting, *Phys. Chem. Chem. Phys.*, 2005, **7**, 1716–1725.

[16] X.-X. Zhang, C. Würth, L. Zhao, U. Resch-Genger, N. P. Ernsting and M. Sajadi, *Rev. Sci. Instrum.*, 2011, **82**, year.

[17] T. Gelot, P. Touron-Touceda, O. Cregut, J. Leonard and S. Haacke, *Journal of Physical Chemistry A*, 2012, **116**, 2819–2825.

[18] J.Briand, O. Bräm, J. Réhault, J. Léonard, A. Cannizzo, M. Chergui, V. Zanirato, M. Olivucci, J. Helbing and S. Haacke, *Physical Chemistry Chemical Physics*, 2010, **12**, year.

[19] G. Auböck, C. Consani, R. Monni, A. Cannizzo, F. V. Mourik and M. Chergui, *Review of Scientific Instruments*, Sep, **83**, 093105–093105–5.

[20] R. R. Alfano, *The Supercontinuum Laser Source*, Springer, 2006.

[21] P. A. Franken, A. E. Hill, C. W. Peters and G. Weinreich, *Phys. Rev. Lett.*, 1961, **7**, 118–119.

[22] G. Cerullo and S. D. Silvestri, *Review of Scientific Instruments*, 2003, **74**, year.

[23] P. Didier, *Ph.D. thesis*, Université de Strasbourg, 2004.

[24] A. Einstein, *Verh. der D. Physikal. Ges.*, 1916, **18**, 318–323.

[25] A. Einstein, *Mitteilungen der Physikalischen Gesellschaft Zürich*, 1916, **18**, year.

[26] S. J. Strickler and R. A. Berg, *Journal of Chemical Physics*, 1962, **37**, 814–822.

[27] C. Geskes and J. Heinze, *Journal of Electroanalytical Chemistry*, 1996, **418**, 167–173.

[28] J. You, L. Dou, K. Yoshimura, T. Kato, K. Ohya, T. Moriarty, K. Emery, C.-C. Chen, J. Gao, G. Li and Y. Yang, *Nature Communications*, 2012.

[29] Z. He, C. Zhong, S. Su, M. Xu, H. Wu and Y. Cao, *Nature Photonics*, 2012, **6**, 591–595.

[30] M. T. Dang, L. Hirsch and G. Wantz, *Adv. Mater.*, 2011, **23**, 3597–3602.

[31] L. G. kaake, G. C. Welch, D. Moses, G. C. Bazan and A. J. Heeger, *J. Phys. Chem. Lett.*, 2012, **3**, 1253–1257.

[32] J. M. Szarko, J. Guo, B. S. Rolczynski and L. X. Chen, *Nano Reviews*, 2011, **2**, year.

[33] D. Li, H. Yan, C. Li, Y. Yang, Z. Wei and C. Wang, *Chin. Sci. Bull.*, 2014, **59**, 360–368.

[34] T. Ameri, P. Khoram, J. Min and C. J. Brabec, *Adv. Mater.*, 2013, **25**, 4245–4266.

[35] J. Roncali, *Accounts of chemical research.*, 2009, 1719–1730.

[36] L. Biniek, C. L. Chocho, N. Leclerc, G. Hadziioannou, J. K. Kallitsis, R. Bechara, P. Leveque and T. Heiser, *Journal of Materials Chemistry*, 2009, **19**, 4946–4951.

[37] L. Biniek, C. L. Chochos, G. Hadziioannou, N. Leclerc, P. Leveque and T. Heiser, *Macromolecular Rapid Communications*, 2010, **31**, 651–656.

[38] J.-Y. Liu, M. E. El-Khouly, S. Fukuzumi and D. K. P. Ng, *ChemPhysChem*, 2012, **13**, 2030–2036.

[39] C. A. Wijesinghe, M. E. El-Khouly, J. D. Blakemore, M. E. Zandler, S. Fukuzumi and F. D'souza, *Chem. Commun.*, 2010, **46**, 3301–3303.

[40] S. Erten-Ela, M. D. Yilmaz, B. Icli, Y. Dede, S. Icli and E. U. Akkaya, *Org. Lett.*, 2008, **10**, 3299–3302.

[41] T. Kilicoglu and Y. S. Ocak, *Micro. Eng.*, 2011, **88**, 150–154.

[42] T. Rousseau, A. Cravino, T. Bura, G. Ulrich, R. Ziessel and J. Roncali, *Chem. Commun.*, 2009, 1673–1675.

[43] S. Suzuki, M. Kozaki, K. Nozaki and K. Okada, *Journal of Photochemistry and Photobiology C: Photochemistry Reviews*, 2011, 269–292.

[44] S. Hattori, K. Ohkubo, Y. Urano, H. Sunahara, T. Nagano, Y. Wada, N. V. Tkachenko, H. Lemmetyinen and S. Fukuzumi, *J. Phys. Chem. B*, 2005, **109**, 15368–15375.

[45] V. S. Gevaerts, E. M. Herzig, M. Kirkus, K. H. Hendriks, M. M. Wienk, J. Perlich, P. Müller-Buschbaum and R. A. J. Janssen, *Chem. Mater.*, 2013.

[46] S. Izawa, K. Hashimoto and K. Tajima, *Chem. Comm.*, 2011, **47**, 6365–6367.

[47] N. Banerji, M. Wang, J. Fan, E. S. Chesnut, F. Wudl and J.-E. Moser, *J. Mater. Chem.*, 2012, 1286–13294.

[48] S. D. Dimitrov, C. B. Nielsen, S. Shoaee, P. S. Tuladhar, J. Du, I. McCulloch and J. R. Durrant, *J. Phys. Chem. Lett*, 2012, 140–144.

[49] S. Qu and H. Tian, *Chem. Commun.*, 2012, **48**, 3039–3051.

[50] B. P. Karsten, R. K. M. Bouwer, J. C. Hummelen, R. M. Williams and R. A. J. Jansen, *Photochem. Photobiol. Sci.*, 2010, **9**, 1055–1065.

[51] S. D. Dimitrov, Z. Huang, F. Deledalle, C. B. Nielsen, B. C. Schroeder, R. S. Ashraf, S. Shoaee, I. McCulloch and J. R. Durrant, *Energy Environ. Sci.*, 2014, 1037–1043.

[52] M. M.Wienk, M. Turbiez, J. Gilot and R. A. J. Janssen, *Adv. Mater.*, 2008, 2556–2560.

[53] D. P. Hagberg, T. Edvinsson, T. Marinado, G. Boschloo, A. Hagfeldtb and L. Sun, *Chem. Comm.*, 2006, 2245–2247.

[54] H. Tian, X. Yang, J. Pan, R. Chen, M. Liu, Q. Zhang, A. Hagfeldt and L. Sun, *Adv. Funct. Mater.*, 2008, **18**, 3461–3468.

[55] F. Zhang, Y.-H. Luo, J.-S. Song, X.-Z. Guo, W.-L. Liu, C.-P. Maa, Y. Huang, M.-F. Ge, Z. Bo and Q.-B. Meng, *Dyes and Pigments*, 2009, **81**, 224–230.

[56] W. Xu, B. Peng, J. Chen, M. Liang and F. Cai, *J. Phys. Chem*, 2008, **112**, 874–880.

[57] L. Schmidt-Mende, A. Fechtenkötter, K. Müllen, E. Moons, R. Friend and J. MacKenzie, *Science*, 2010, **293**, 1119–1122.

[58] L. Bu, X. Guo, B. Yu, Y. Qu, Z. Xie, D. Yan, Y. Geng and F. Wang, *J.A.C.S.*, 2009, **131**, 13242–13243.

[59] G. Ramirez, *Ph.D. thesis*, Université de Strasbourg, 2010.

[60] L. Bu, X. Guo, B. Yu, Y. Qu, Z. Xie, D. Yan, Y.-H. Geng and F. Wang, *J. Am. Chem. Soc.*, 2009, **132**, 13242–13243.

[61] B.-R. Gao, J.-F. Qu, Y. Wang, Y.-Y. Fu, L. Wang, Q.-D. Chen, H.-B. Sun, Y.-H. Geng, H.-Y. Wang and Z.-Y. Xie, *J. Phys. Chem. C*, 2013, **117**, 4836–4843.

[62] J. Qu, B. Gao, H. Tian, X. Zhang, Y. Wang, Z. Xie, H. Wang, Y.-H. Geng and F. Wang, *J. Mater. Chem. A*, 2014, **2**, 3632–3640.

[63] E. Peeters, P. A. van Hal, S. C. J. Meskers, R. A. J. Janssen and E. W. Meijer, *Chem. Eur. J.*, 2002, **8**, 4470–4474.

[64] T. Roland, G. H. Ramirez, J. Léonard, S. Méry and S. Haacke, *Journal of Physics: Conference Series*, 2011, **276**, year.

[65] T. Roland, J. Leonard, G. Ramirez, S. Mery, O. Yurchenko, S. Ludwigs and S. Haacke, *Phys. Chem. Chem. Phys.*, 2012, **14**, 273–279.

[66] W. Paa, J.-P. Yang, M. Helbig, J. Hein and S. Rentsch, *Chemical Physics Letters*, 1998, **292**, 607–614.

[67] W. Paa, J.-P. Yang and S. Rentsch, *Synthetic Metals*, 2001, **119**, 525–526.

[68] F. Würthner, T. E. Kaiser and C. R. Saha-Möller, *Angew. Chem. Int. Ed.*, 2011, **50**, 3376–3410.

[69] W. E. Ford and P. V. Kamat, *J. Phys. Chem*, 1987, **91**, 6373–6380.

[70] T. Kircher and H.-G. Löhmannsröben, *Phys. Chem. Chem. Phys.*, 1999, **1**, 3987–3992.

[71] D. Veldman, O. Ipek, S. C. J. Meskers, J. Sweelssen, M. M. Koetse, S. C. Veenstra, J. M. Kroon, S. S. van Bavel, J. Loos and R. A. J. Janssen, *J.A.C.S.*, 2008, **130**, 7721–7735.

[72] P.-O. Schwartz, *Ph.D. thesis*, Université de Strasbourg, 2013.

[73] C. C. Moser, J. M. Keske, K. Warncke, R. S. Farid and P. L. Dutton, *Nature*, 1992, **355**, 796–802.

[74] N. J. Turro, V. Ramamurthy and J. Scaiano, *Principles of Molecular Photochemistry*, University Science paper, 2009.

[75] H. Wang, E. R. McNellis, S. Kinge, M. Bonn and E. Cánovas, *Nano Lett.*, 2013, **13**, 5311–531.

[76] P. Schwartz, L. Biniek, E. Zaborova, B. Heinrich, M. Brinkmann, N. Leclerc and S. Méry, *J. Am. Chem. Soc.*, 2014, **136**, 5981–5992.

Part V

List of figures

List of Figures

Part VI

List of tables

List of Tables

Part VII

Index

Index

Thomas ROLAND

Ultrafast Spectroscopy of New Organic Molecules for Photovoltaic Application

Résumé

Cette thèse porte sur l'étude de nouvelles molécules organiques par différentes méthodes de spectroscopie. La combinaison de techniques de fluorescence résolue en temps, d'absorption différentielle résolue en temps et de spectro-électro-chimie avec des méthodes d'analyse globale permet de déterminer la photo-dynamique des molécules étudiées. Deux familles de molécules ont été étudiées . La première est une antenne de type donneur basée sur le pigment BODIPY. La seconde consiste en une triade donneur-accepteur-donneur (DAD) ayant des propriétés d'auto-organisation. Après une première génération de molécules dont on a montré les limitations (temps de vie de l'état transfert de charge très court, d'environ 55 ps), une seconde génération de molécules a été développée, incluant de nombreuses variations du groupe donneur, ce qui a permis de déterminer l'impact des-dites variations. Entre autres, un temps de vie de l'état transfert de charge de plus d'une nanoseconde est observé.

Mots clés: Spectroscopie, ultra-rapide, transfert de charge, FRET, BODIPY, donneur-accepteur, théorie de Marcus

Abstract

The topic of this thesis is the study -through different spectroscopy methods- of new organic molecules for photovoltaic applications. Combination of time resolved fluorescence, time resolved differential absorption and spectro-electro-chemistry with global analysis methods allowed to determine the photo-dynamics of the studied molecules. Two families of molecules have been studied. The first one is a donor-type antenna based on the BODIPY dye. The second consists in a donor-acceptor-donor (DAD) triad, with self-organizing properties. After a first generation of molecules that we proved to be limited by a short life time of its charge transfer state (about 55 ps), a second generation of molecules was developed, including several variation of the donor group, which allowed to study the impact of said variation. Among others, a charge transfer state lifetime longer than 1 nanosecond was observed.

Keywords:Spectroscopy, ultra-fast, charge transfer, FRET, BODIPY donor-acceptor, Marcus theory